AD NUMBER
AD225362
LIMITATION CHANGES

TO:
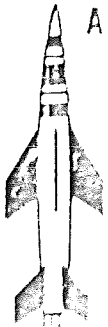
Approved for public release; distribution is unlimited.

FROM:

Distribution authorized to DoD and DoD contractors only; Administrative/Operational Use; SEP 1959. Other requests shall be referred to Arnold Engineering Development Center, Arnold AFB, TN.

AUTHORITY

AEDC ltr 13 Nov 1975

DETERMINATION OF OPTIMUM OPERATING
PARAMETERS FOR THE PWT 16-FT TRANSONIC
CIRCUIT UTILIZING ONE-PERCENT
BODIES OF REVOLUTION

By

James H. Nichols

PWT, ARO, Inc.

September 1959

ARNOLD ENGINEERING

DEVELOPMENT CENTER

AIR RESEARCH AND DEVELOPMENT COMMAND

U S   A F

DETERMINATION OF OPTIMUM OPERATING PARAMETERS
FOR THE PWT 16-FT TRANSONIC CIRCUIT
UTILIZING ONE-PERCENT BODIES OF REVOLUTION

By

James H. Nichols

PWT, ARO, Inc.

September 1959

ARO Project No. 220005

Contract No. AF 40(600)-800

CONTENTS

ILLUSTRATIONS

ABSTRACT

This report presents data obtained during an investigation of test section interference in the PWT 16-Ft Transonic Circuit using cone-cylinder and ogive-cylinder configurations having 1-percent blockage. Pressure distributions and base pressure data on a 20 deg cone-cylinder 10.0-diam long are presented and used to determine optimum test section wall angle and test leg pressure ratio settings for Mach numbers between 0.6 and 1.6. Comparisons are made with interference-free cone-cylinder data which show that tunnel wall interference between M = 0.95 and M = 1.10 cannot be completely eliminated with the present test section configuration. Ogive-cylinder pressure distributions are presented. Three-component force data are presented for 8.5-diam cone-cylinder and ogive-cylinder configurations, and comparisons are made with interference-free cone-cylinder data.

NOMENCLATURE

C_D	Drag coefficient, $Drag/q_\infty S$
$C_{D,b}$	Base-drag coefficient, $(p_\infty - p_b)/q_\infty$
$C_{D,F}$	Forebody-drag coefficient, $C_D - C_{D,b}$
C_L	Lift coefficient, $Lift/q_\infty S$
C_m	Pitching-moment coefficient referenced to the model nose, $Moment/q_\infty SD$
C_N	Normal-force coefficient, $Normal\ force/q_\infty S$
D	Diameter of model base, 1.800 ft
M_∞	Free-stream Mach number
p	Local static pressure, psfa
p_b	Pressure at model base, psfa
p_t	Tunnel total pressure, psfa
p_∞	Free-stream static pressure, psfa
q_∞	Free-stream dynamic pressure, $0.7\,p_\infty M_\infty^2$, psf
r	Radius used to define ogive nose profile, ft
S	Area of model base, $(\pi/4)D^2 = 2.544\ ft^2$

x	Distance from model nose, ft
α	Model angle of attack, deg
λ	Test leg pressure ratio (ratio of tunnel total pressure to the static pressure at the end of the diffuser)
λ^*	Optimum test leg pressure ratio
θ_w	Test section wall angle, deg, (positive when walls are diverged)
θ_w^*	Optimum test section wall angle, deg
$dC_L/d\alpha$	Rate of change of lift coefficient with angle of attack at $C_L = 0$
$dC_N/d\alpha$	Rate of change of normal-force coefficient with angle of attack at $C_N = 0$
dC_m/dC_L	Rate of change of pitching-moment coefficient with lift coefficient at $C_m = 0$
dC_m/dC_N	Rate of change of pitching-moment coefficient with normal-force coefficient at $C_m = 0$

INTRODUCTION

When testing in transonic wind tunnels, it is important to know the nature and extent of interference which will be encountered when compression and expansion waves generated by the model are reflected back to the model after striking the test section walls. In all transonic tunnels this interference increases with increasing model size and length. In the PWT 16-Ft Transonic Circuit, however, because of the type of test section walls and the ability to vary test section wall angle and test leg pressure ratio, interference can be reduced for the larger models by proper adjustment of the test section parameters. The purpose of this investigation was to determine the optimum settings for the test section parameters with 1-percent-blockage bodies of revolution 8.5- and 10.0-diam in length. Comparisons are made with data obtained in earlier investigations using 0.01-percent-blockage models which produce data essentially free of interference. This investigation was conducted during December 1957.

APPARATUS

TUNNEL

- The PWT 16-Ft Transonic Circuit is a closed-circuit, continuous-flow wind tunnel capable of operating at Mach numbers between 0.5 and 1.6 and at tunnel total pressures between 50 and 4000 psfa. The main compressor of the tunnel has been augmented by means of a plenum auxiliary suction system which removes air from the plenum chamber surrounding the test section and injects this air into the diffuser downstream of the test section. The pressure ratio across the test section leg of the tunnel can be varied at any Mach number by adjusting the balance between the main compressor blade setting and the plenum auxiliary flow rate. During this investigation only three of the five compressors of the auxiliary suction system were available for use.

Supersonic Mach numbers are obtained by the use of a flexible-wall Laval-type nozzle. Contours are provided for Mach numbers from 1.00 to 1.63 at intervals of approximately 0.025 in Mach number.

A more complete description of the tunnel and its facilities may be found in Ref. 1.

TEST SECTION

The test section is 16 by 16 ft in cross section (see Fig. 1). There is an initial 10 ft length which is a permanent part

Manuscript released by author July 1959.

of the tunnel and provides a linear transition from the solid walls of the nozzle to the perforated walls of the testing region which is contained in the 40 ft long test section cart. A sting support system is provided in the solid-walled rear portion of the test section, and the two moveable test section side walls are bulged outward in this area to prevent choking and to minimize subsonic interference from the support strut. Details of the test section geometry and the perforated wall liners are shown in Fig. 1.

MODELS

The models used in this investigation were made up of components which could be assembled in several combinations to give the desired model geometry. The basic components were a cylindrical body, a body extension, a conical nose having a 20 deg total angle, and an ogive nose which had the same shape as the nose of the AGARD model B. The three configurations used were the 10.0-diam cone-cylinder, made up of the conical nose, the cylindrical body, and the body extension; the 8.5-diam cone-cylinder, made up of the conical nose and cylindrical body; and the 8.5-diam ogive-cylinder, made up of the ogive nose and the cylindrical body. The location of the models in the test section is shown in Fig. 1, and a photograph of a typical installation is shown in Fig. 2. Details of the models are shown in Fig. 3. Each model had base pressure orifices and a single longitudinal row of pressure orifices to obtain pressure distributions. All models were mounted on a 6-component internal strain-gage balance. Model blockage was in all cases 1-percent (ratio of model cross-sectional area to test section cross-sectional area).

INSTRUMENTATION

The internal strain-gage balance used during this investigation was 8 in. in diameter and incorporated beams for determining all six force and moment components, although only three were used for this investigation. In order to obtain the greatest sensitivity, the balance was rolled so that the 5000 lb side force elements could be used to measure normal force, rather than the standard 8000 lb normal force elements. The axial force element used was rated at 3000 lb. The overall accuracy obtainable with this balance is approximately ± 0.35 percent of the full design load of the elements.

Pressure leads from all model orifices were routed down the support system to an area beneath the test section where they were connected to pressure transducers of the standard pressure measuring system of the tunnel. Signals from these transducers were fed into the on-line data reduction system.

Measurements from both the strain-gage balance and the pressure transducers were fed directly into the input system of the automatic

digital computer. On-line data reduction procedures were used so that final force, moment, and pressure coefficients were obtained immediately in both tabular and plotted form and were used in guiding the progress of the test.

TEST DESCRIPTION

TEST PROCEDURE

The procedure followed during this investigation can be broken down into several phases. The configuration used for the initial phase was the 10.0-diam cone-cylinder. With this configuration, pressure distributions and base pressures were obtained at zero angle of attack at each Mach number as test section wall angle, θ_w, and test leg pressure ratio, λ, were varied independently.

For the second phase of the investigation, the rear cylindrical extension was removed to form the 8.5-diam cone-cylinder, and the base of the model was moved forward 2.7 ft. Using the test section wall angle which resulted in the best body pressure distribution during the initial phase, designated θ_w^*, base pressure was measured at each Mach number as test leg pressure ratio was varied. At each Mach number, the base pressure data obtained with both the 10.0- and the 8.5-diam cone-cylinders were compared, and the test leg pressure ratio which resulted in the same base pressure for the two bodies was selected as the optimum value, designated λ^*. The reason for this basis for the selection of the optimum test leg pressure ratio can be better understood if the empty test section case is considered first. Variations in test leg pressure ratio affect the test section flow in such a manner as to produce a varying amount of gradient in the pressure distributions at the downstream end of the test section. The optimum pressure ratio usually selected is that which minimizes this pressure gradient. When a model is installed, the test section losses are increased, and the optimum λ for the tunnel empty case is no longer the optimum. Since the model base pressure is the most sensitive indication of the effects of gradients at the rear of the test section, the optimum λ is defined as that which will produce the same base pressure over a range of axial locations of the model base. A more detailed explanation of this procedure may be found in Ref. 2.

The third phase consisted of determining force and moment data with the 8.5-diam cone-cylinder, using θ_w^* and λ^*.

For the fourth phase, the ogive nose was installed, and pressure data were obtained with the 8.5-diam ogive-cylinder, again using θ_w^* and λ^*.

The fifth and final phase consisted of determining force and moment data with the 8.5-diam ogive-cylinder at θ_w^* and λ^*.

TEST CONDITIONS

During this test results were obtained at Mach numbers from 0.6 to 1.6. The angle of the test section side walls was varied from -0.75 deg to +1.00 deg, and the test leg pressure ratio was varied from 1.036 to 1.479. Tunnel total pressure was varied from 1000 to 1500 psfa, and the resulting Reynolds numbers are presented in Fig. 4. Also shown in this figure are the Reynolds numbers at which data were obtained with the 0.01-percent blockage model, which are presented for correlation purposes in this report.

PRECISION OF MEASUREMENTS

An estimate of the precision of the measurements presented in this report is given in the table below. Because the loads during this test represented only a small percentage of the balance capacity, the precision achieved in force and moment measurements is poor when compared with normal standards.

ΔM	$\Delta \lambda$	$\Delta p/pt$	$\Delta \theta_w$	Δa	ΔC_L	ΔC_m	$\Delta C_{D,F}$	$\Delta C_{D,b}$
±.003	±.005	±.004	±.02	±.05	±.020	±.060	±.010	±.003

The Mach number error presented above does not include the deviation from the mean value in the region of the model. This deviation was ±0.003 at subsonic Mach numbers and up to ±0.010 at supersonic Mach numbers.

RESULTS AND DISCUSSION

Figures 5 through 16 illustrate the effects of test section wall angle variations and test leg pressure ratio variations on pressure distributions obtained with the 10.0-diam cone-cylinder at each Mach number. At Mach numbers of 0.80, 1.00, and 1.50, data are presented showing the effects of test leg pressure ratio variations at four test section wall angles and the effects of wall angle variations at a fixed pressure ratio. At each of the other Mach numbers, pressure ratio effects are presented for only one wall angle. At Mach numbers of 0.60 through 0.95, wall angle variations had only small effects on the body pressure distributions; however, when wall angle was held constant, pressure ratio variation caused changes in the distributions near the rear of the model.

At Mach number 1.00, both wall angle variations and pressure ratio variations had small effects on the pressure distributions over the body; complete data are presented for this Mach number to illustrate that none of these effects were large.

At Mach numbers of 1.05 through 1.60, variations in test leg pressure ratio had no effect on the cone-cylinder pressure distributions. Test section wall angle variations, however, showed very noticeable effects on these distributions, particularly through Mach number 1.50. At M = 1.60 the disturbance field has moved downstream of the base of the model and does not affect a model of this length.

In general, the results of this phase of the investigation indicate that at subsonic Mach numbers, pressure ratio variations had a predominant effect on body pressure distributions, while wall angle variations had a negligible effect; conversely, at supersonic Mach numbers, wall angle variations showed predominant effects, while pressure ratio effects were negligible.

Figure 17 presents the optimum test section wall angle as a function of Mach number. In order to simplify and speed up operation in the Mach number range from 0.6 to 0.95 the θ_w = 0 deg setting was selected for use at these Mach numbers. The points presented for the supersonic Mach numbers were selected after a careful study of all results after completion of the test and differed slightly from the settings selected during the course of the test. In several cases the points selected represent interpolated or extrapolated settings at which data were not obtained during the test. These optimum values of θ_w have been designated θ_w^*.

Figure 18 presents a comparison of base pressure data obtained with the 10.0- and the 8.5-diam cone-cylinders. When an intersection of the curves could be obtained, the value of test leg pressure ratio resulting in this intersection was selected as the optimum value, designated λ^*. When an intersection could not be obtained, the value of λ^* was selected after a careful examination of the curves for each Mach number. (Because of the wide range of conditions presented, it was necessary to change the scale of the plots for Mach numbers above 1.05.)

Figure 19 presents values of λ^*, the optimum test leg pressure ratio, for the models tested. As indicated in Fig. 18, the values of θ_w used to determine these values of λ^* were not in all cases the θ_w^* presented in Fig. 17.

The high values of λ^* at Mach numbers 1.05 and 1.10 in Fig. 19 are a result of the converged wall requirements for obtaining the minimum of reflected disturbances, which represent a power requirement considerably above that for operation with parallel walls. In cases where power is a prime consideration, it may be desirable to forego the θ_w^* settings at these Mach numbers to test at higher stagnation pressures.

Figure 20 presents a comparison of the pressure distributions obtained with the 10.0-diam cone-cylinder with data from Ref. 3 for a 0.01-percent blockage model, which was essentially interference-free. In choosing 10.0-diam cone-cylinder data for this comparison, distributions were selected which were obtained with conditions which most closely represented the values of θ_w^* and λ^*. Distributions for Mach numbers 0.80 and 0.90 compare very closely with the interference-free data. The effects of wall-induced disturbances begin to appear at Mach number 0.95, and are readily seen at Mach numbers of 1.00, 1.05, and 1.10. At Mach number 1.20 and above, slight disagreements are evident in the distributions, but none appear to be of a serious nature. (Because Ref. 3 presents no M = 1.5 data, comparison was made with a theoretical curve for this Mach number.) Hence, the range in which interference will be a problem with models of this general geometry begins at a Mach number of 0.95 and extends through a Mach number of 1.10.

Figure 21 presents pressure distributions measured with the 8.5-diam ogive-cylinder. No interference-free data were available for comparison. Interference disturbances can be observed at the same Mach numbers as with the 10.0-diam cone-cylinder.

The basic force and moment data for the 8.5-diam cone-cylinder and ogive-cylinder models are presented in Figs. 22 through 27. The lift and moment curve slopes as functions of Mach number are shown in Figs. 28 and 29 for these two configurations.

The variations of forebody- and base-drag coefficients with Mach number for the 1-percent cone-cylinder and ogive-cylinder models are presented in Fig. 30. As was expected, the forebody-drag coefficients for the two bodies show excellent agreement at a Mach number of 0.60 and above a Mach number of 1.20, while demonstrating entirely different transonic characteristics. Base drag coefficients for the two bodies differ slightly below a Mach number of 0.90 but agree quite well at all higher Mach numbers.

Figure 31 presents a comparison of the normal-force curve slope obtained with the 8.5-diam cone-cylinder model and that obtained with a model having 0.01-percent blockage, which is essentially interference-free because of its size. This comparison must be made on the basis of normal force rather than lift because these unpublished data from an earlier test were obtained with a balance which had no axial force element. Because both tests were conducted with balances of relatively poor sensitivity, the agreement is considered quite good.

Figure 32 presents a comparison of the slopes of the pitching-moment curves for the 1-percent and 0.01-percent models. Again, when the balance sensitivities are considered, the agreement is good.

CONCLUSIONS

This investigation of optimum operating parameters for the 16-Ft Transonic Circuit utilizing 1-percent bodies of revolution has resulted in the following conclusions:

1. At subsonic Mach numbers, variations in test leg pressure ratio have definite effects on model pressure distributions, while test section wall angle variations show little or no effect.

2. At supersonic Mach numbers, variations in test section wall angle have definite effects on model pressure distributions, while test leg pressure ratio variations show little or no effect.

3. Values of θ_w^* and λ^* presented in this report represent optimum conditions for minimizing test section interference with models of the type and size used in this investigation.

4. The operating range in which test section interference on models of the type and size used in this investigation cannot be eliminated begins at a Mach number of 0.95 and ends at Mach number 1.10.

5. Interference which is noticeable in pressure data between Mach numbers of 0.95 and 1.10 is not apparent in the normal-force and pitching-moment data.

REFERENCES

1. Test Facilities Handbook, (2nd Edition). "Propulsion Wind Tunnel Facility, Vol. 3." Arnold Engineering Development Center, January 1959.

2. Rittenhouse, L. E. "Base Pressure Effects Resulting from Changes in Tunnel Pressure Ratio in a Transonic Wind Tunnel." AEDC-TN-58-88, January 1959.

3. Estabrooks, Bruce B. "Wall-Interference Effects on Axisymmetric Bodies in Transonic Wind Tunnels." AEDC-TR-59-12, June 1959.

TYPICAL PERFORATED
WALL PATTERN

Section A-A

6% Open Area
Hole Diameter = 0.75 In.
Plate Thickness = 0.75 In.
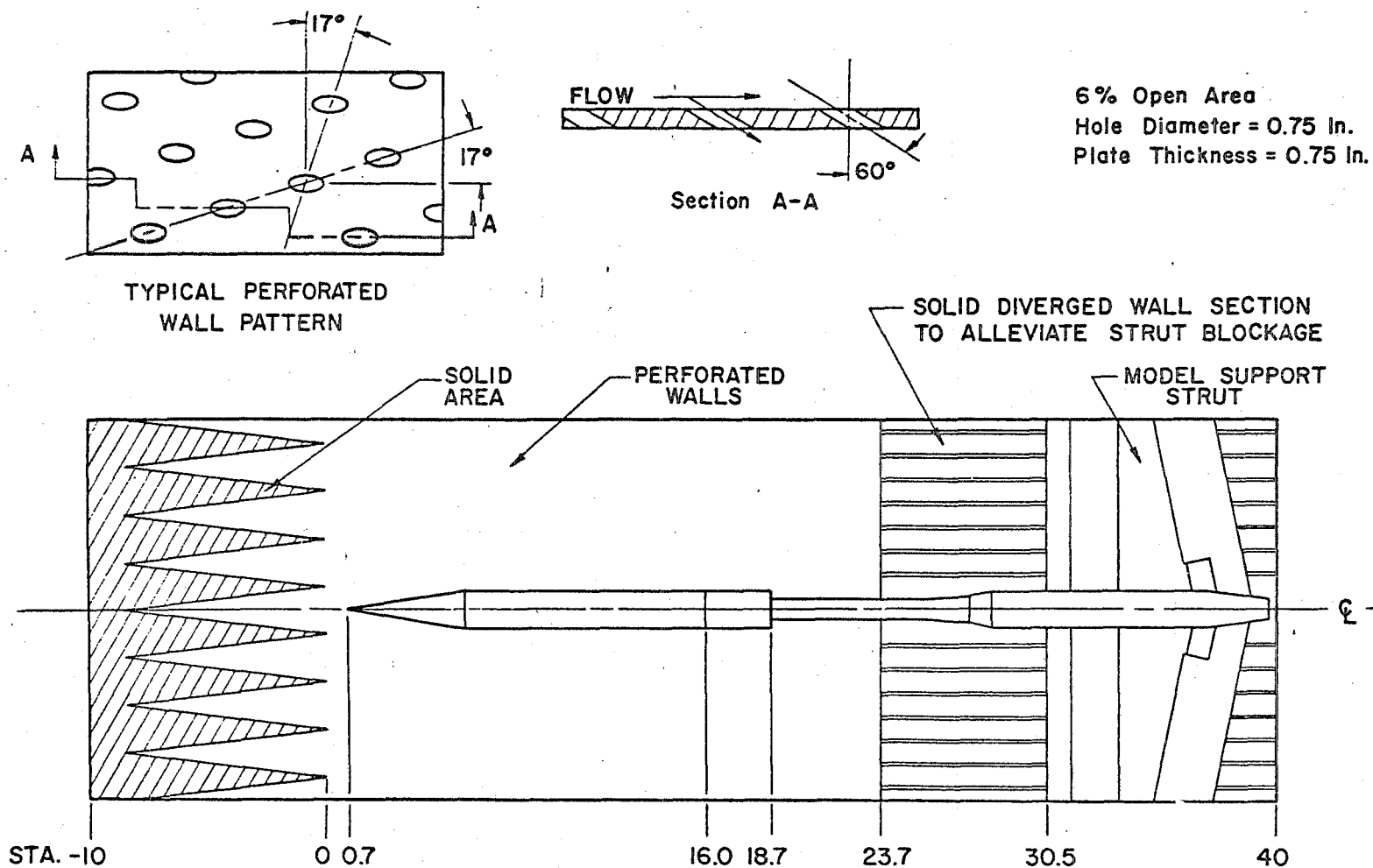
Fig. 1 Details of Test Section
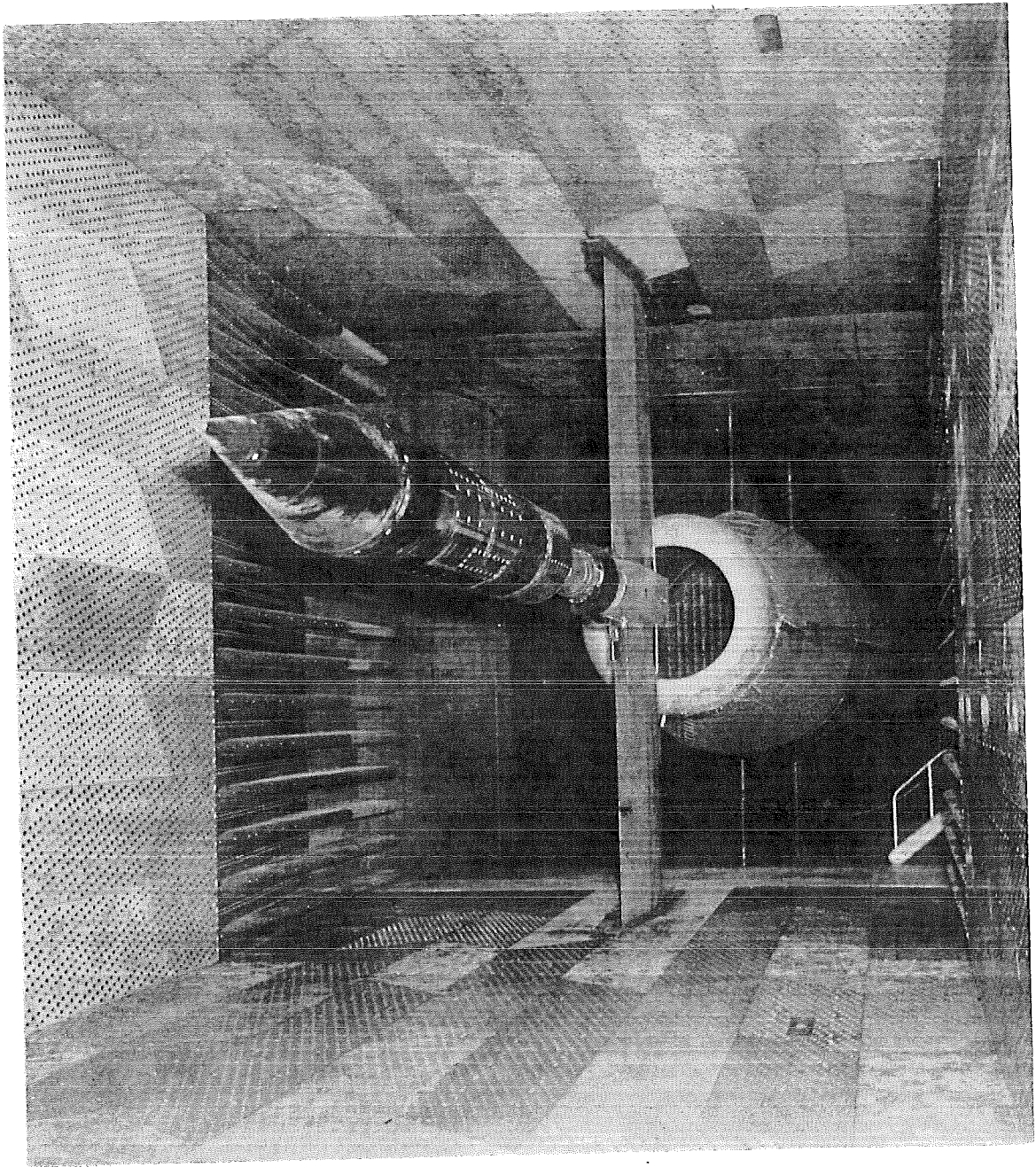
Fig. 2 Typical Model Installation

All Dimensions In Feet

20°

1.800

5.104

17.975

10.0 D CONE CYLINDER

20°

1.800

5.104

15.275

8.5 D CONE CYLINDER

x

r

1.800

5.400

15.300
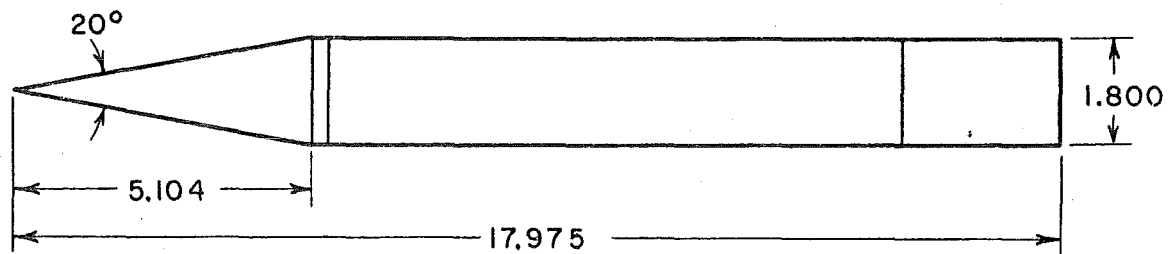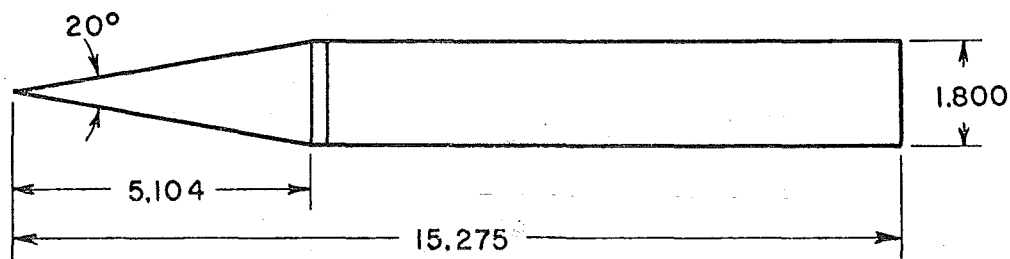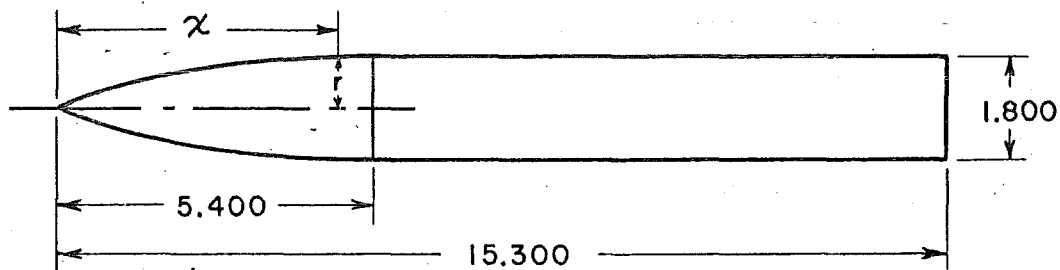
8.5 D OGIVE CYLINDER

Ogive Nose Profile (AGARD):

$$r = \frac{x}{3}\left[1 - \frac{1}{9}\left(\frac{x}{D}\right)^2 + \frac{1}{54}\left(\frac{x}{D}\right)^3\right]$$

where D = 1.800, length = 3D

Fig. 3 Details of Model Configurations
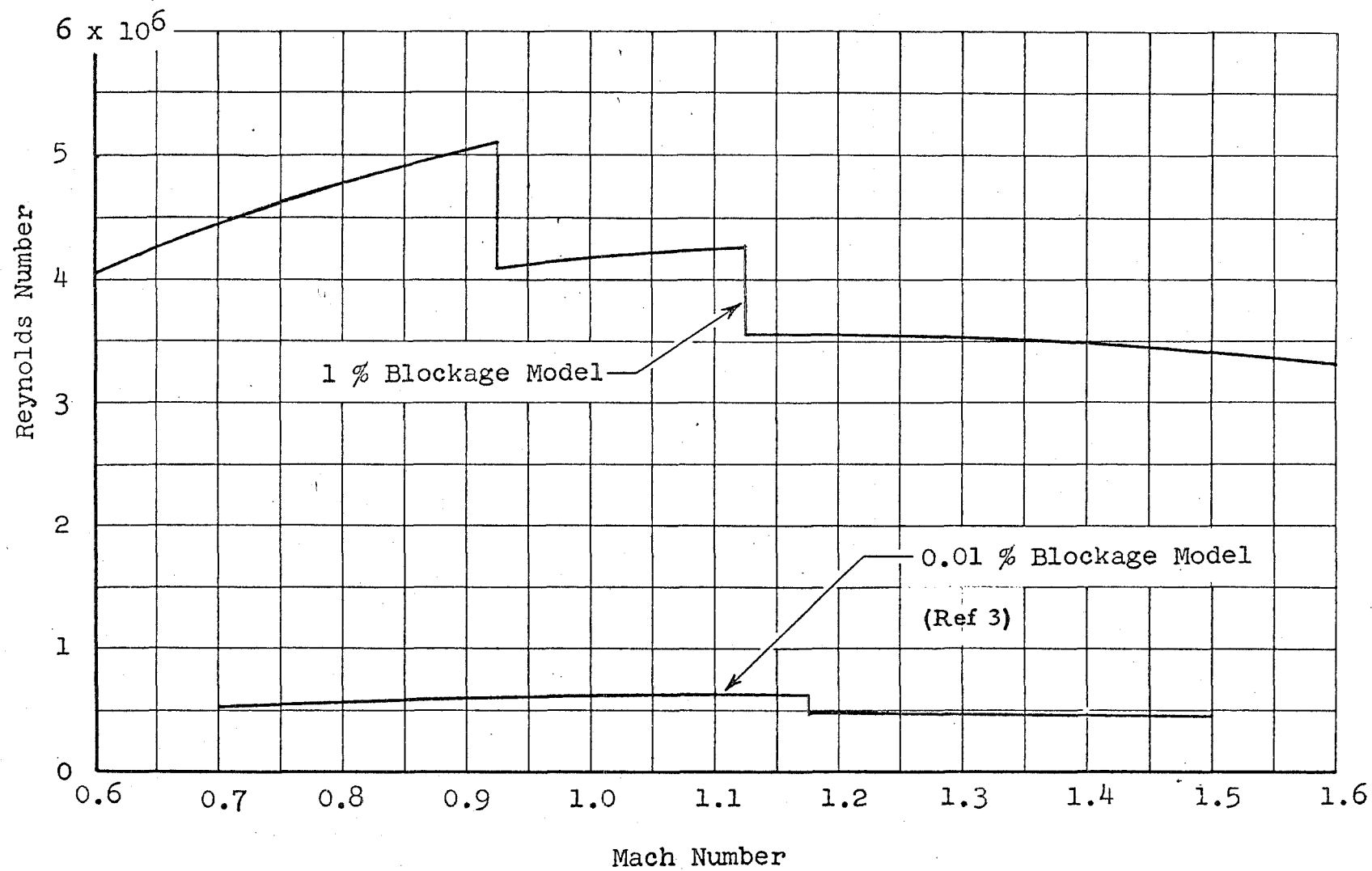
Fig. 4 Test Reynolds Numbers, Based on Body Diameter, for 1-Percent and 0.01-Percent Blockage Models
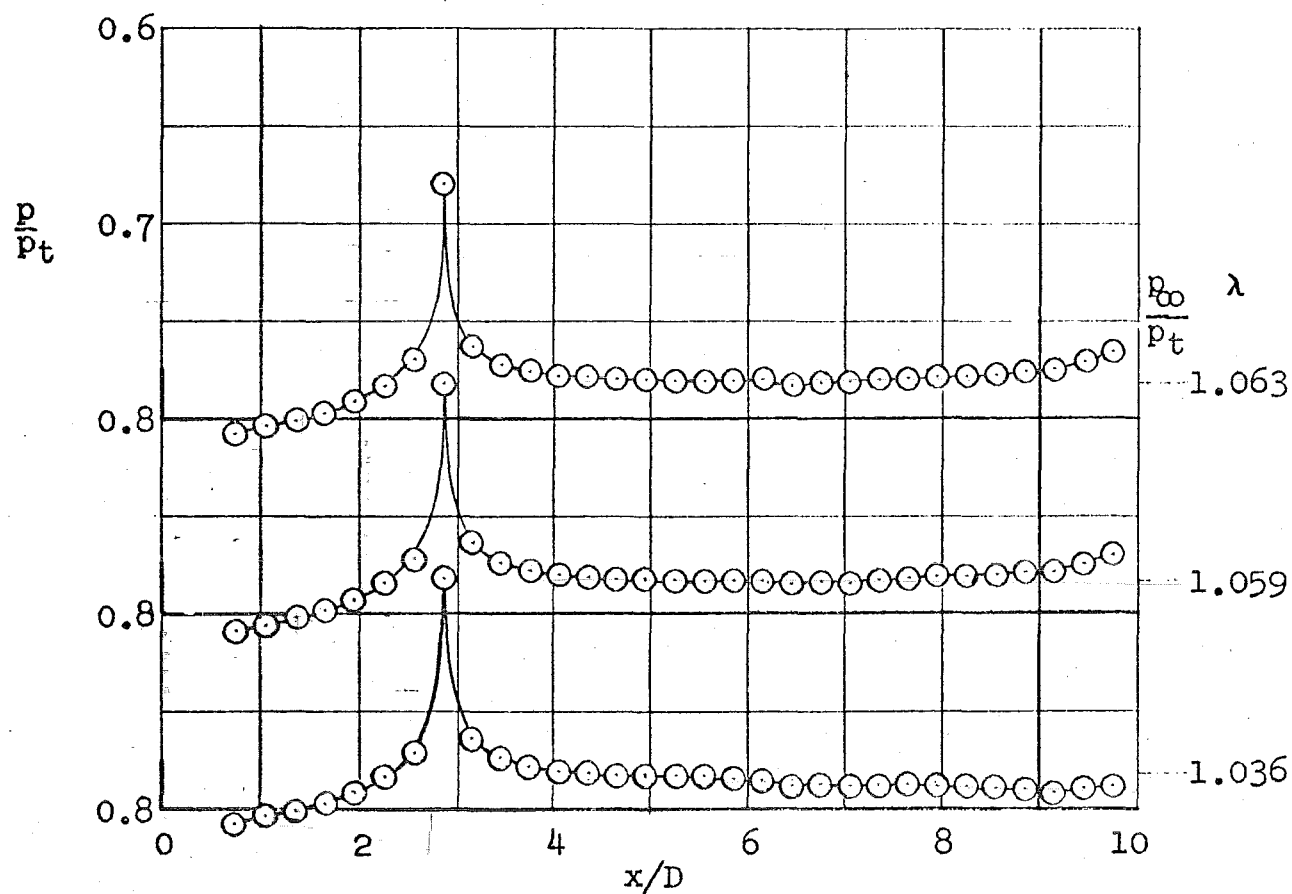
a. θ_w = 0 deg, λ = Variable

Fig. 5 Pressure Distributions on 10.0-diam Cone-Cylinder
at M_∞ = 0.60
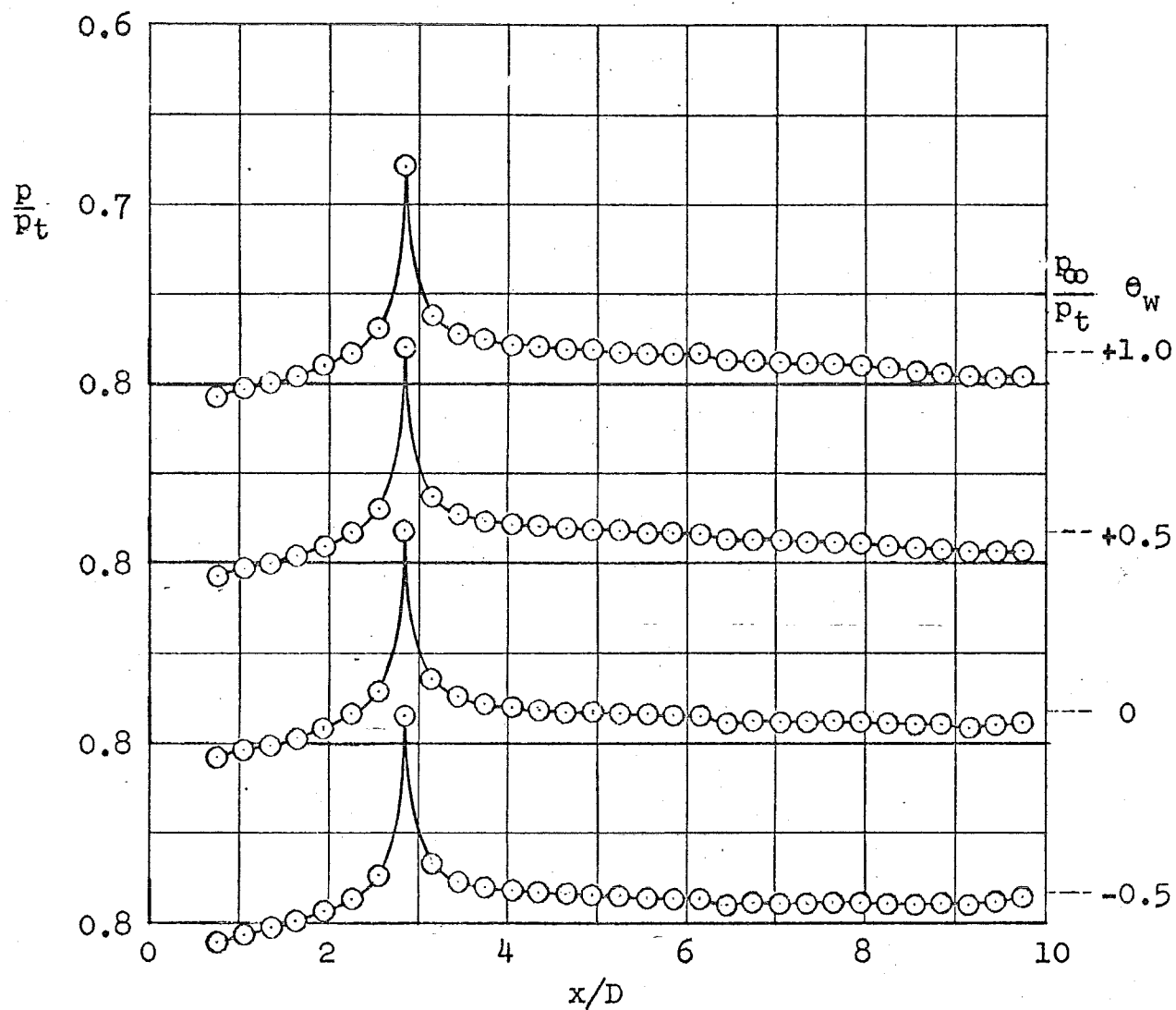
b. $\lambda = 1.036$, θ_w = Variable

Fig. 5 Concluded
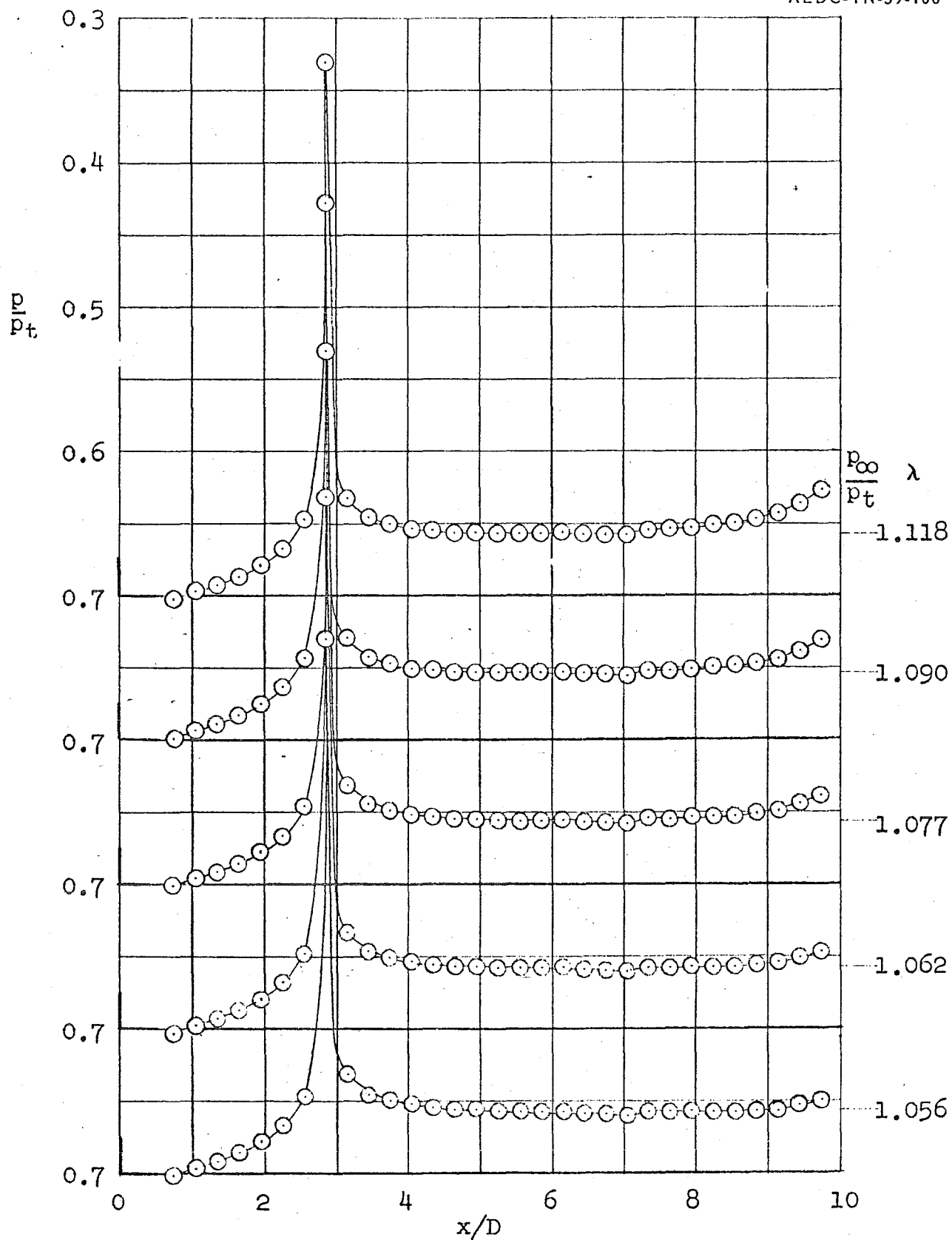
a. $\theta_w = -0.5$ deg, λ = Variable

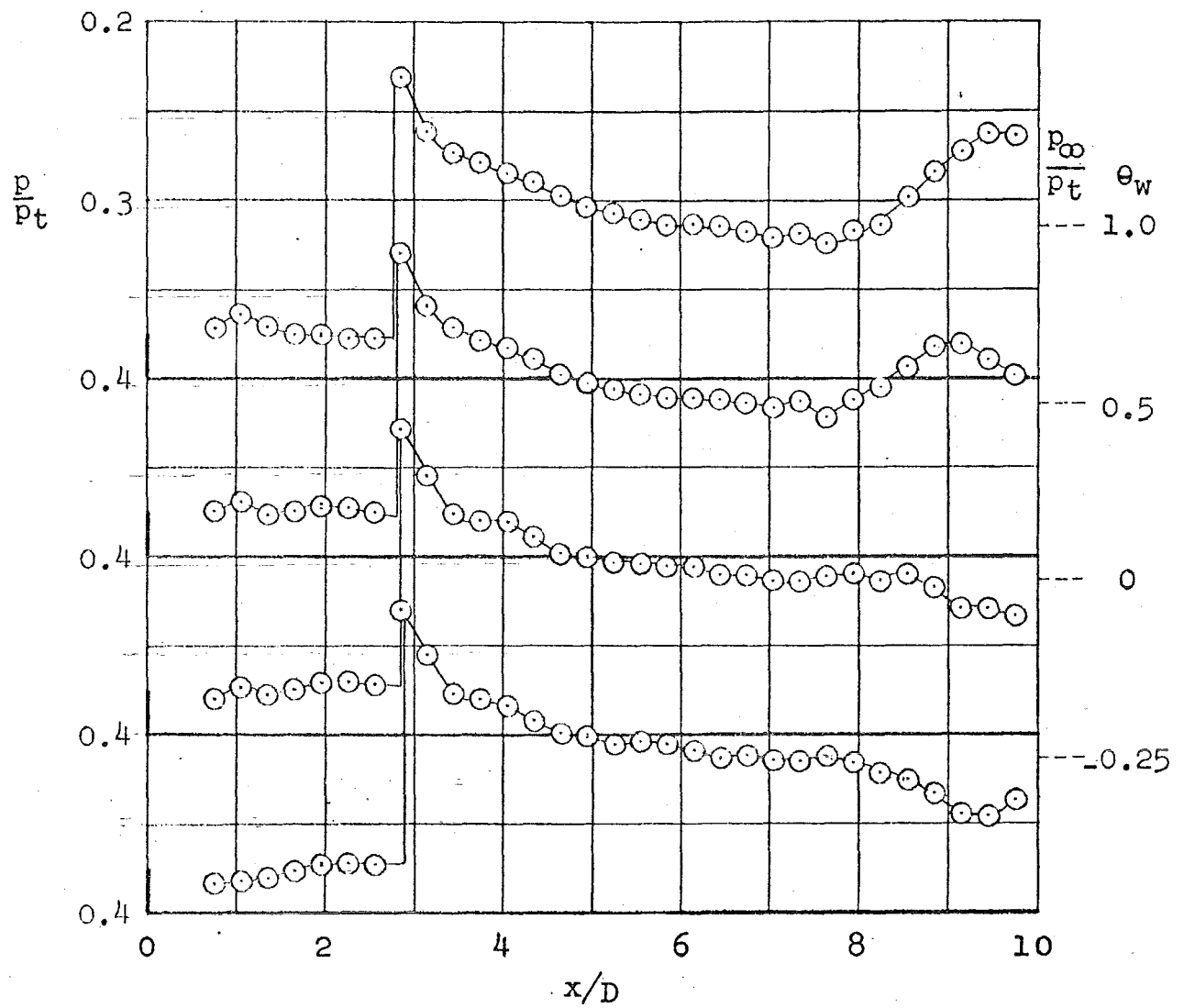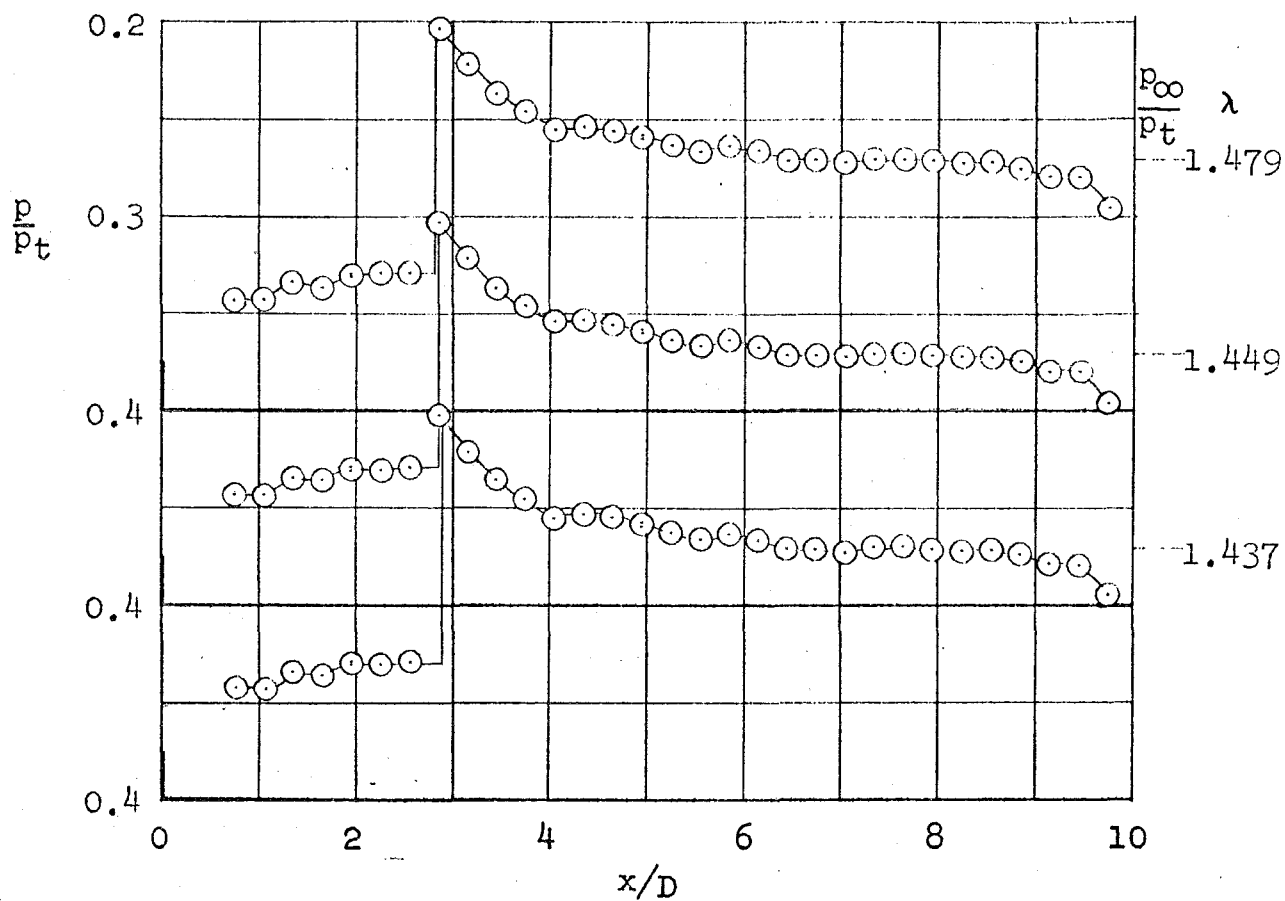Fig. 6 Pressure Distributions on 10.0-diam Cone-Cylinder at $M_\infty = 0.80$
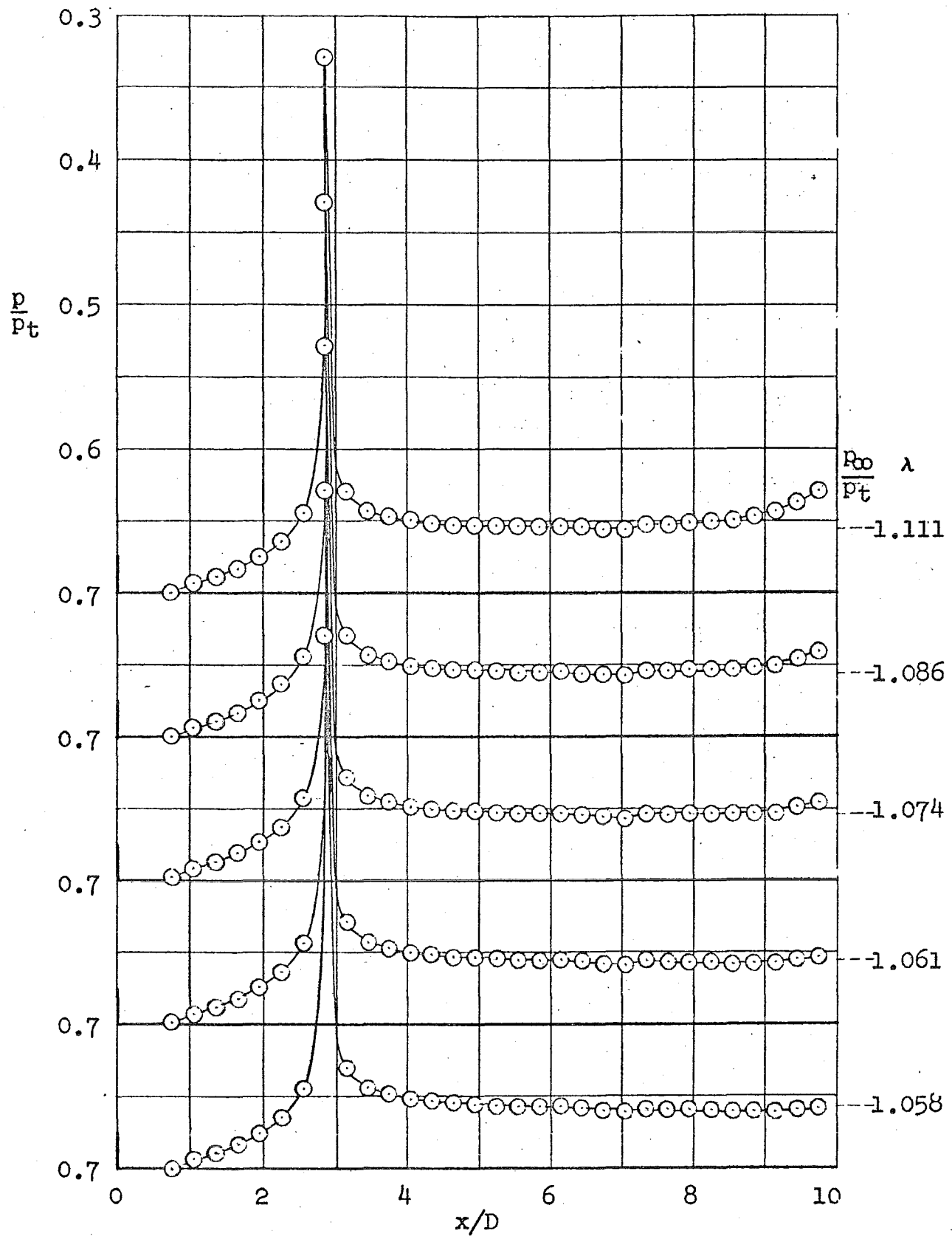
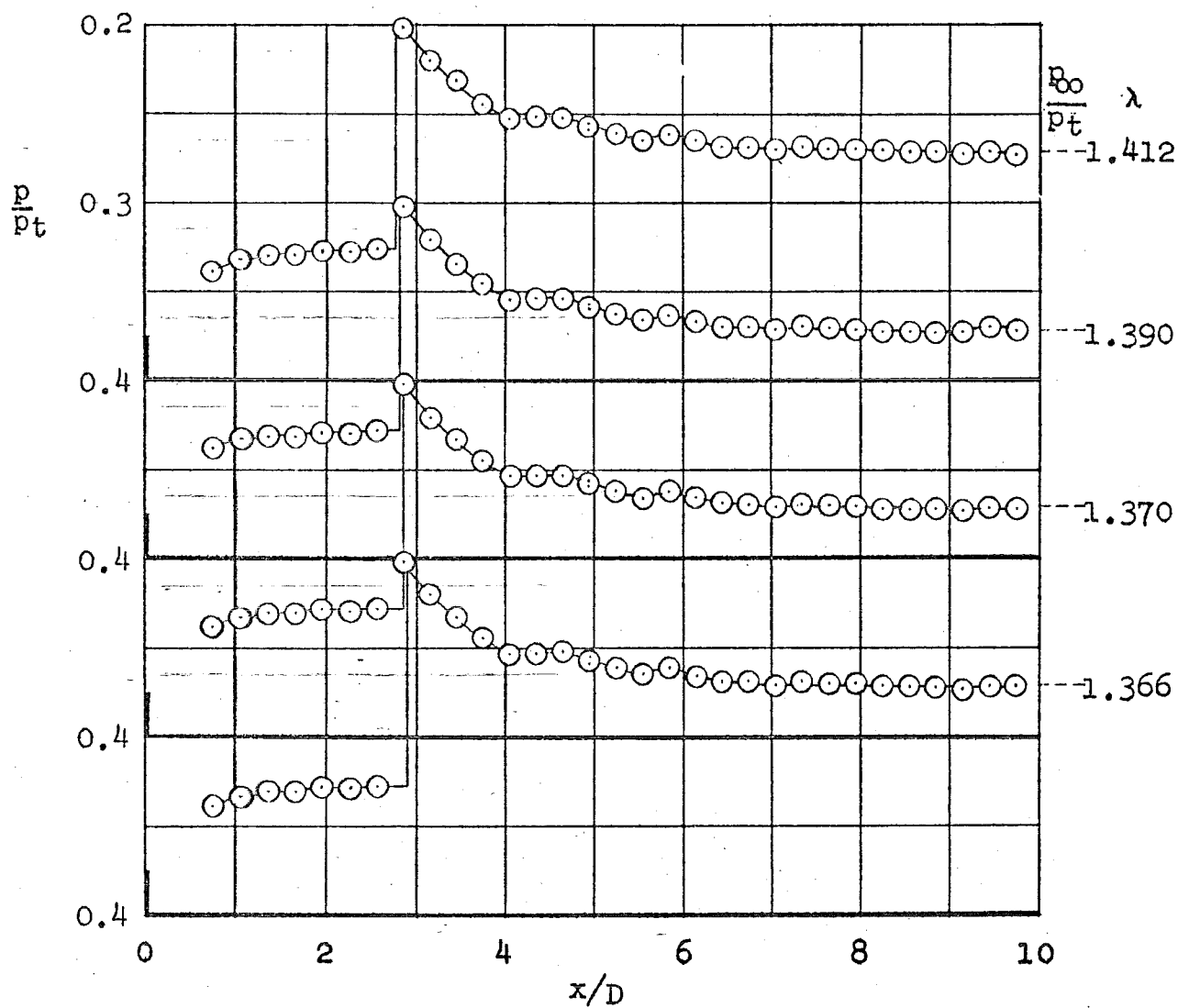b. $\theta_w = 0$ deg, λ = Variable
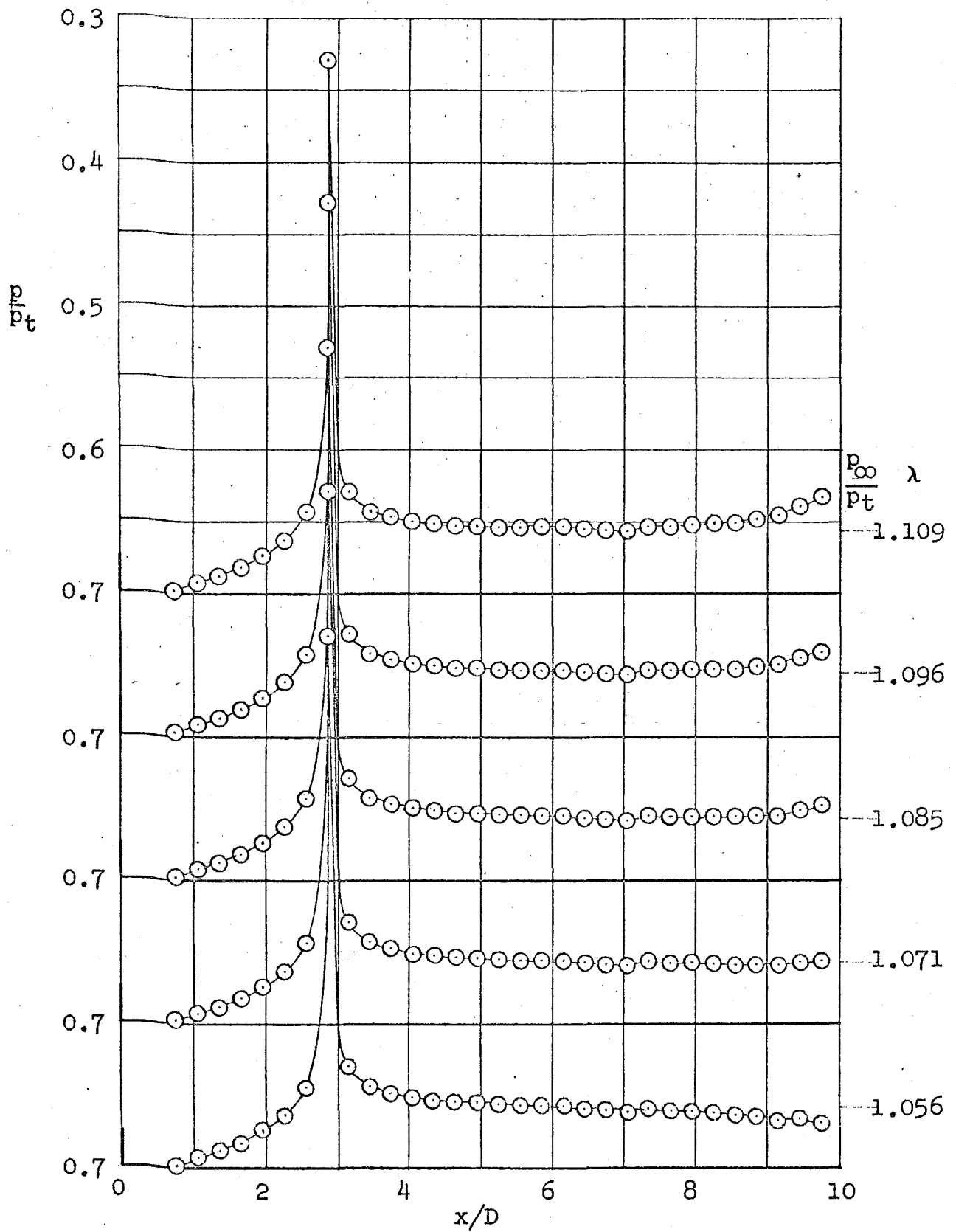
Fig. 6 Continued

c. $\theta_w = +0.5$ deg, λ = Variable

Fig. 6 Continued

d. $\theta_w = +1.0$ deg, λ = Variable

Fig. 6 Continued
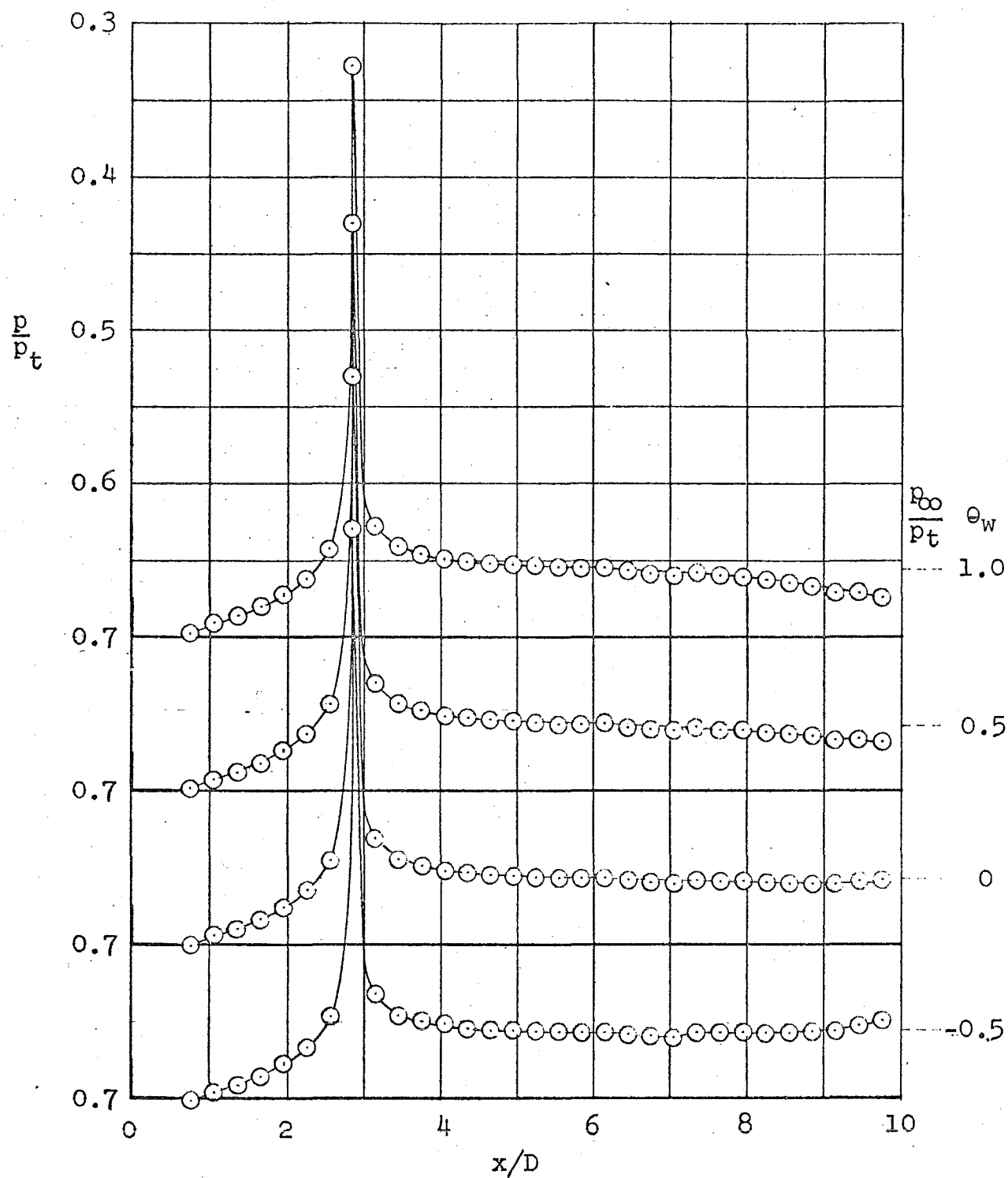
e. $\lambda = 1.056$, θ_w = Variable

Fig. 6 Concluded
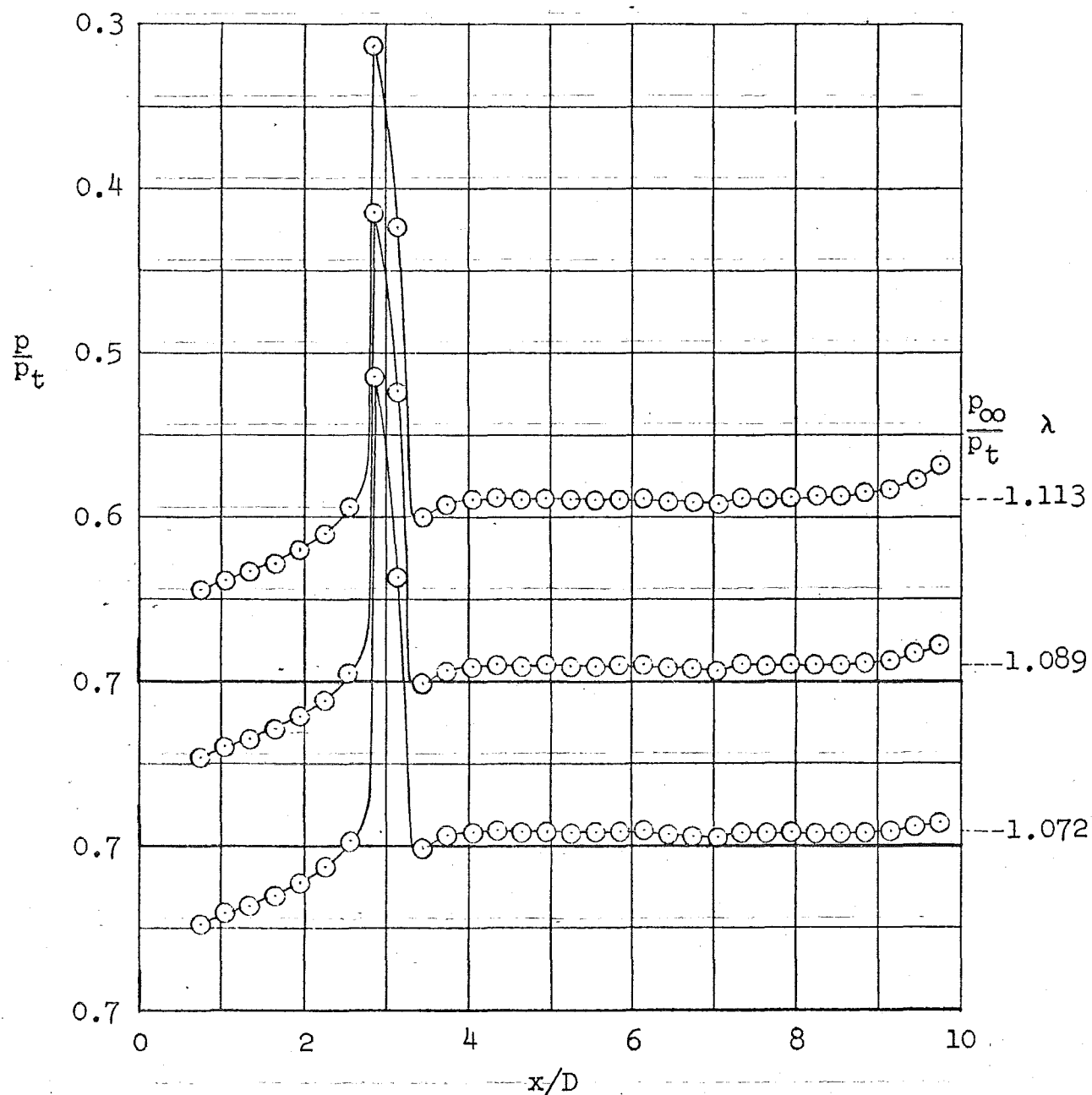
a. $\theta_w = 0$ deg, λ = Variable

Fig. 7 Pressure Distributions on 10.0-diam Cone -Cylinder
at $M_\infty = 0.90$
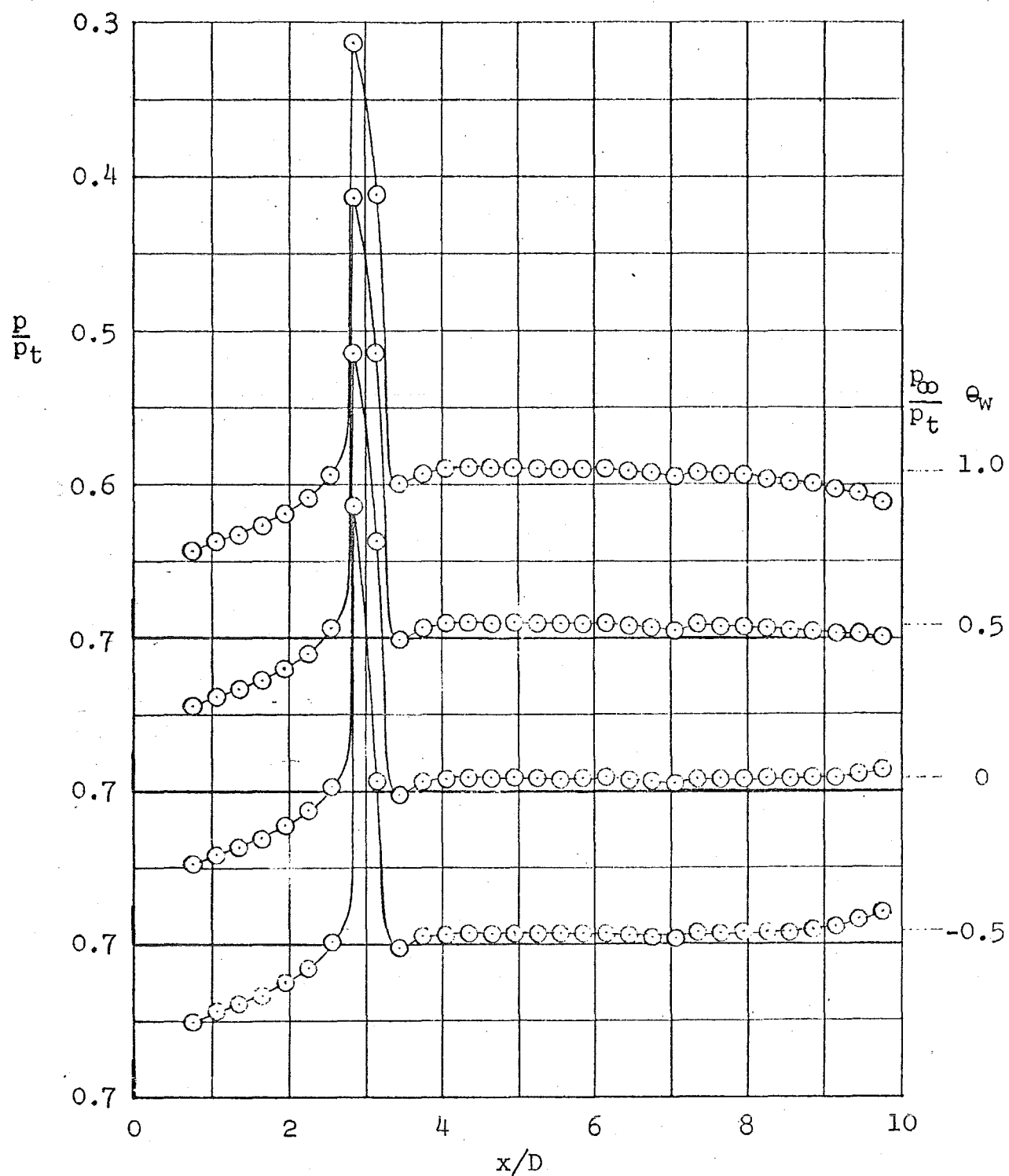
b. $\lambda = 1.075$, θ_w = Variable

Fig. 7 Concluded
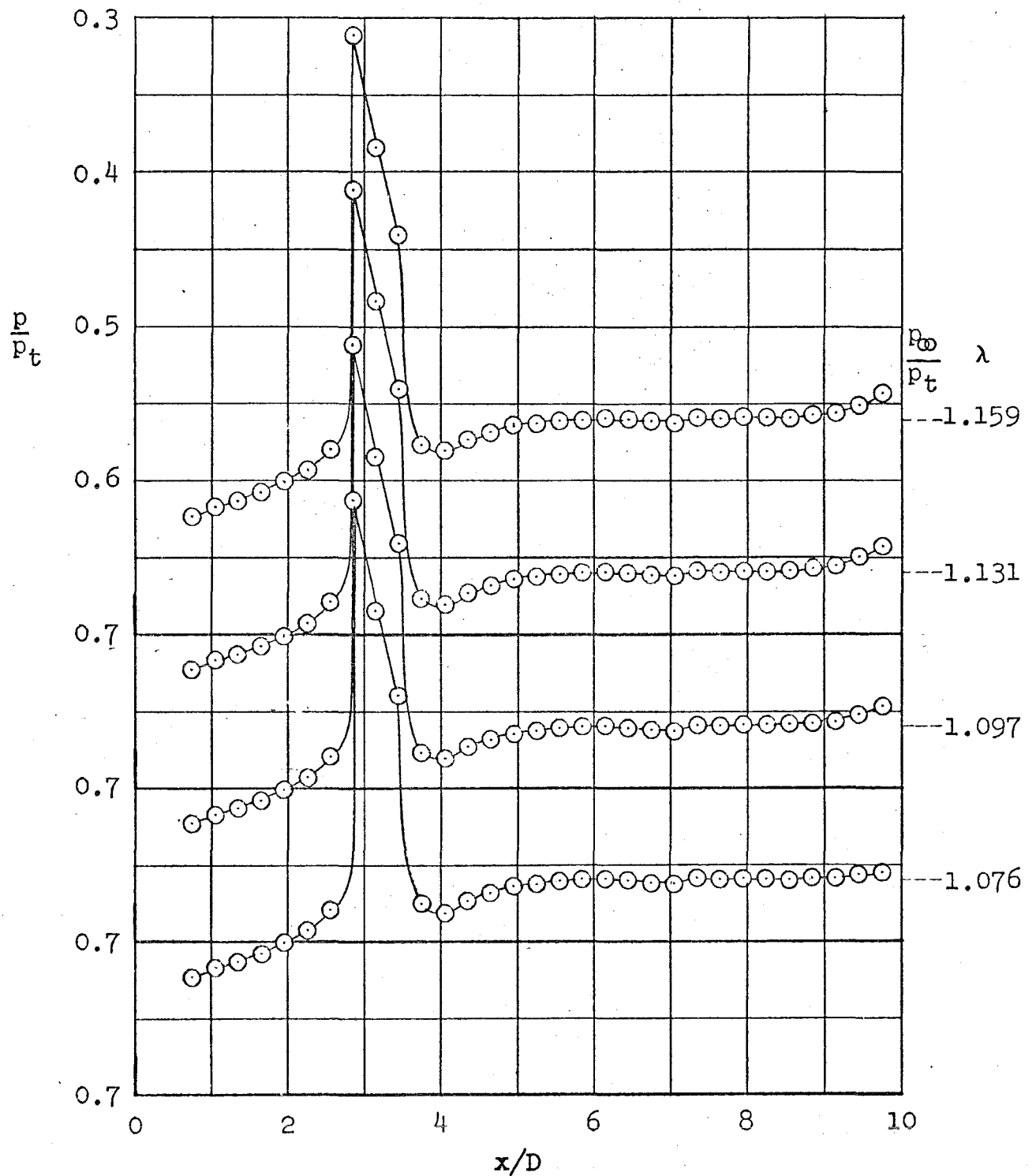
a. $\theta_w = 0$ deg, λ = Variable

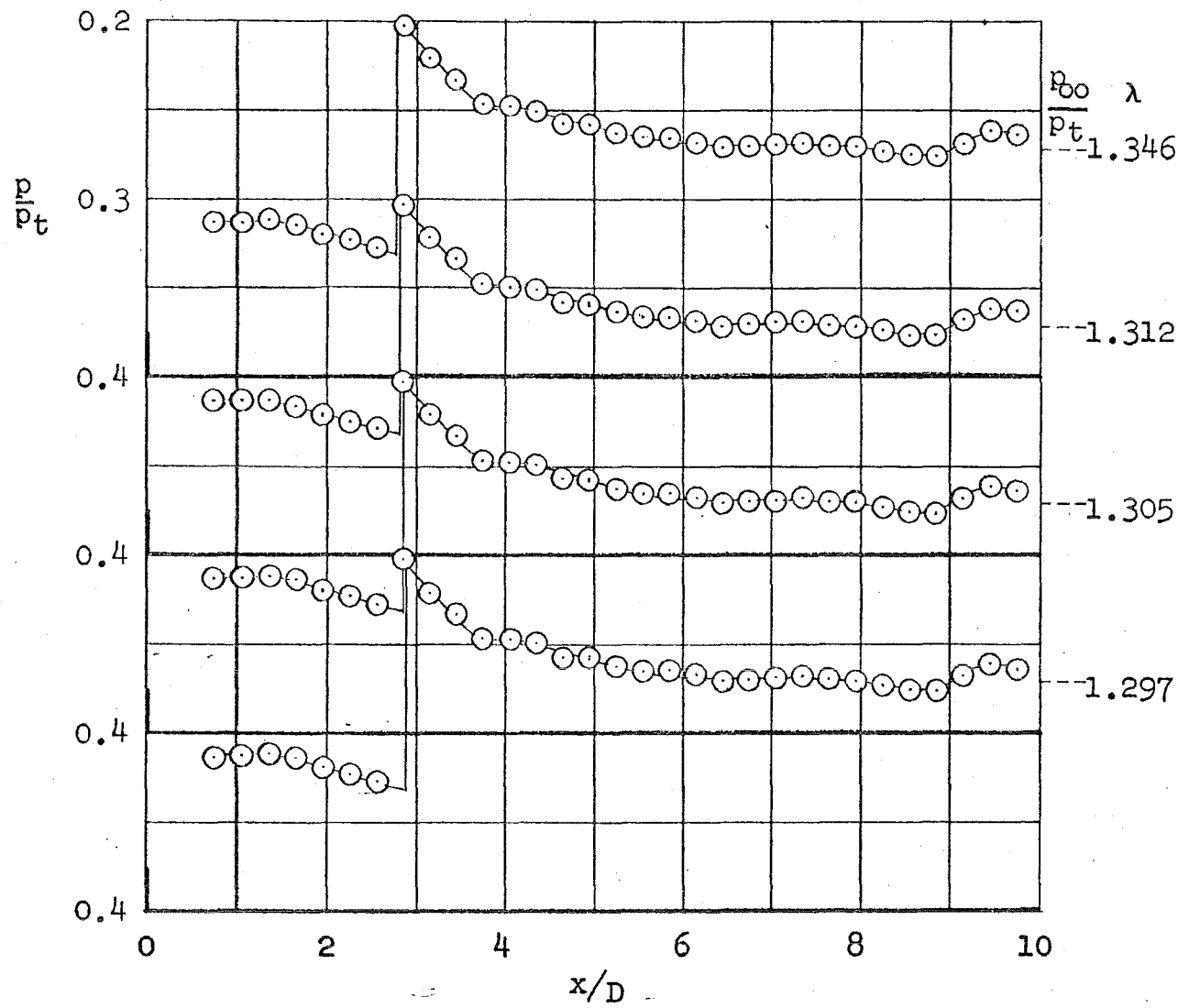Fig. 8 Pressure Distributions on 10.0-diam Cone-Cylinder
at $M_\infty = 0.95$
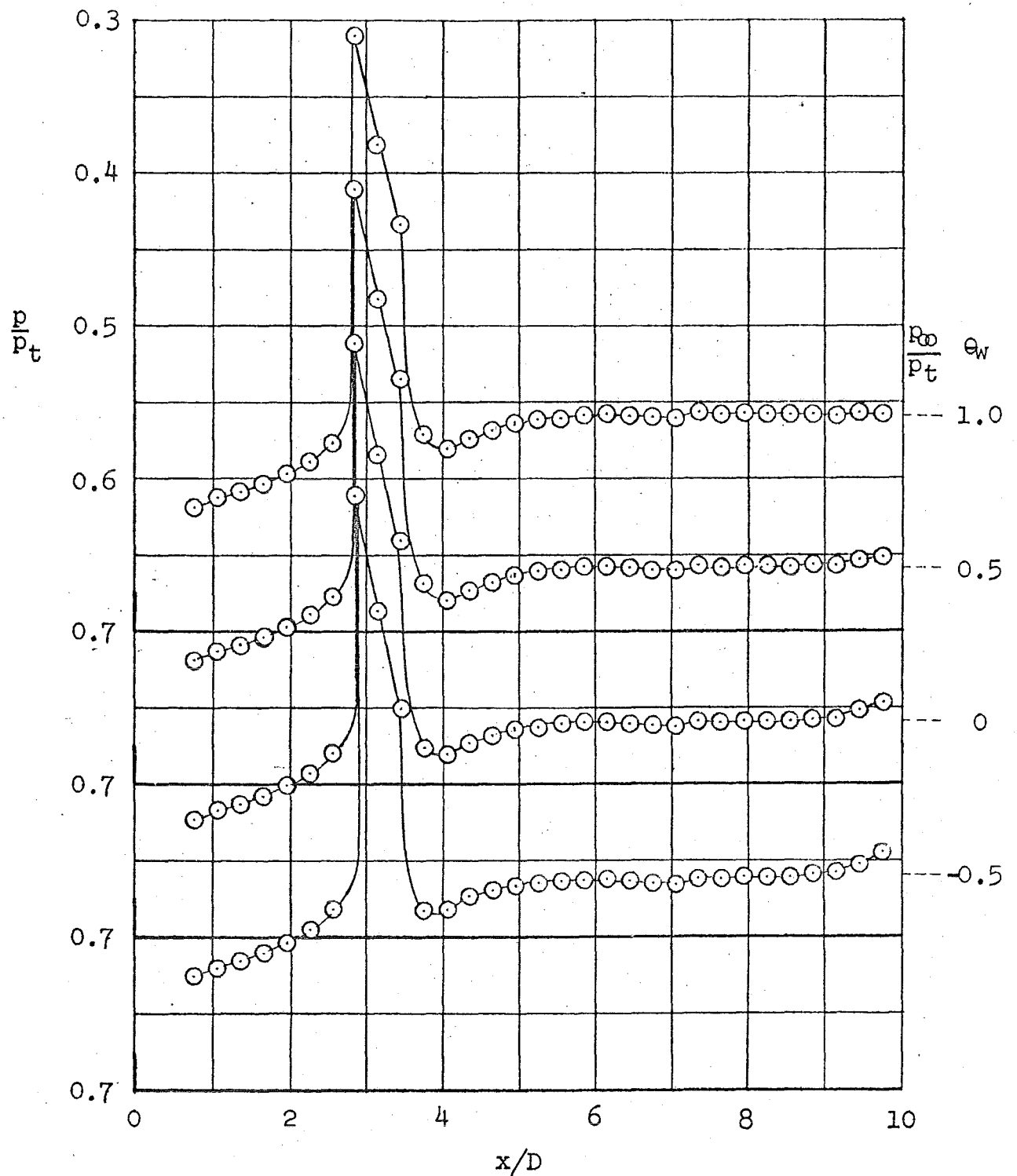
b. $\lambda = 1.100$, $\theta_w = $ Variable

Fig. 8 Concluded
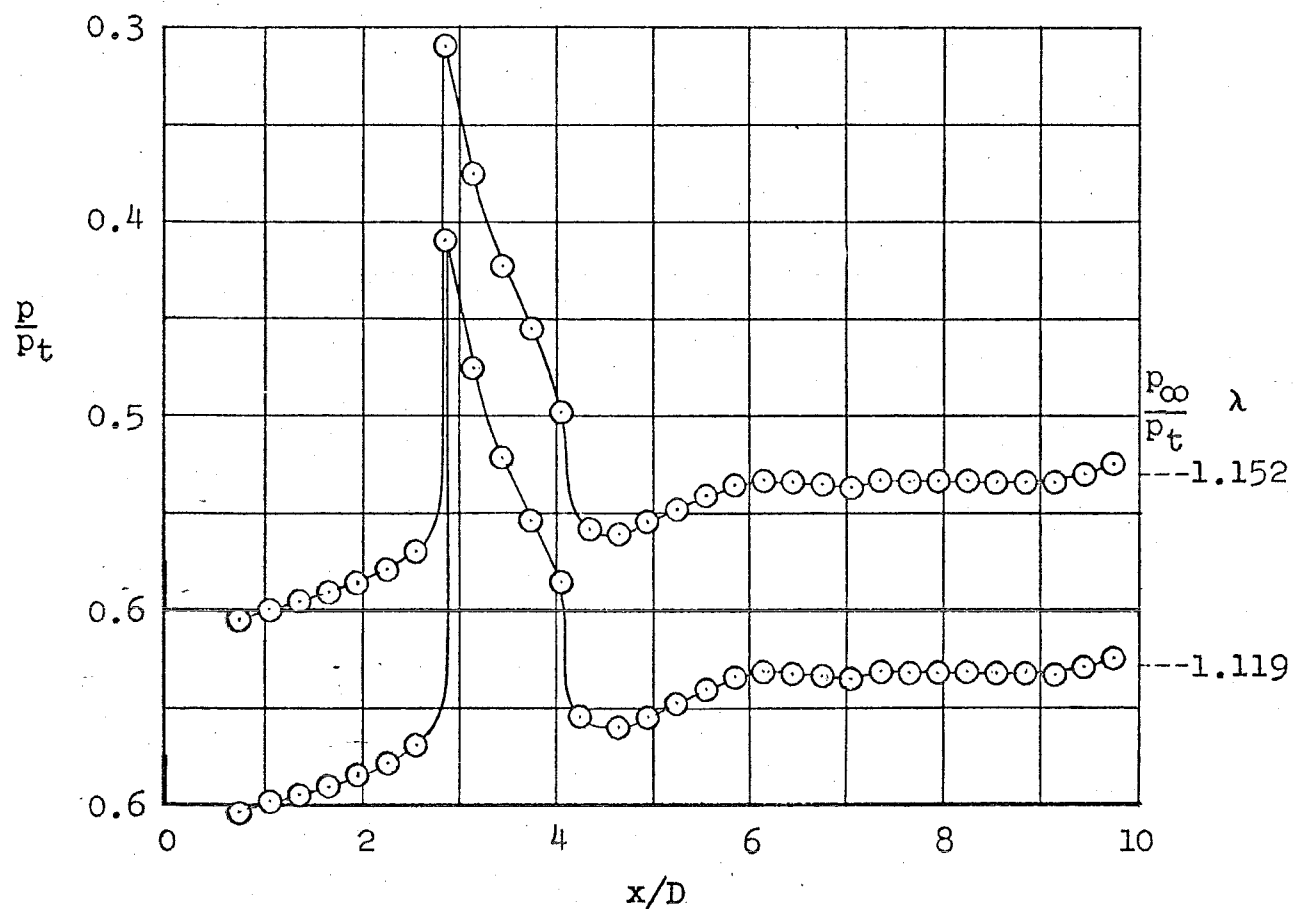
a. $\theta_w = -0.5$ deg, λ = Variable

Fig. 9 Pressure Distributions on 10.0-diam Cone-Cylinder
at $M_\infty = 1.00$
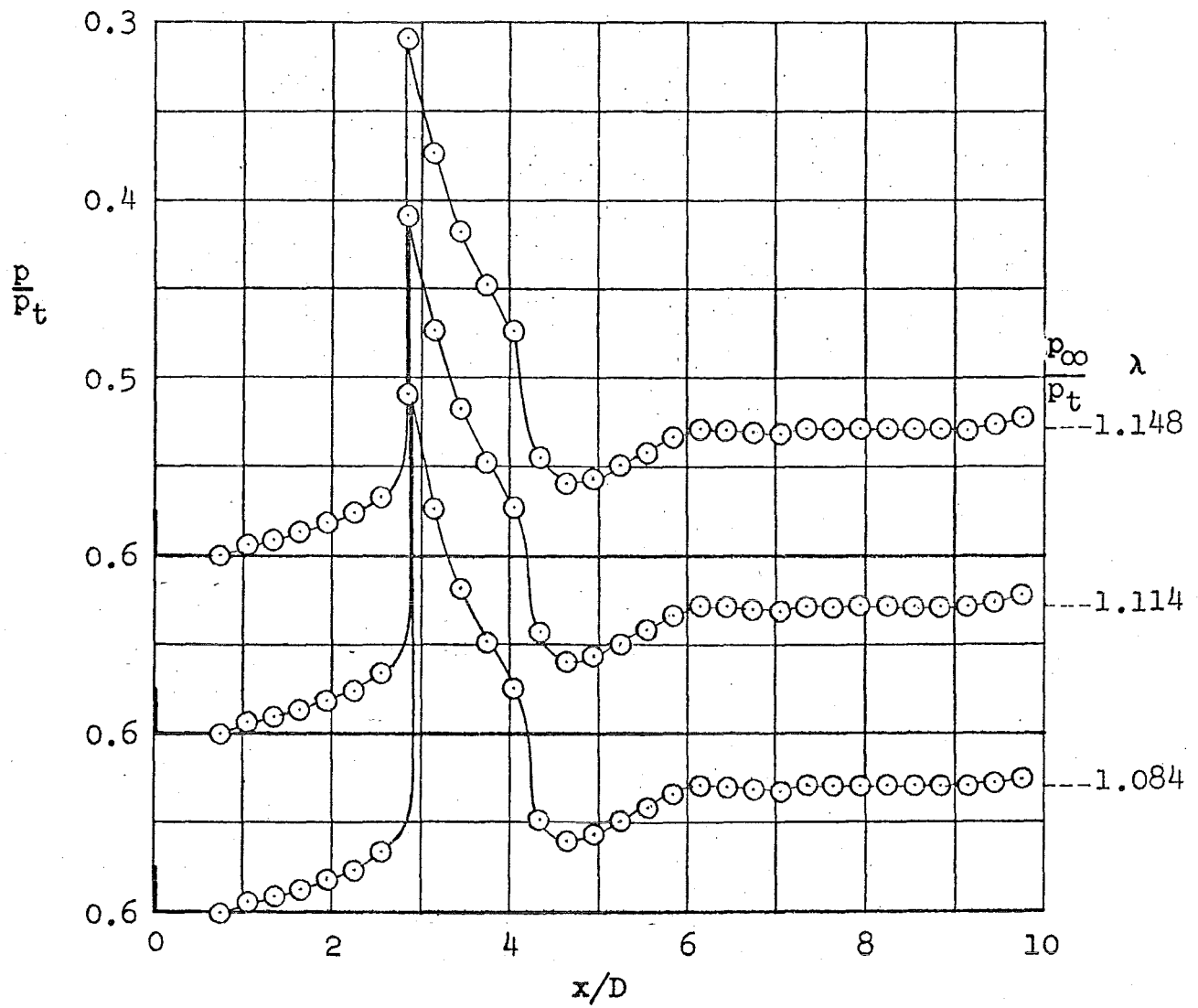
b. $\theta_w = 0$ deg, λ = Variable
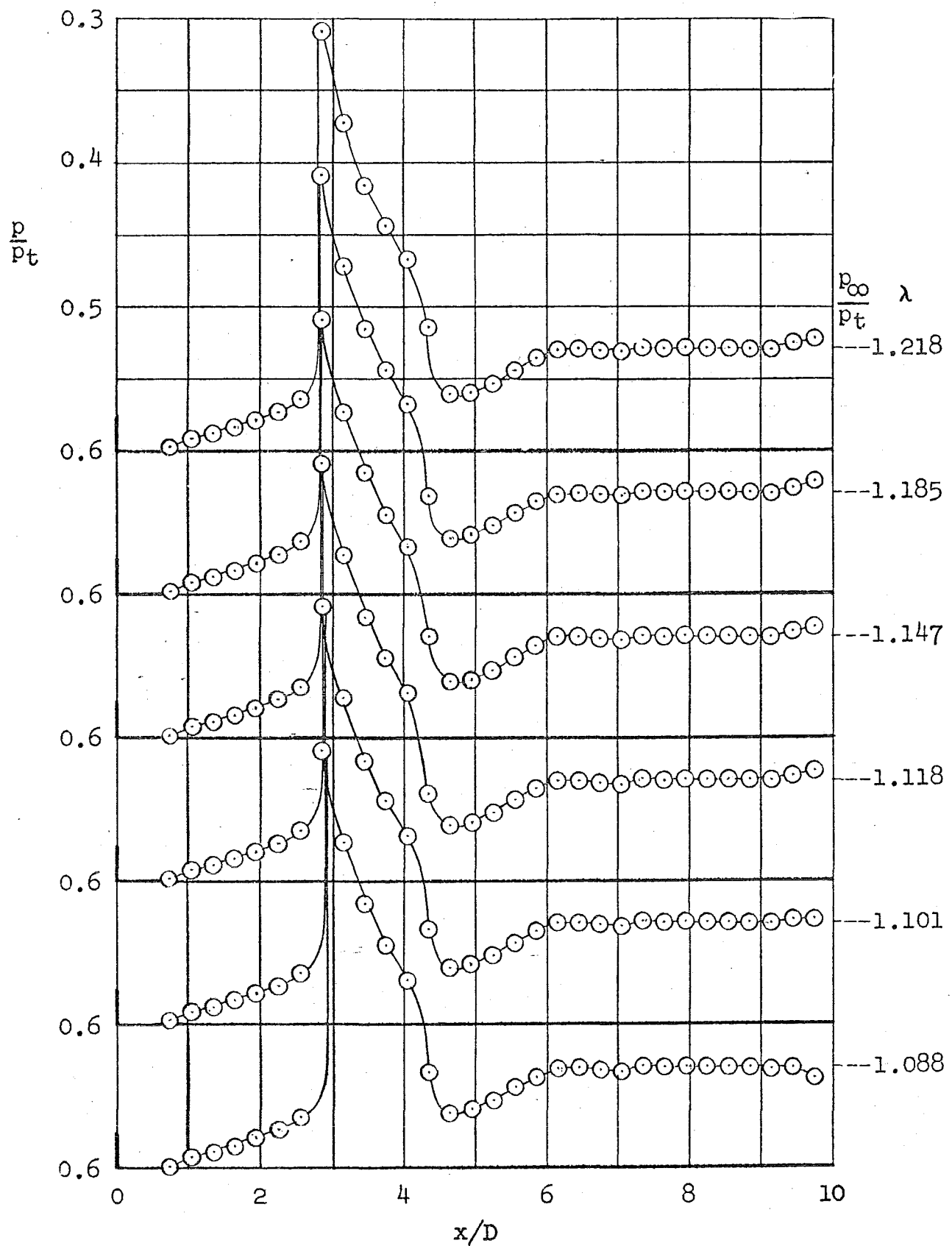
Fig. 9 Continued

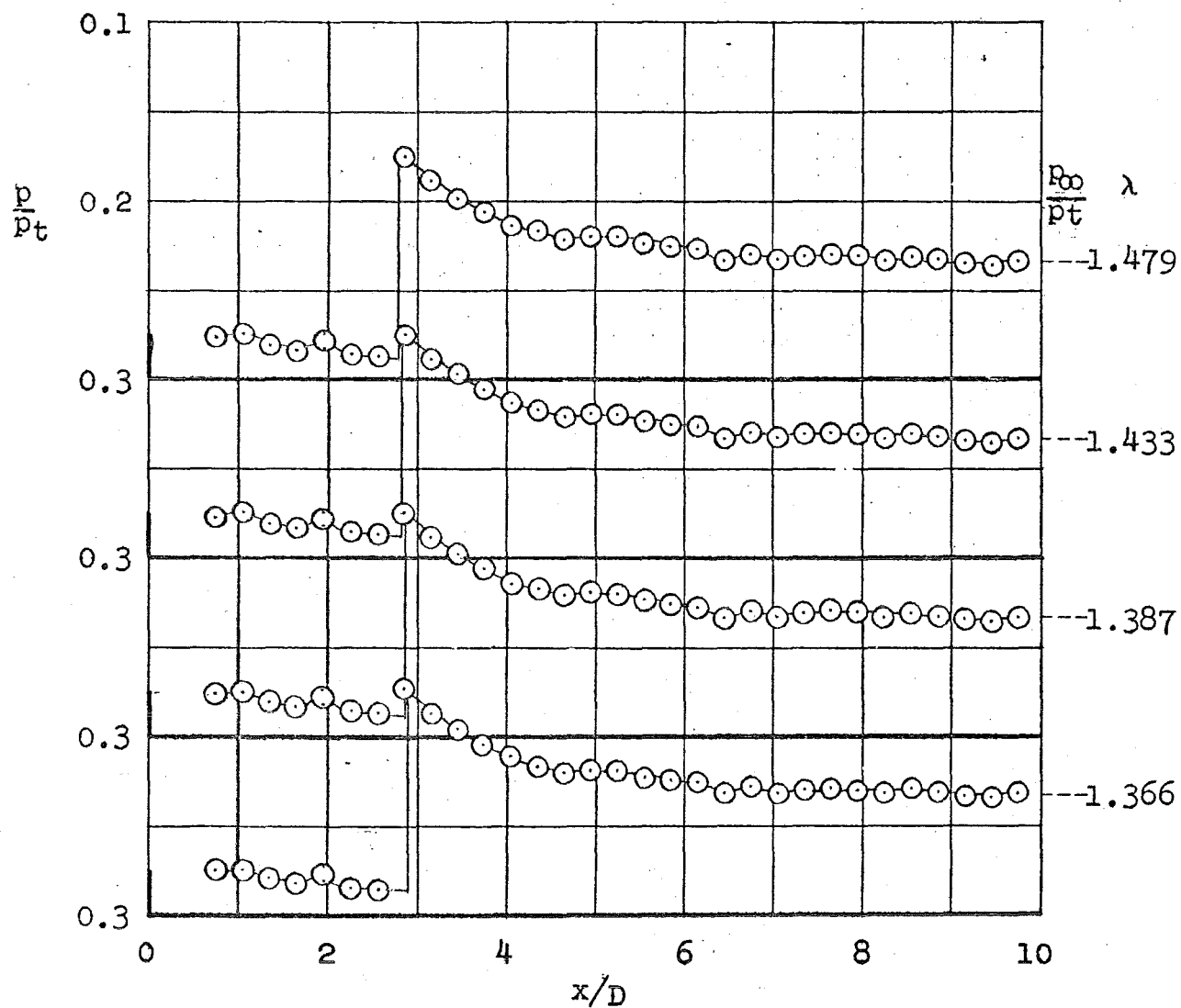c. $\theta_w = +0.5$ deg, λ = Variable

Fig. 9 Continued

d. $\theta_w = +1.0$ deg, λ = Variable

Fig. 9 Continued
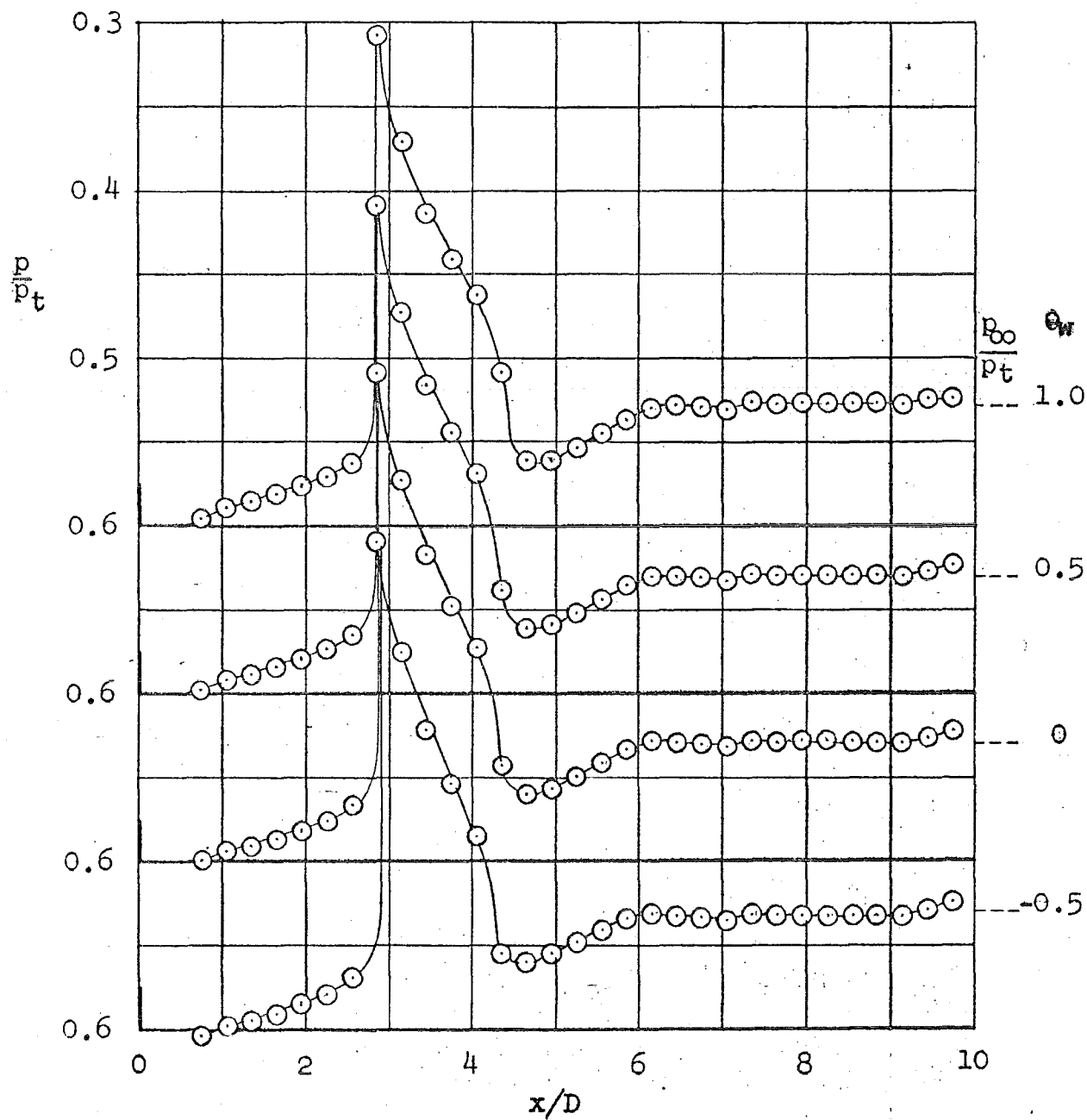
e. $\lambda = 1.117$, θ_w = Variable

Fig. 9 Concluded
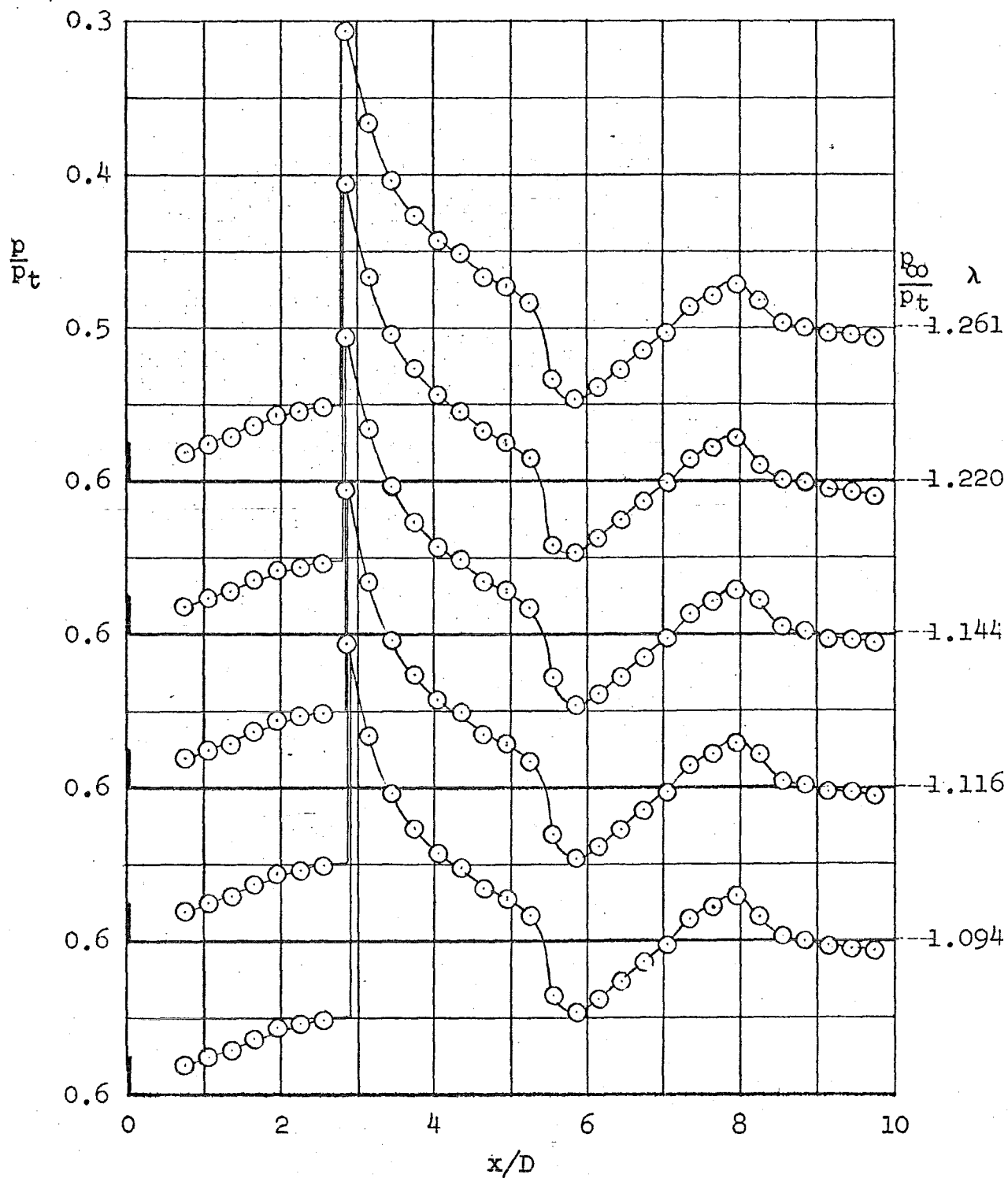
a. $\theta_w = 0$ deg, λ = Variable

Fig. 10 Pressure Distributions on 10.0-diam Cone-Cylinder
         at $M_\infty = 1.05$
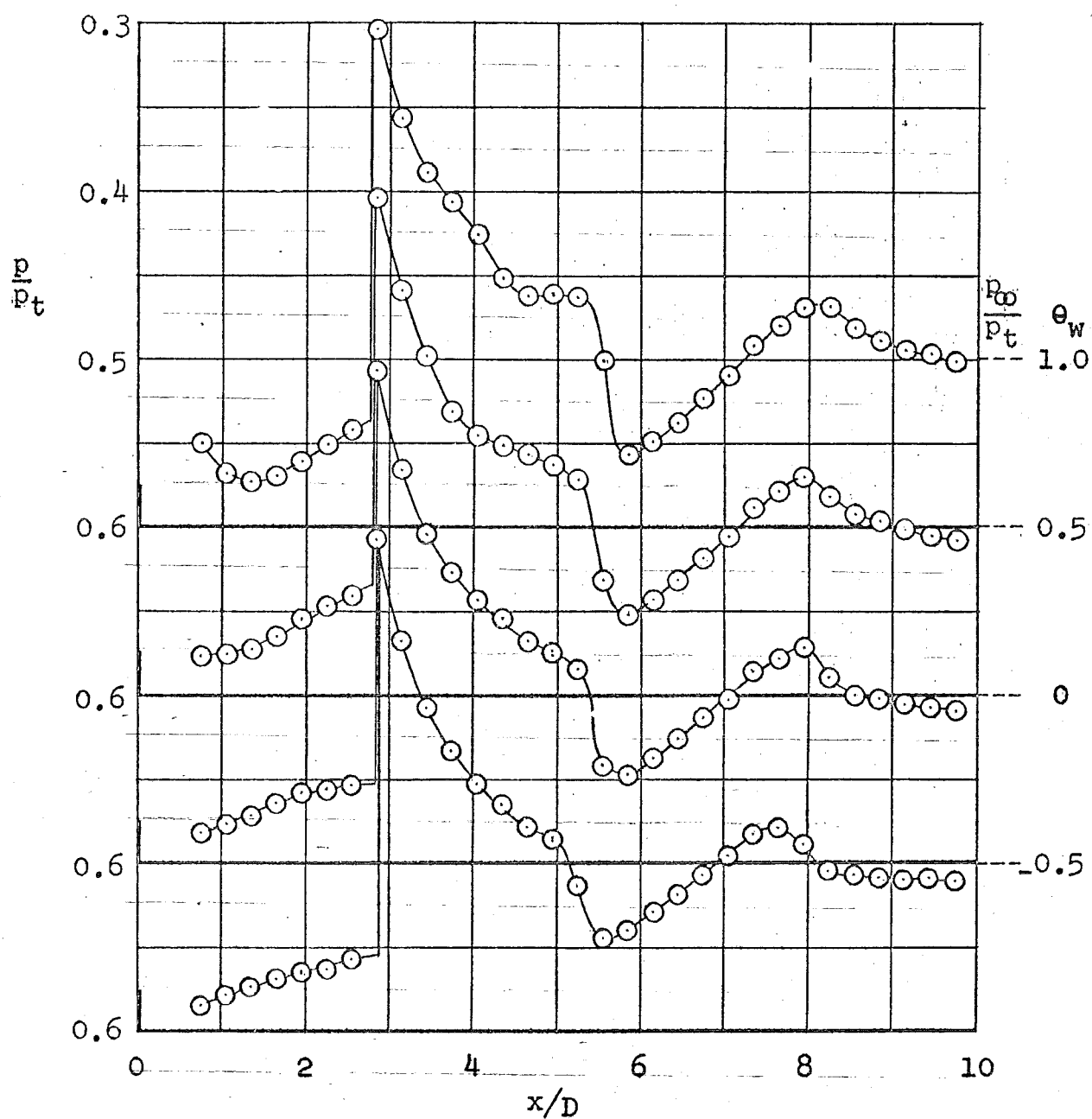
b. $\lambda = 1.22$, θ_w = Variable

Fig. 10 Concluded
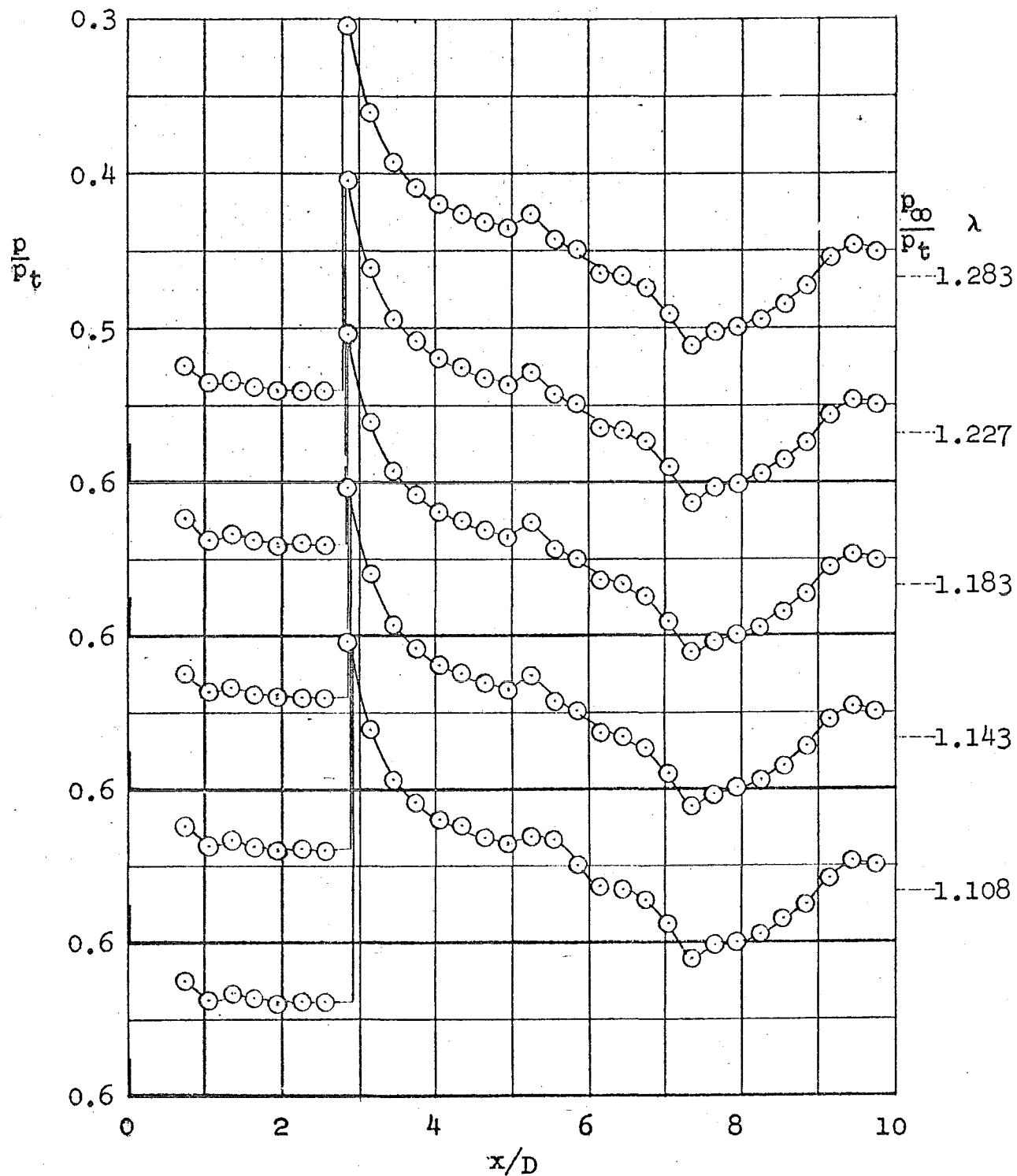
a. $\theta_w = 0$ deg, λ = Variable

Fig. 11 Pressure Distributions on 10.0-diam Cone-Cylinder
at $M_\infty = 1.10$
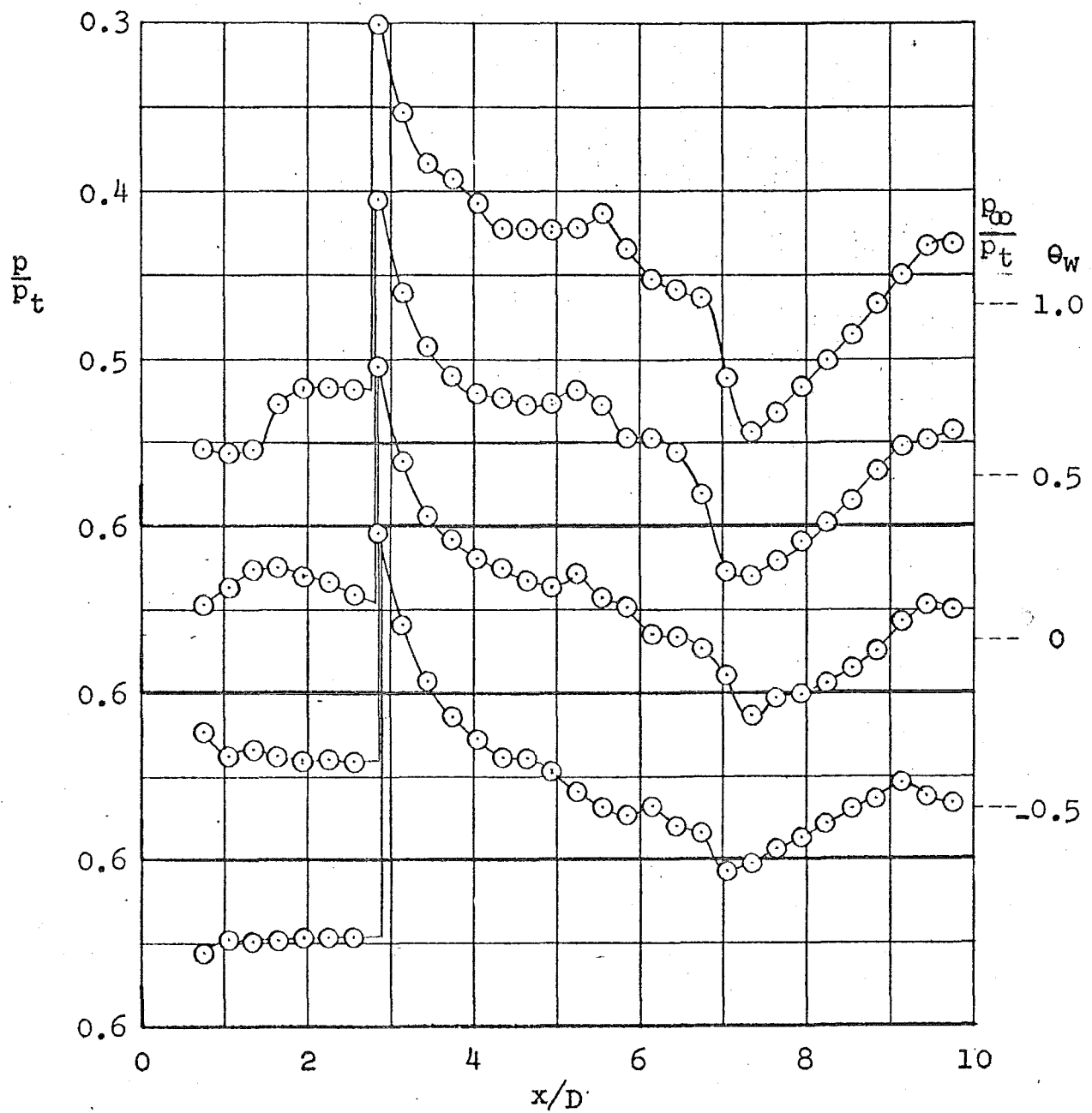
b. $\lambda = 1.23$, θ_w = Variable

Fig. 11 Concluded
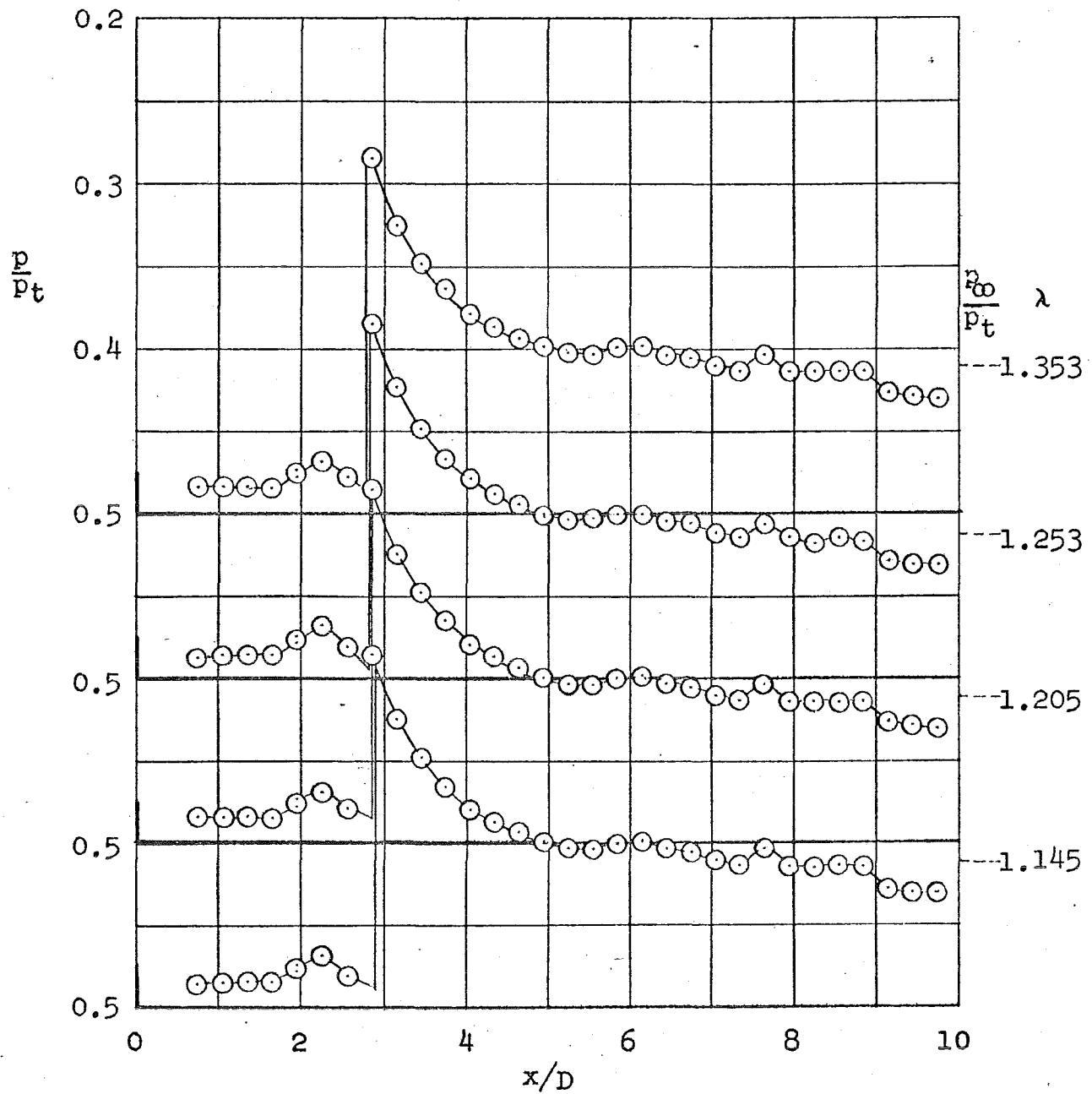
a. $\theta_w = 0$ deg, λ = Variable

Fig. 12 Pressure Distributions on 10.0-diam Cone-Cylinder
at $M_\infty = 1.20$
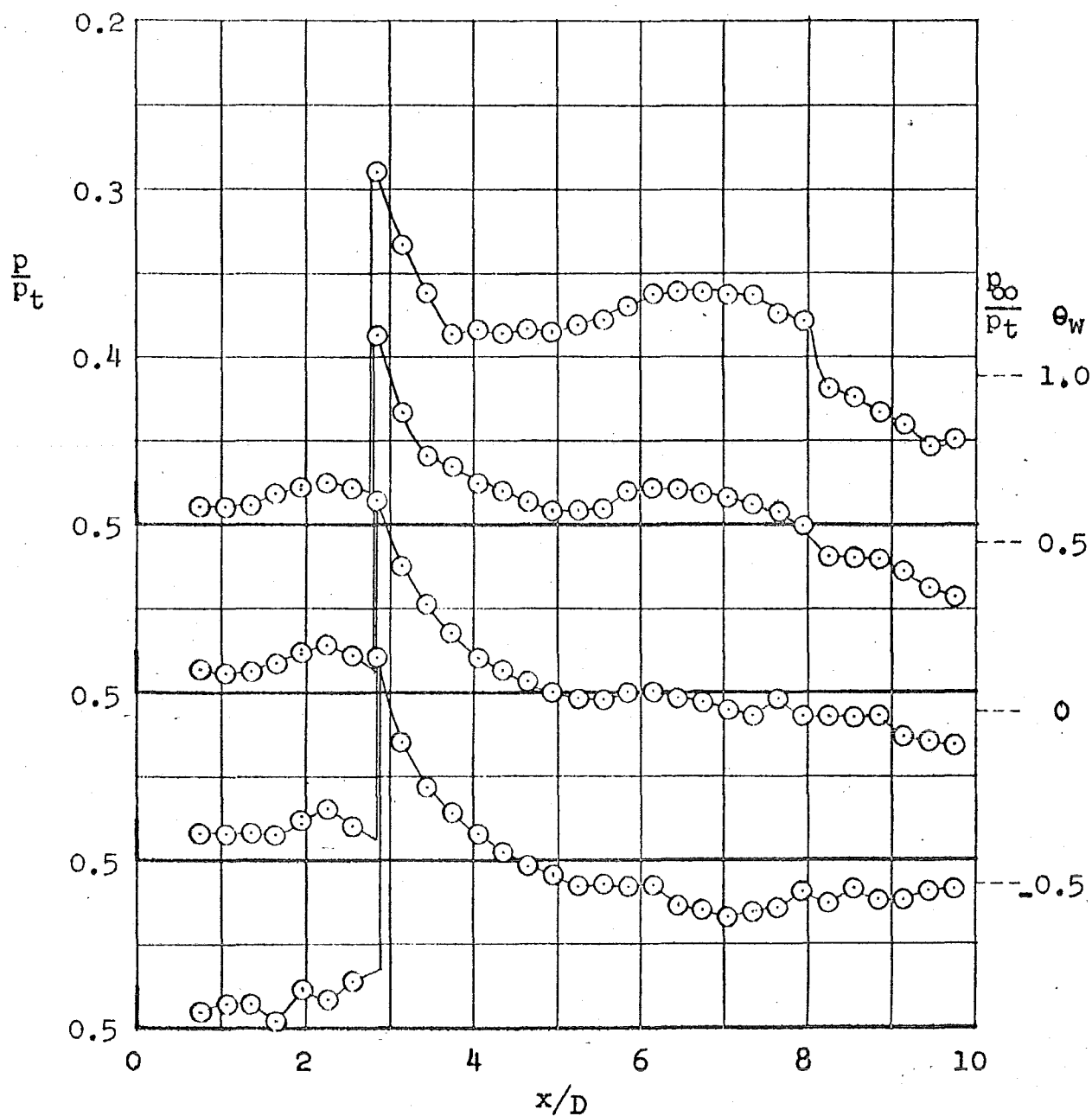
b. $\lambda_{(\theta_w = -0.5)} = 1.418$, $\lambda_{(\theta_w = 0 \text{ through } +1.0)} = 1.20$,

θ_w = Variable

Fig. 12 Concluded
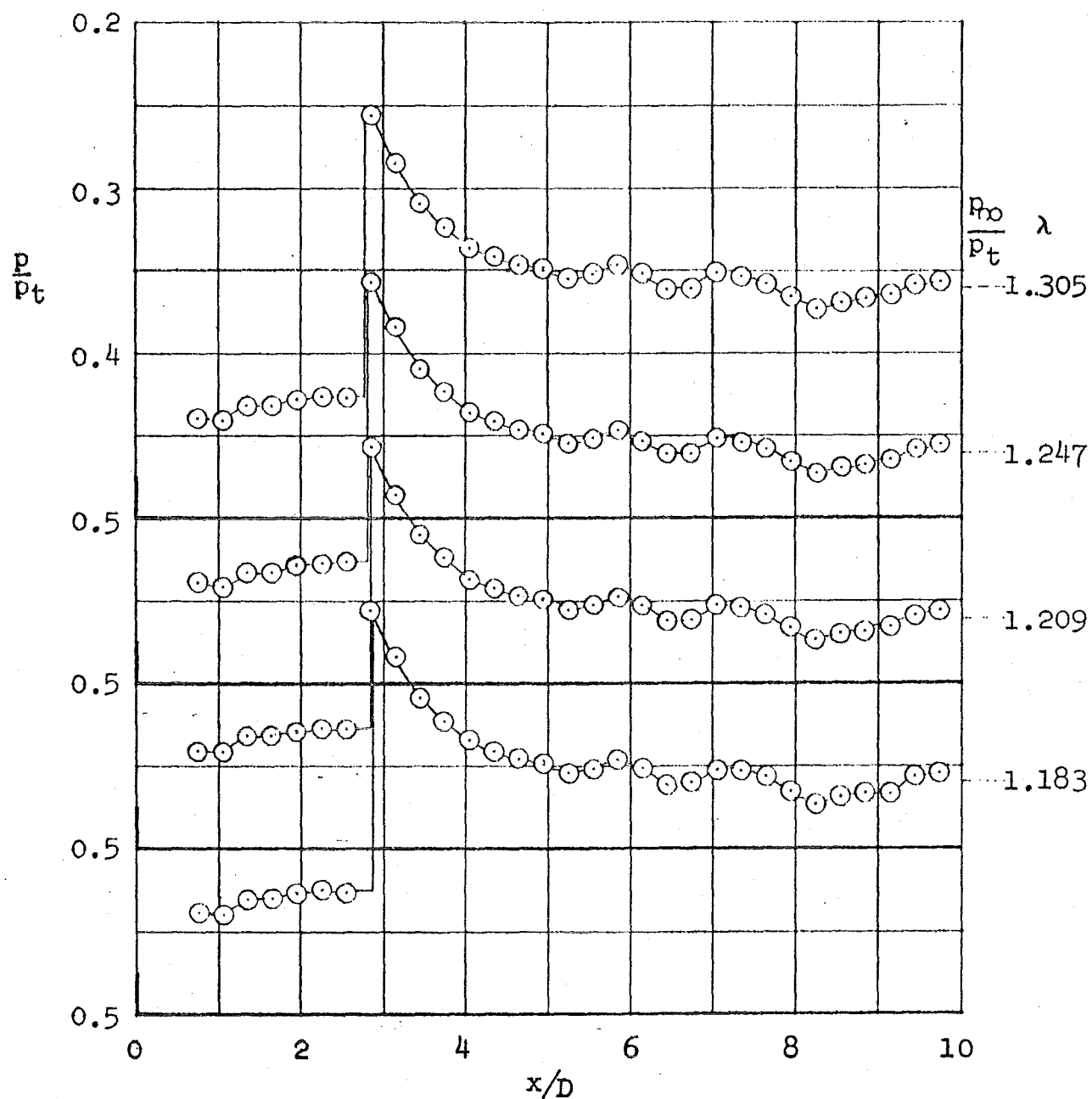
a. $\theta_w = 0$ deg, λ = Variable

Fig. 13 Pressure Distributions on 10.0-diam Cone-Cylinder
at $M_\infty = 1.30$
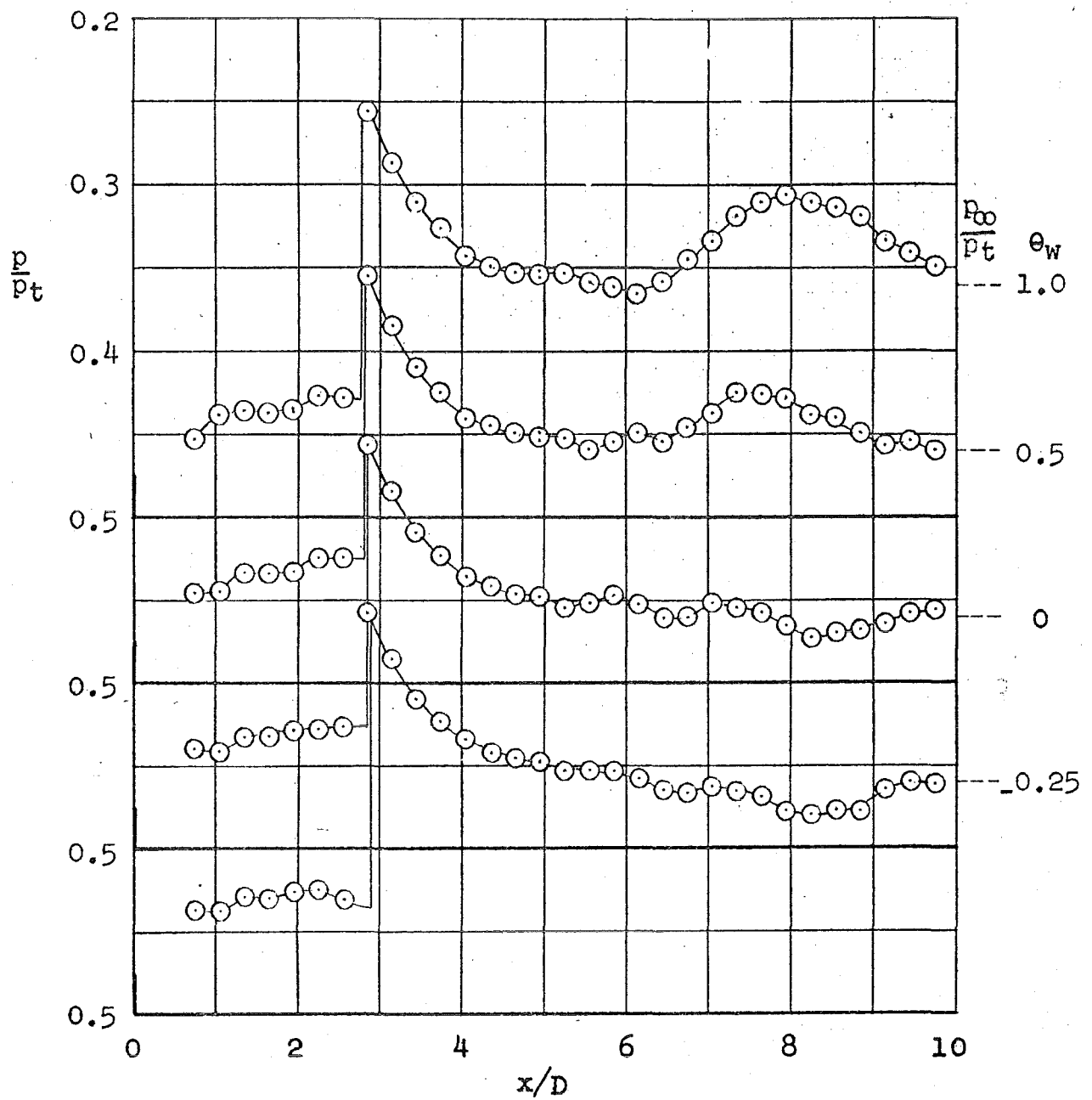
b. $\lambda = 1.25$, θ_w = Variable

Fig. 13 Concluded
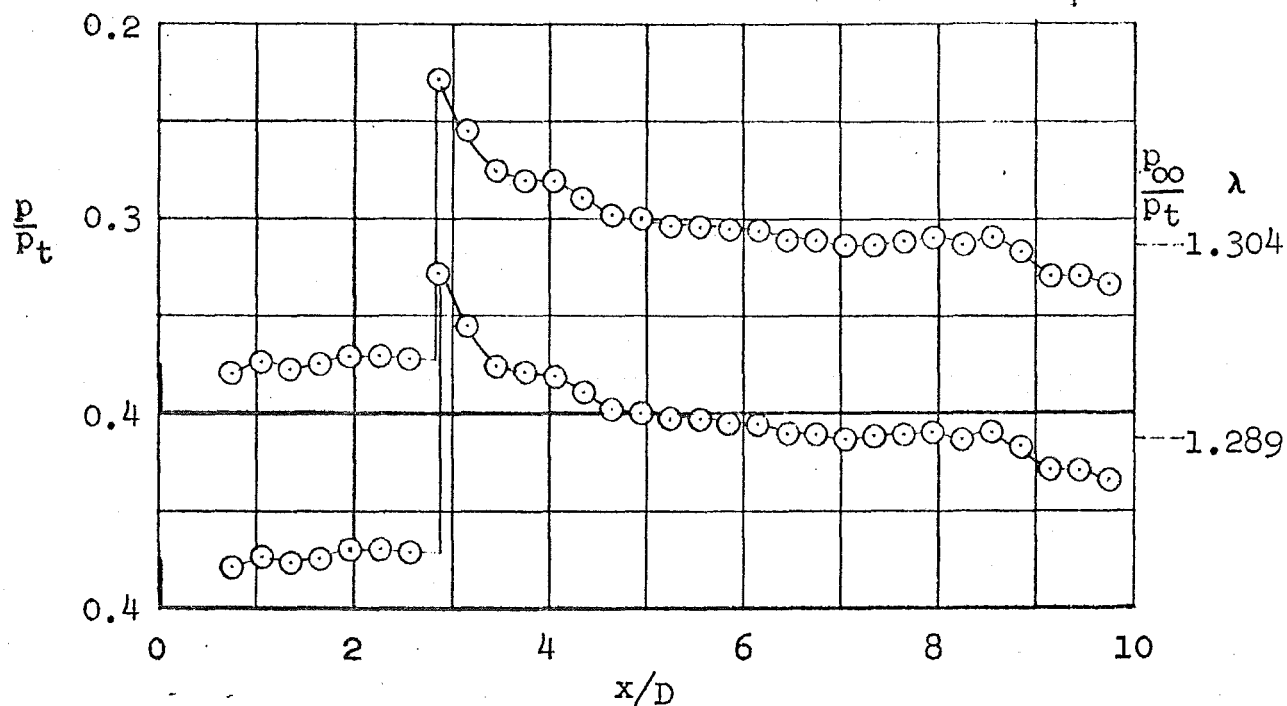
a. $\theta_w = 0$ deg, λ = Variable

Fig. 14 Pressure Distributions on 10.0-diam Cone-Cylinder
at $M_\infty = 1.40$

b. $\lambda = 1.33$, θ_w = Variable

Fig. 14 Concluded

a. $\theta_w = -0.25$ deg, λ = Variable

Fig. 15 Pressure Distributions on 10.0-diam Cone-Cylinder
at $M_\infty = 1.50$

b. $\theta_w = 0$ deg, λ = Variable
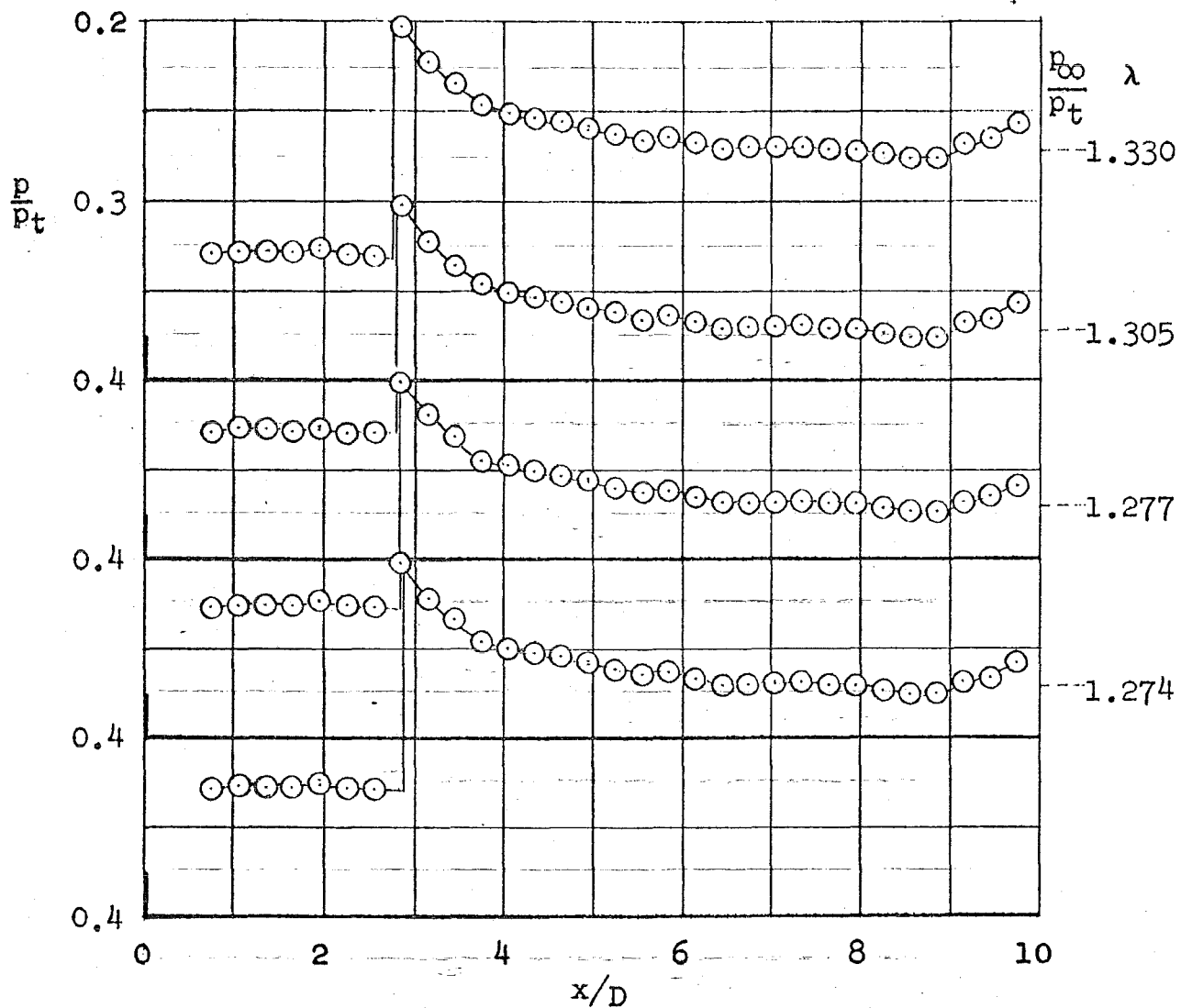
Fig. 15 Continued

c. $\theta_w = +0.5$ deg, $\lambda =$ Variable

Fig. 15 Continued

d. $\theta_w = +1.0$ deg, λ = Variable

Fig. 15 Continued
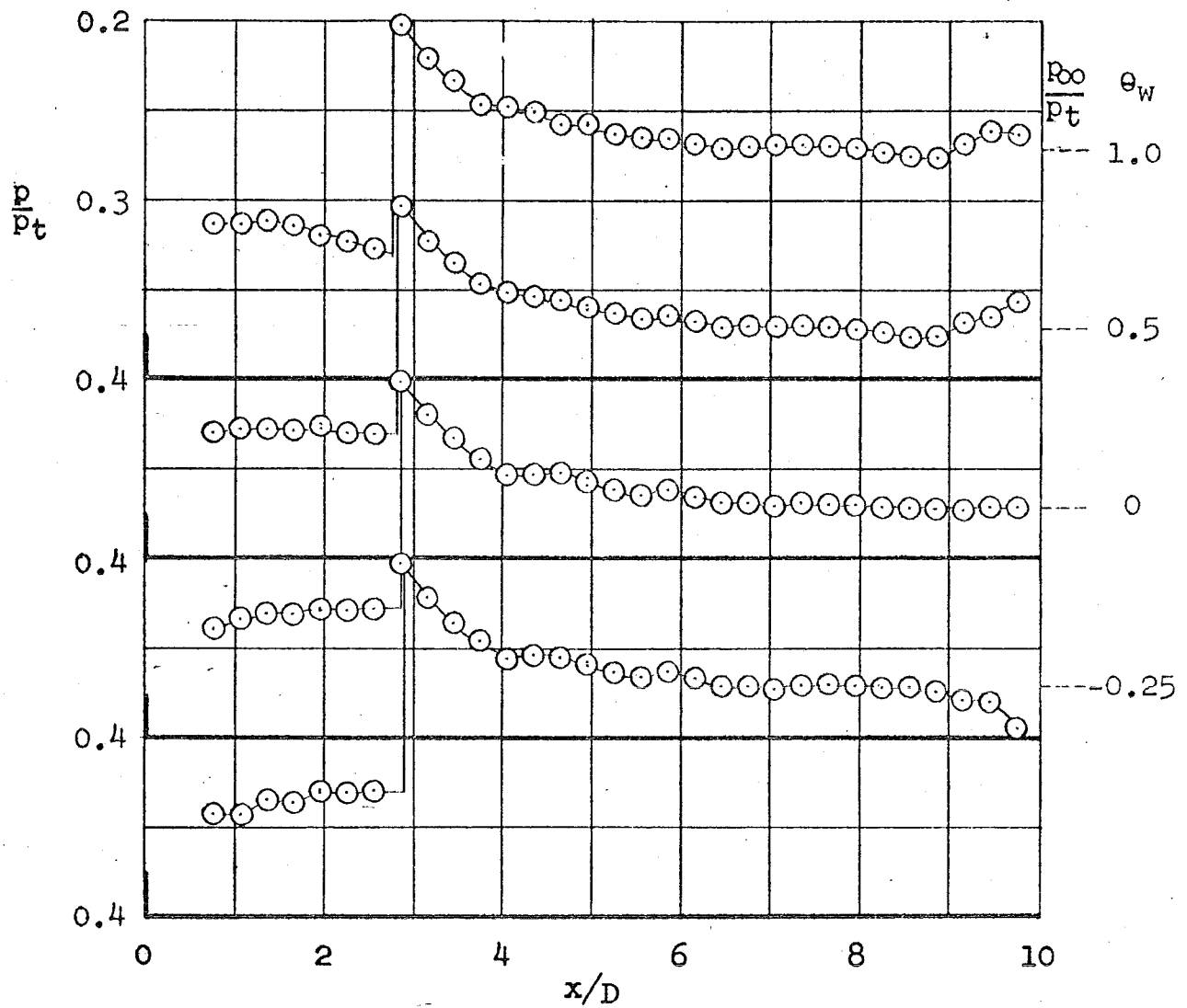
e. $\lambda_{(\theta_w = -0.25)} = 1.44$, $\lambda_{(\theta_w = 0 \text{ through } +1.0)} = 1.35$, θ_w = Variable

Fig. 15 Concluded

a. $\theta_w = +0.5$ deg, λ = Variable

Fig. 16 Pressure Distributions on 10.0-diam Cone-Cylinder
at $M_\infty = 1.60$
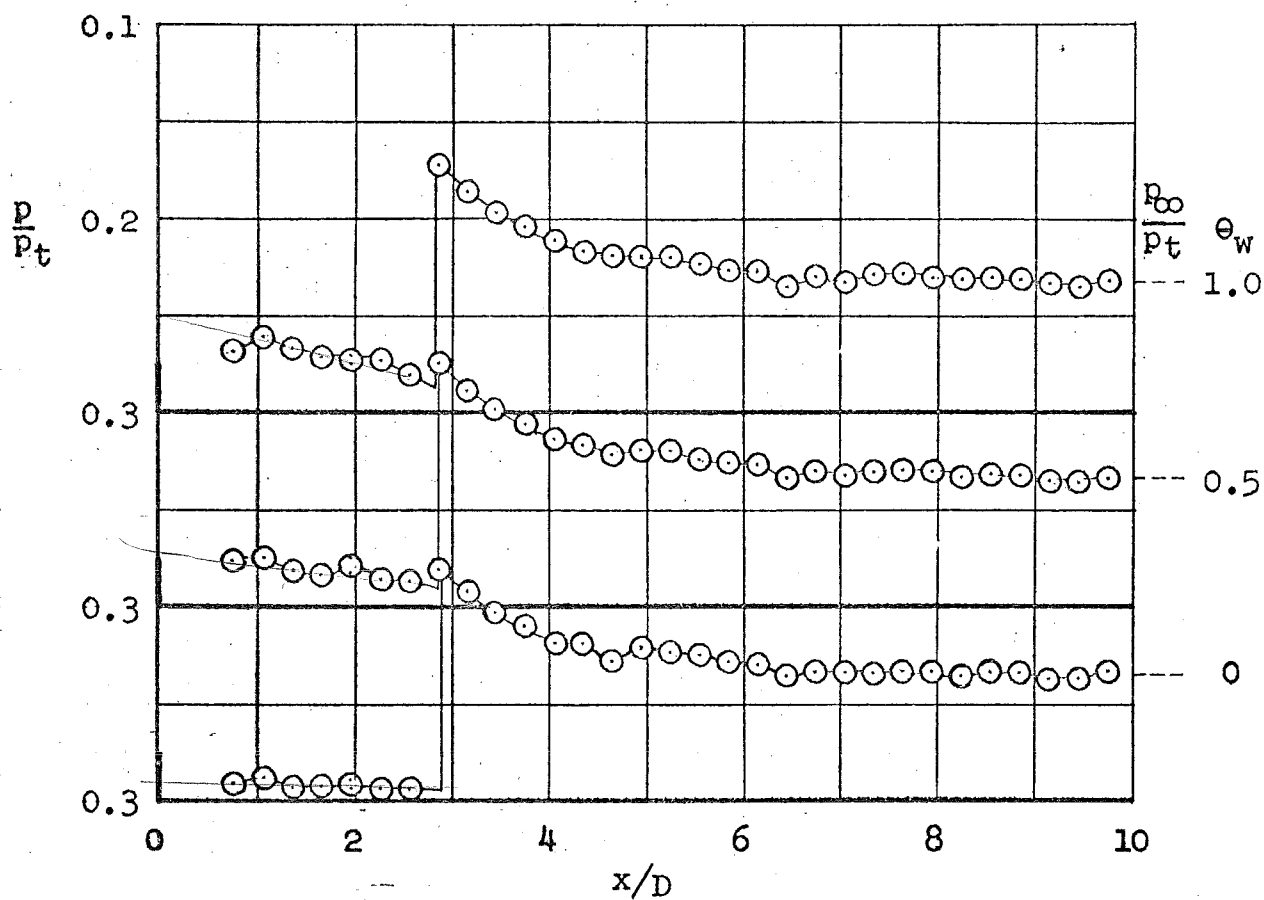
b. $\lambda = 1.48$, θ_w = Variable

Fig. 16 Concluded
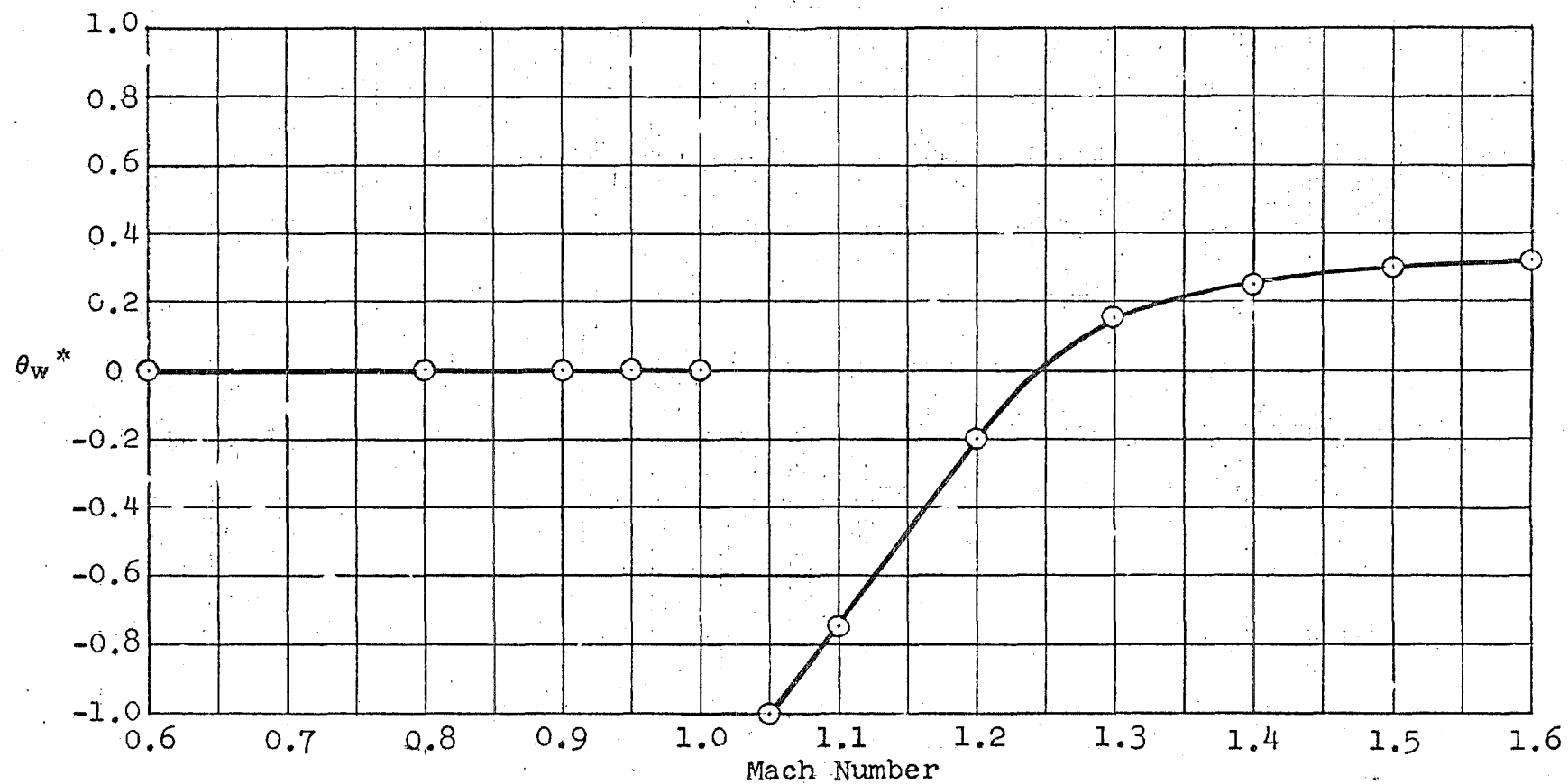
Fig. 17 Variation of Optimum Test Section Wall Angle, θ_w^*, with Mach Number

10.0 D Cone-Cylinder		8.5 D Cone-Cylinder	
Symbol	Θ_W, deg	Symbol	Θ_W, deg
○	-0.50	▨	0
□	0		
◇	0.50		
△	1.00		
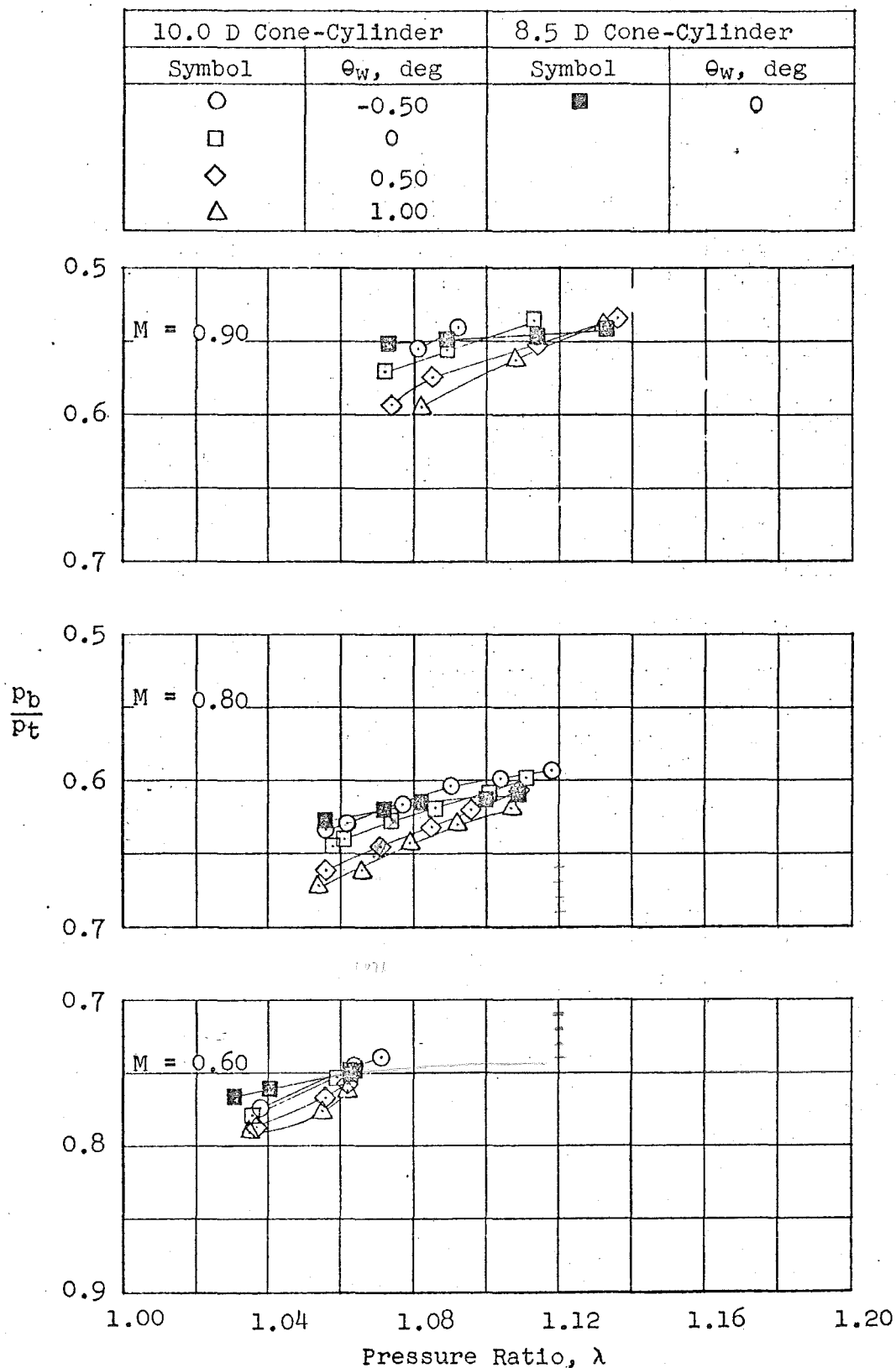
Fig. 18 Base Pressure Data for 8.5-diam and 10.0-diam Cone-Cylinder Models as a Function of Test Leg Pressure Ratio, λ, for a Series of Mach Numbers

10.0 D Cone-Cylinder		8.5 D Cone-Cylinder	
Symbol	Θ_W, deg	Symbol	Θ_W, deg
$\bigcirc$	-0.50	◀	-0.75
$\square$	0	▨	0
$\diamondsuit$	0.50		
$\triangle$	1.00		
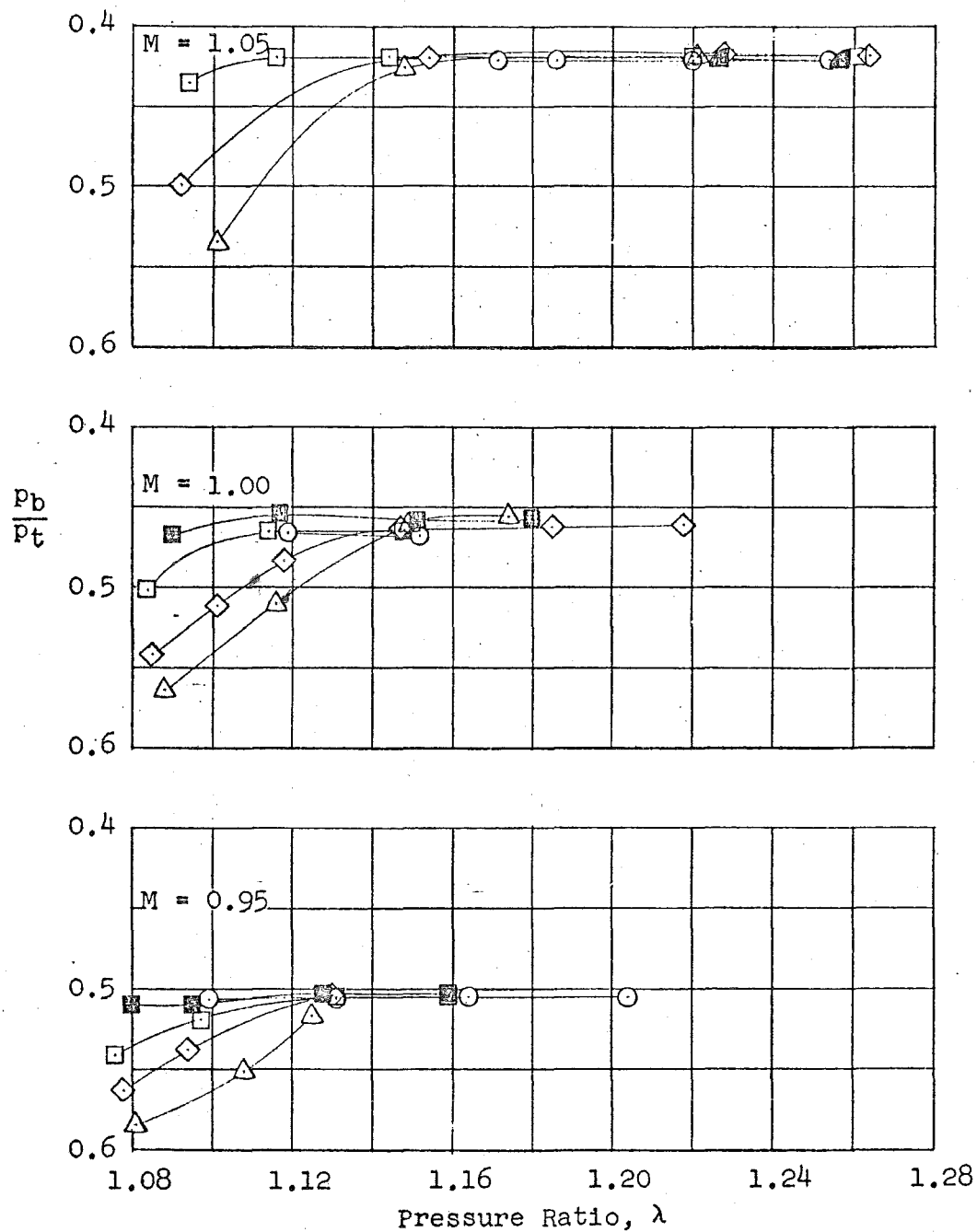
Fig. 18 Continued

10.0 D Cone-Cylinder		8.5 D Cone-Cylinder	
Symbol	Θ_W, deg	Symbol	Θ_W, deg
○	-0.50	◢	-0.75
⌂	-0.25	◓	-0.25
□	0	◭	-0.10
◇	0.50		
△	1.00		

Note Change in Scale
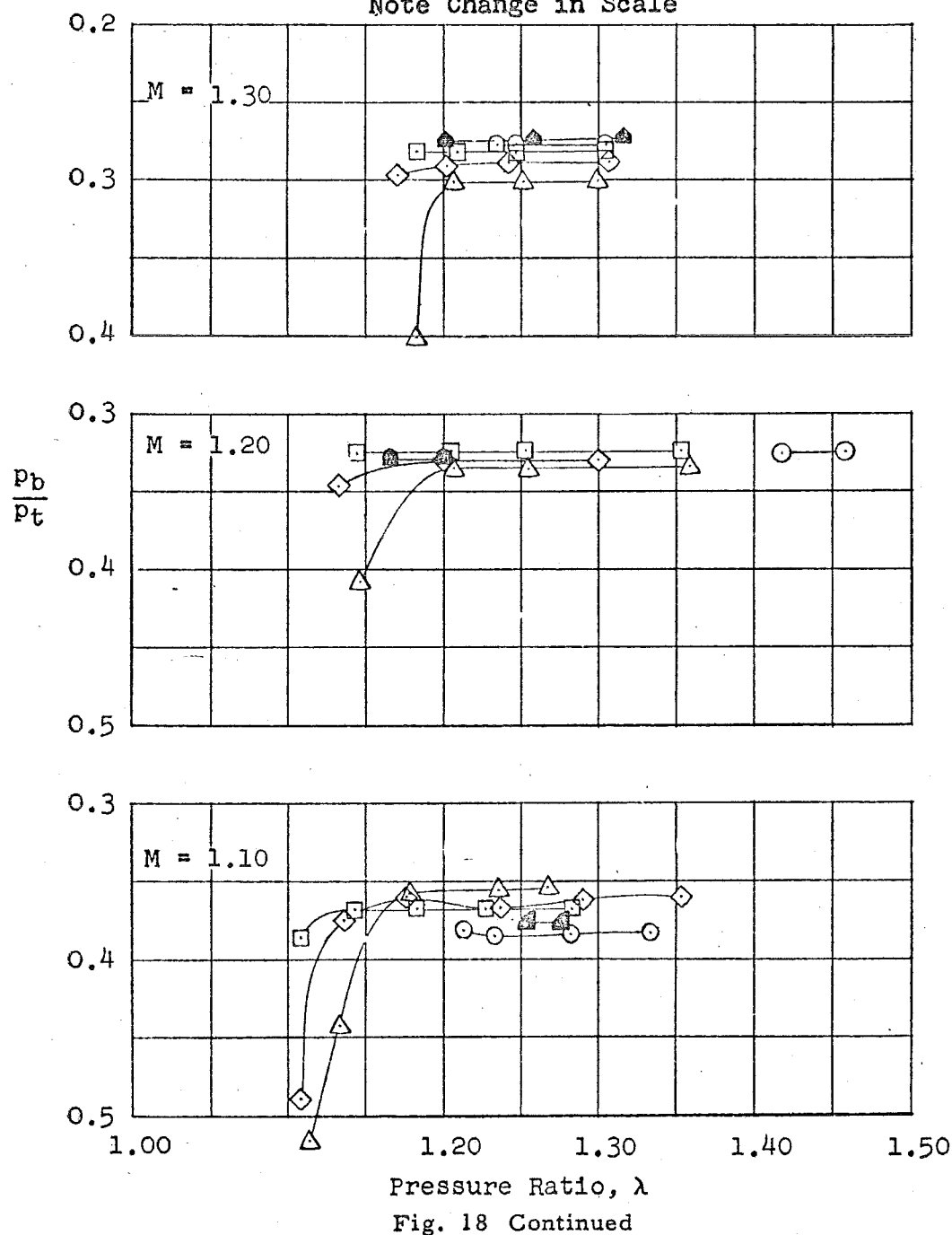
$\dfrac{p_b}{p_t}$

Pressure Ratio, λ

Fig. 18 Continued

10.0D Cone-cylinder		8.5D Cone-cylinder	
Symbol	Θ_W	Symbol	Θ_W
⌂	-0.25	▽	0.10
□	0	▼	0.30
◇	0.50		
△	1.00		

M = 1.6

M = 1.5

$\frac{p_b}{p_t}$

opt Θ_w 0

M = 1.4
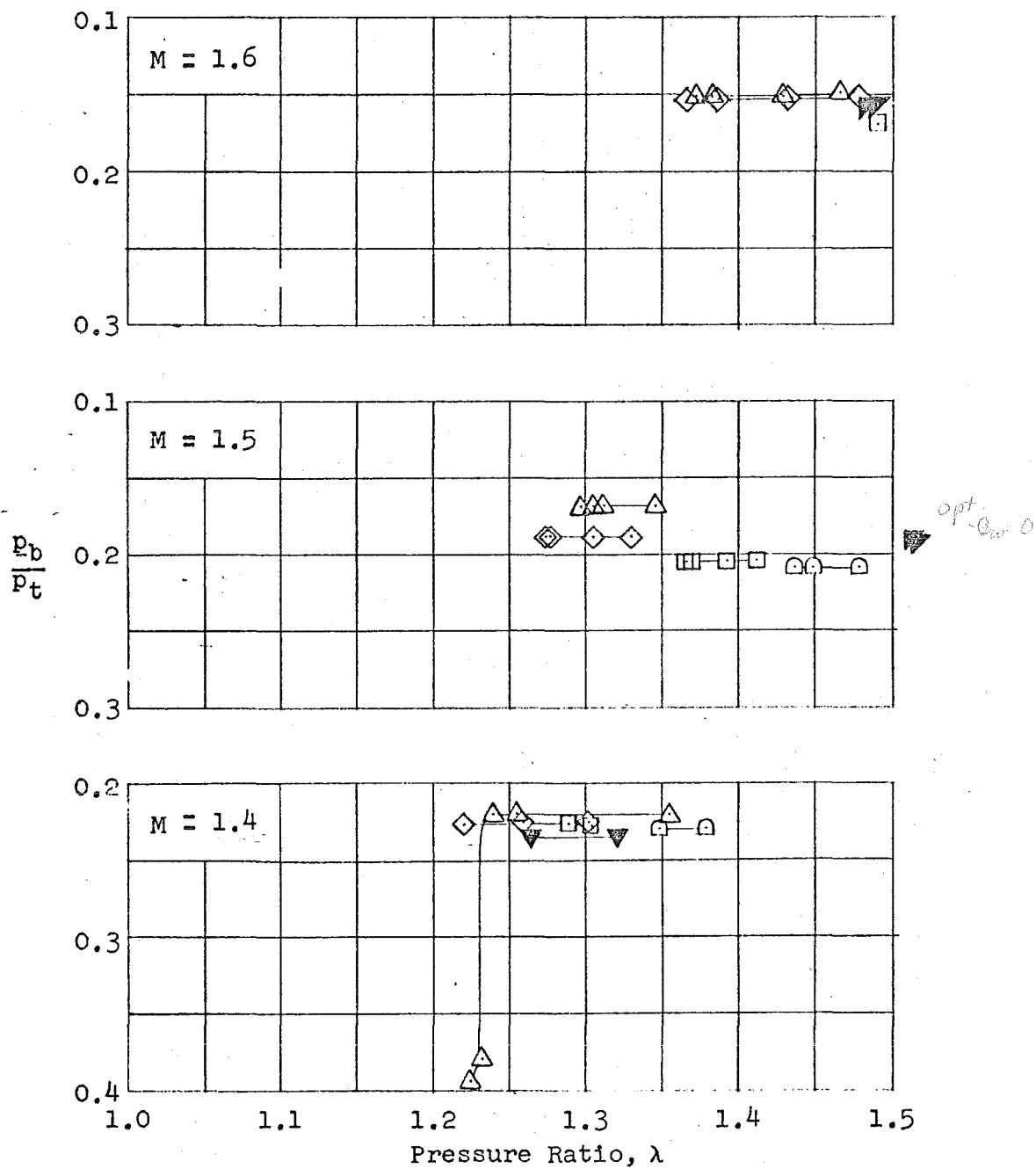
Pressure Ratio, λ

Fig. 18 Concluded
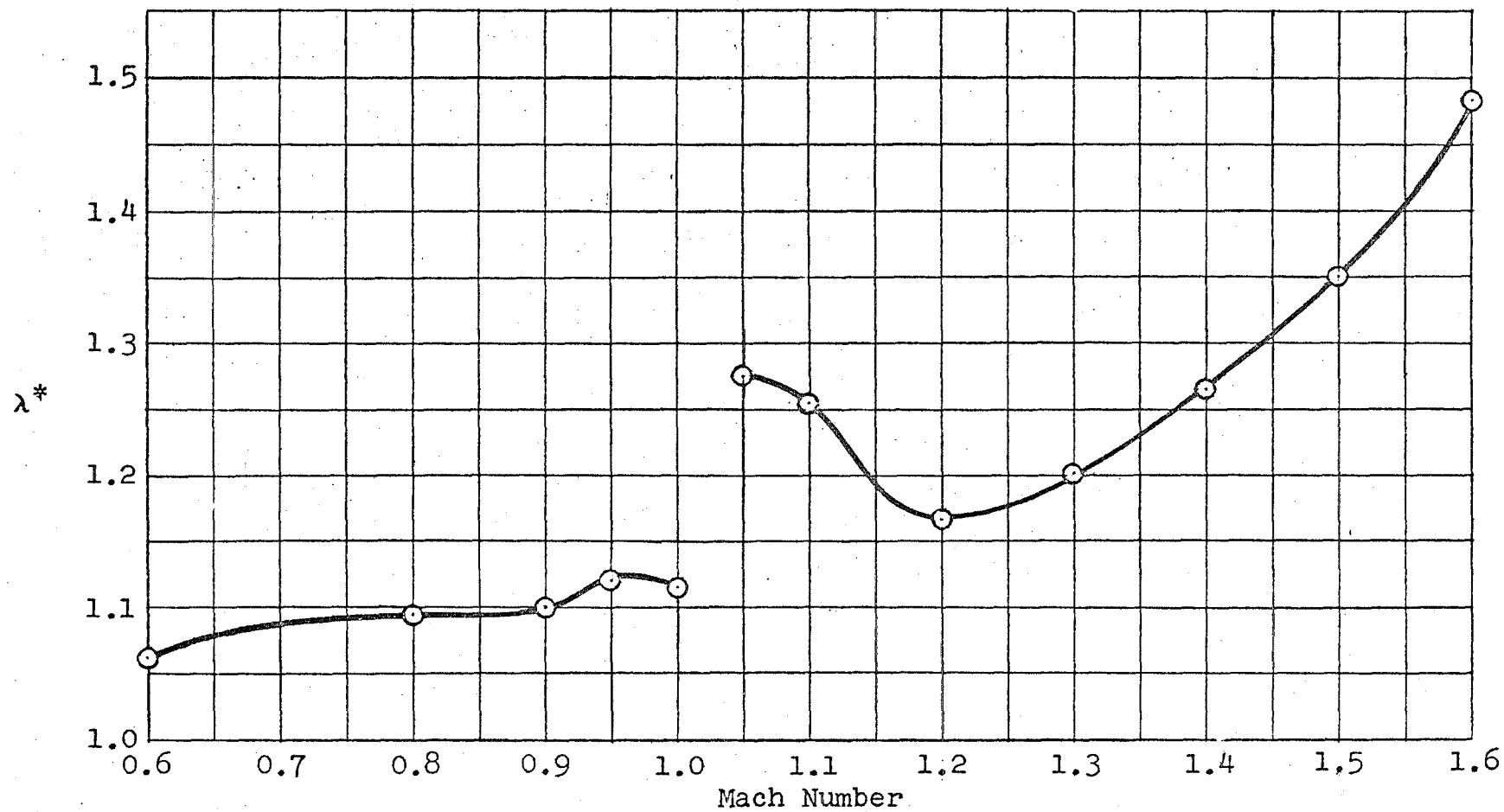
Fig. 19 Variation of Optimum Test Leg Pressure Ratio, λ^*, with Mach Number
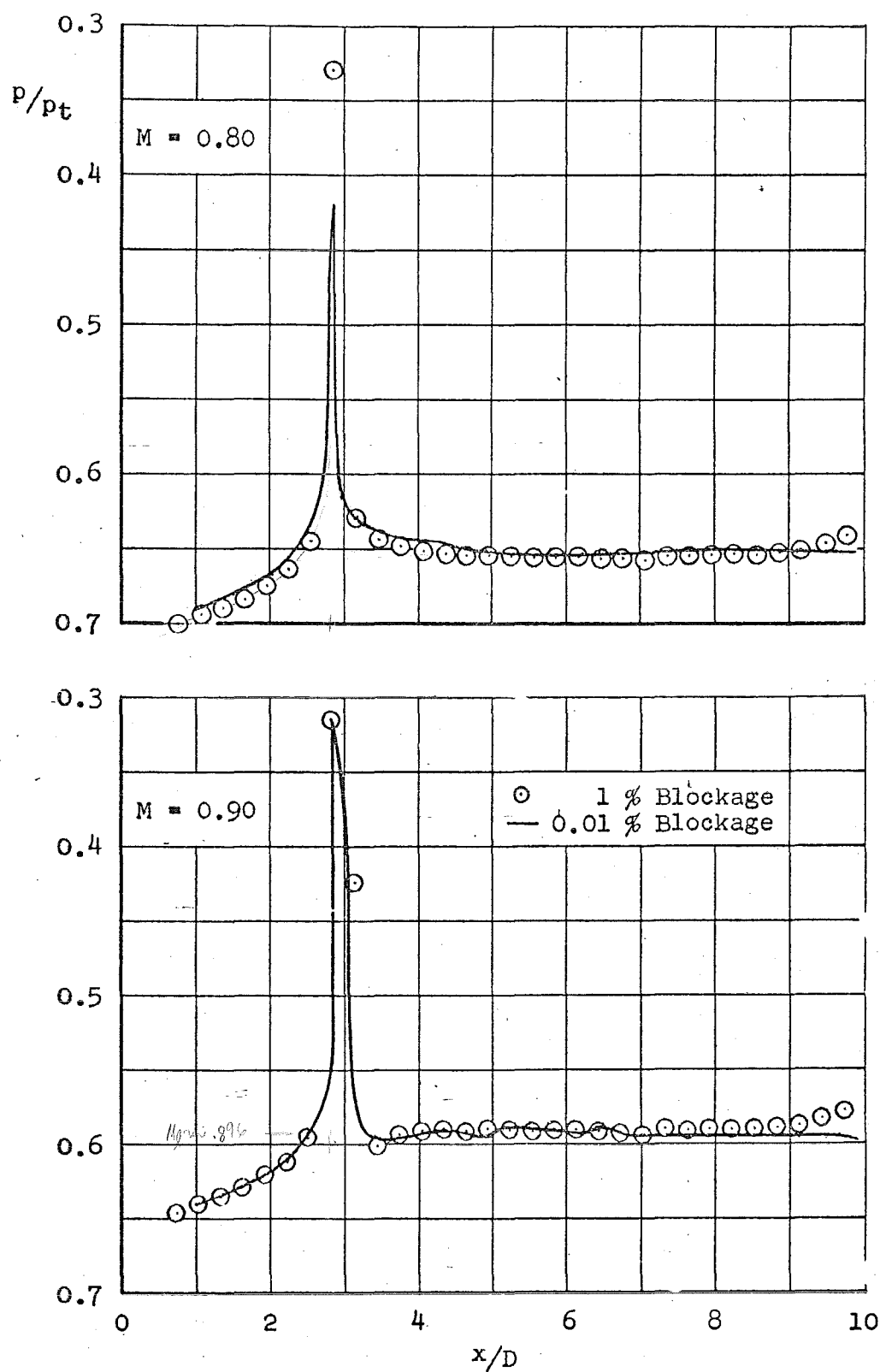
Fig. 20 Comparison of Pressure Distributions on 1-Percent
and 0.01-Percent Blockage 10.0-diam Cone-Cylinder
Models for a Series of Mach Numbers
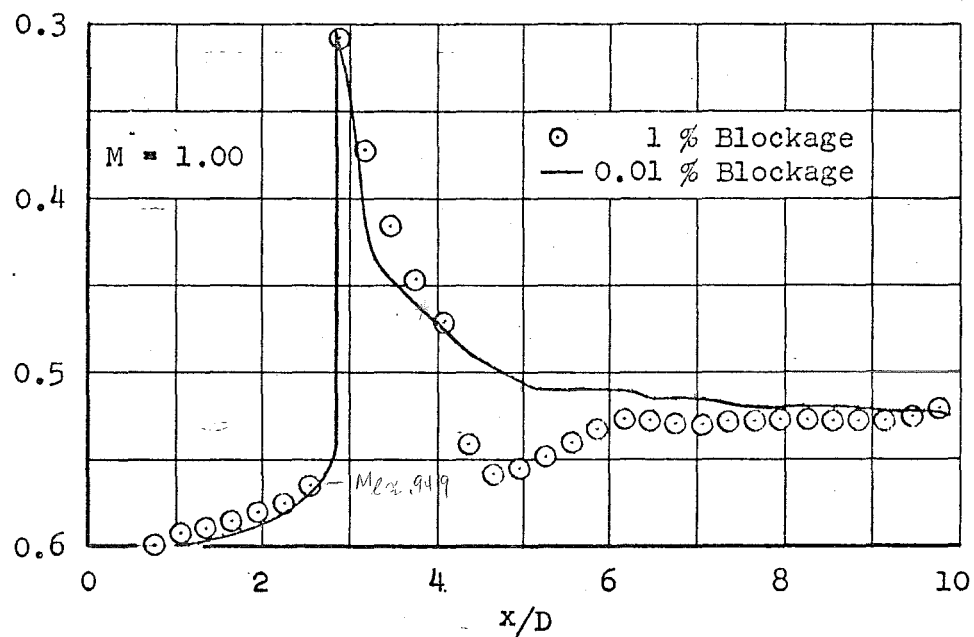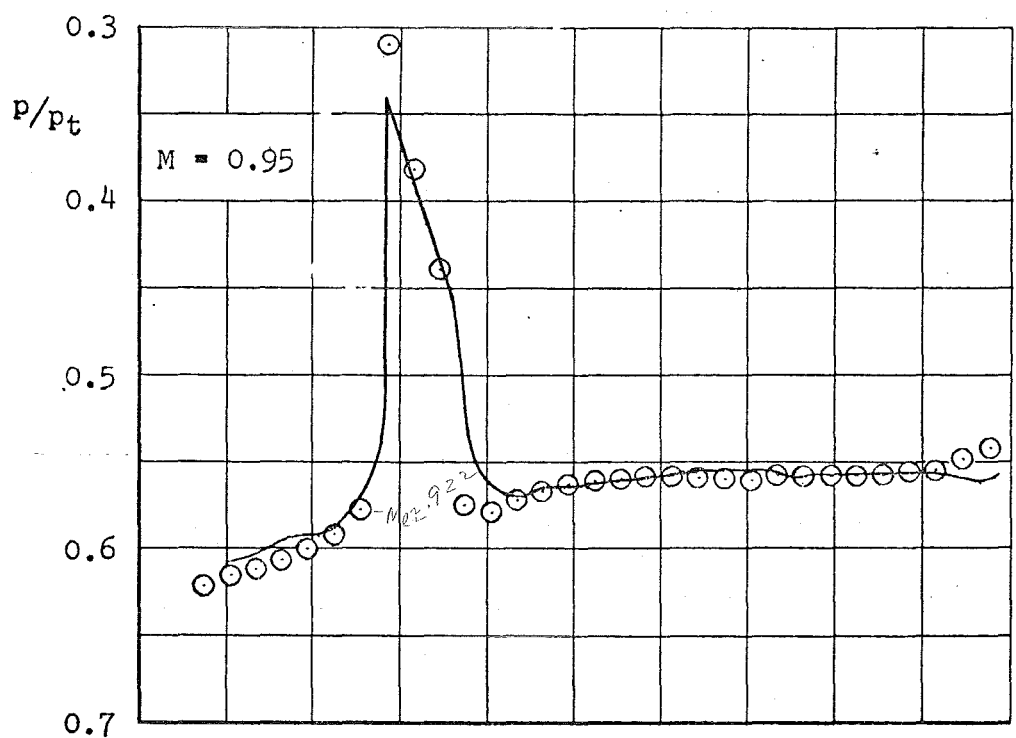
Fig. 20 Continued
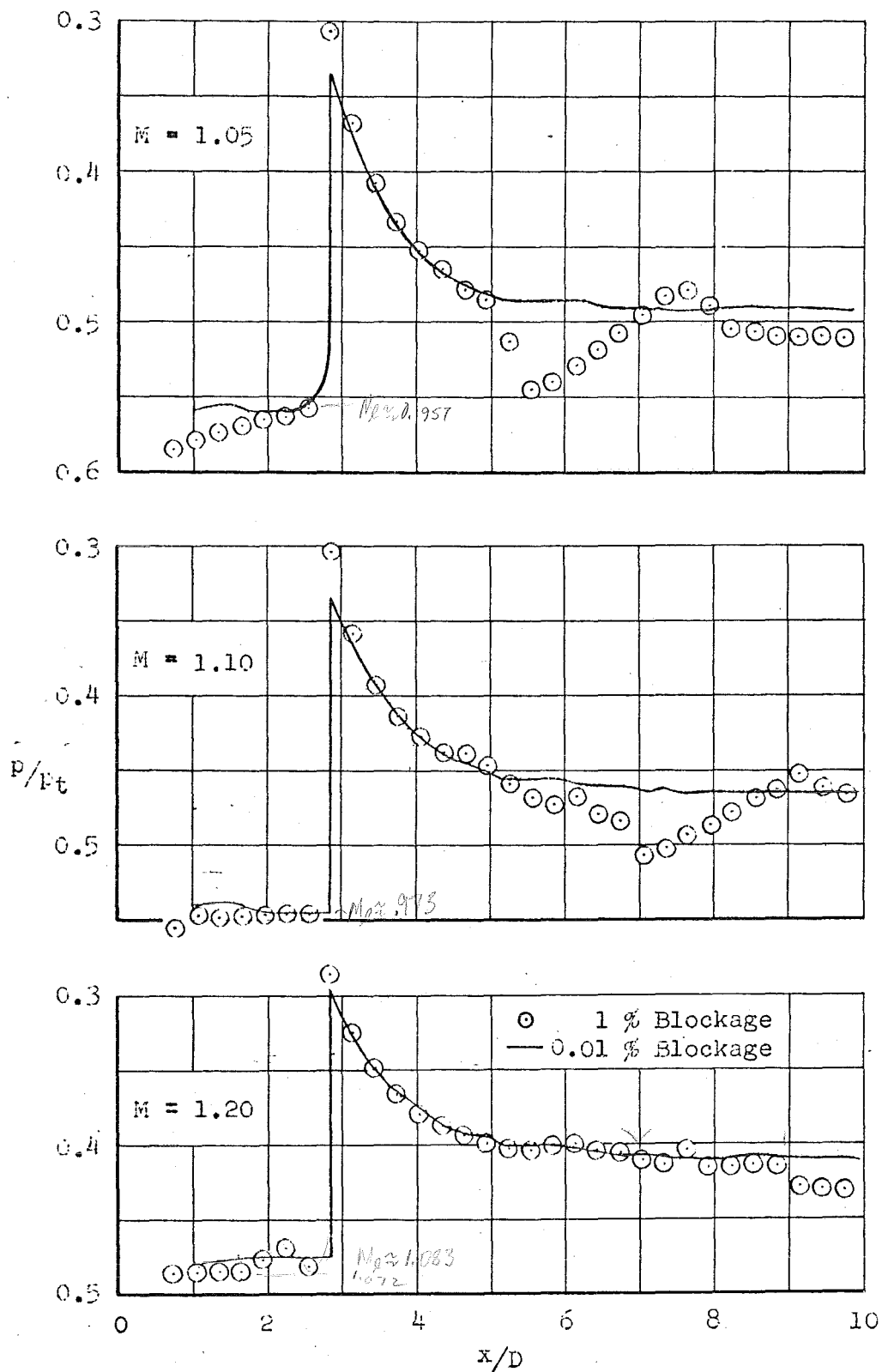
Fig. 20 Continued
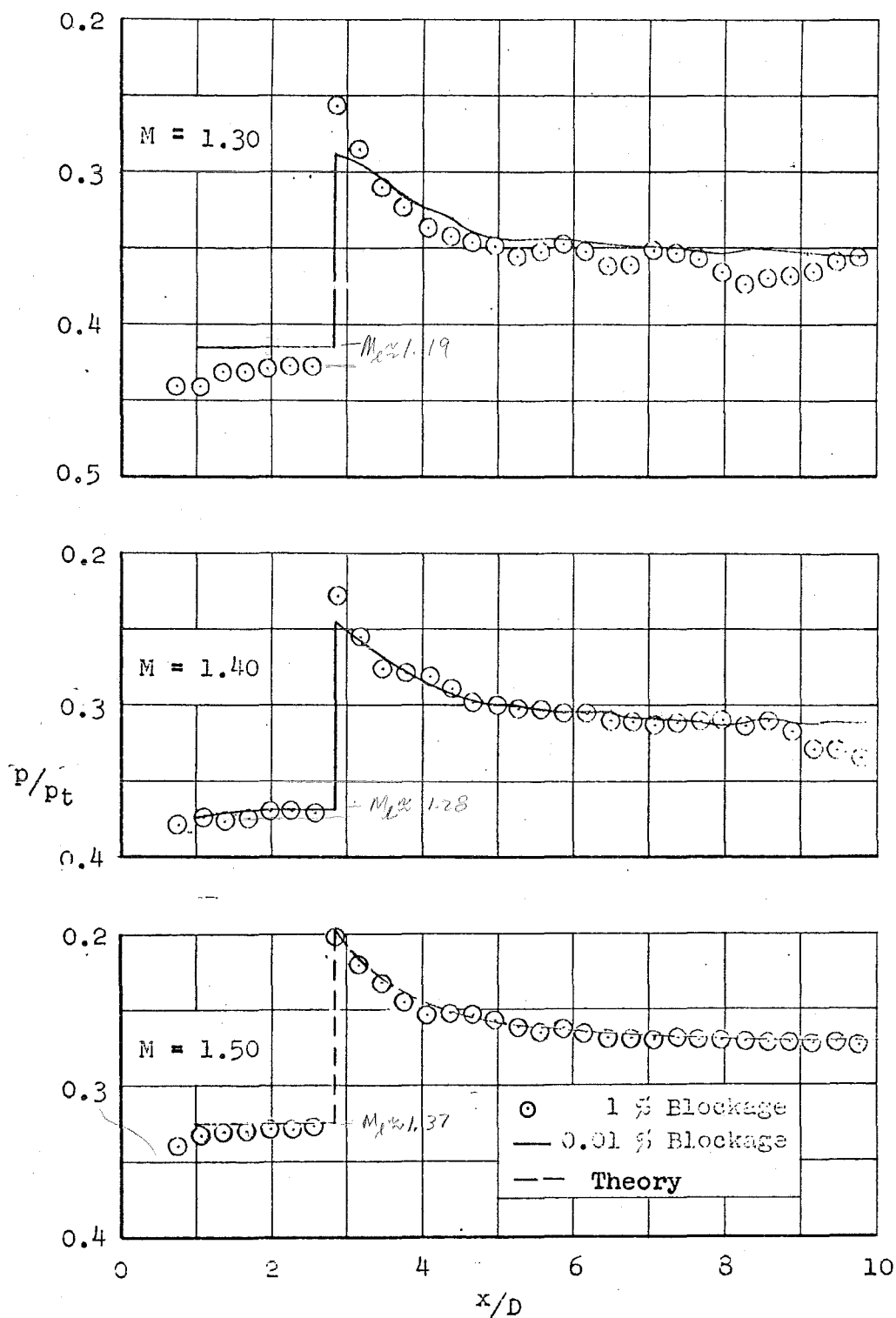
Fig. 20 Concluded
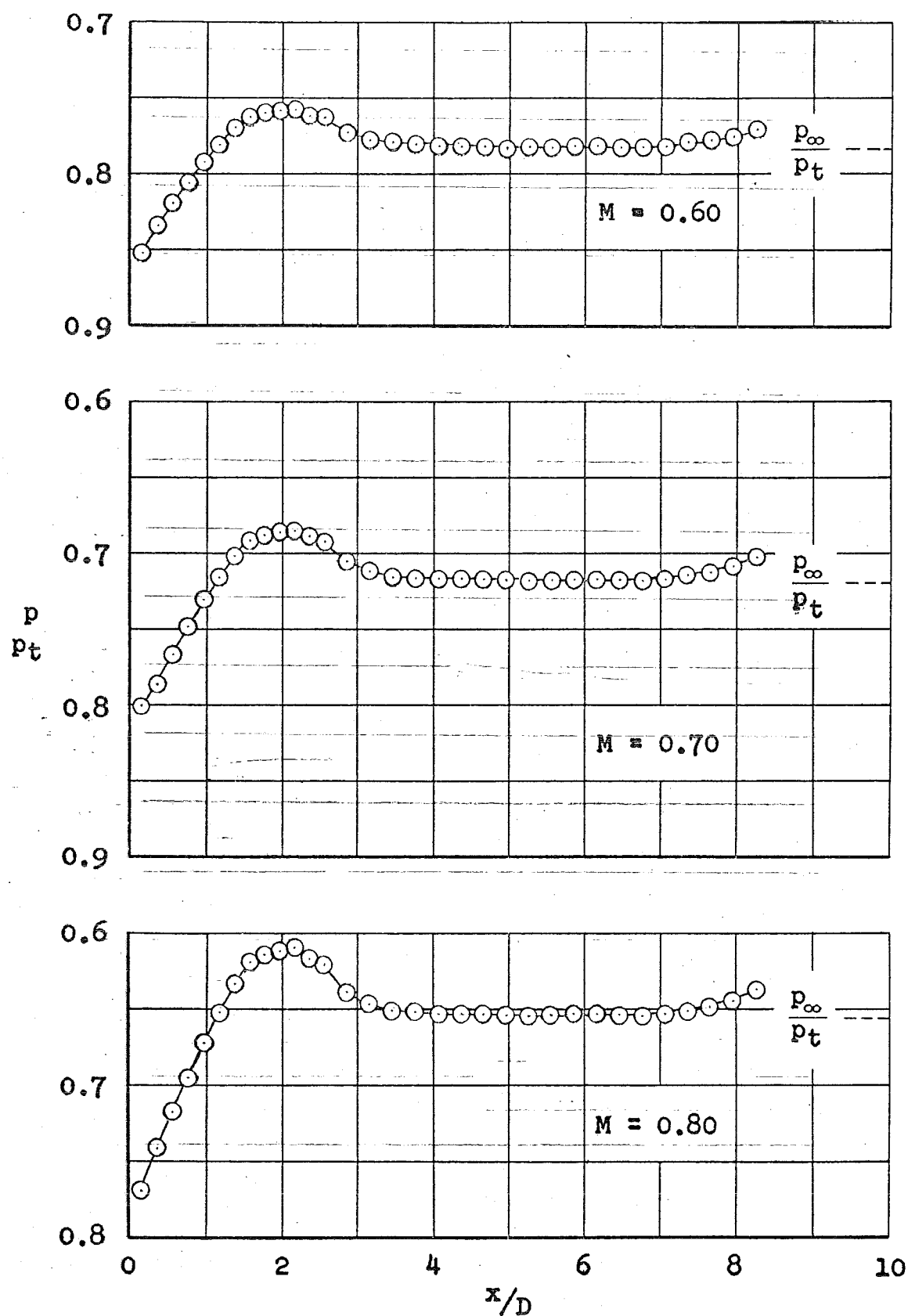
Fig. 21 Pressure Distributions on 8.5-diam Ogive-Cylinder
for a Series of Mach Numbers
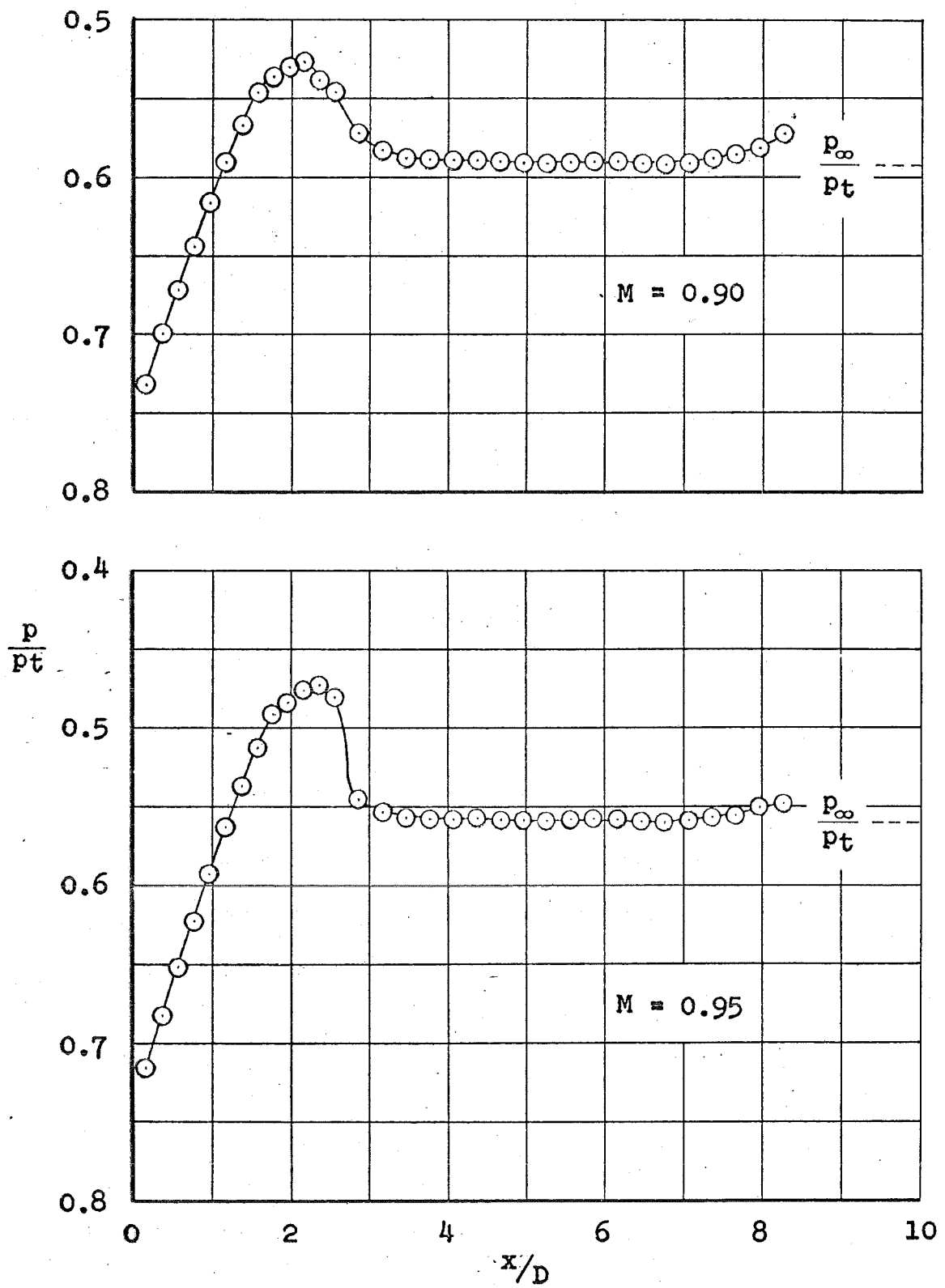
Fig. 21 Continued
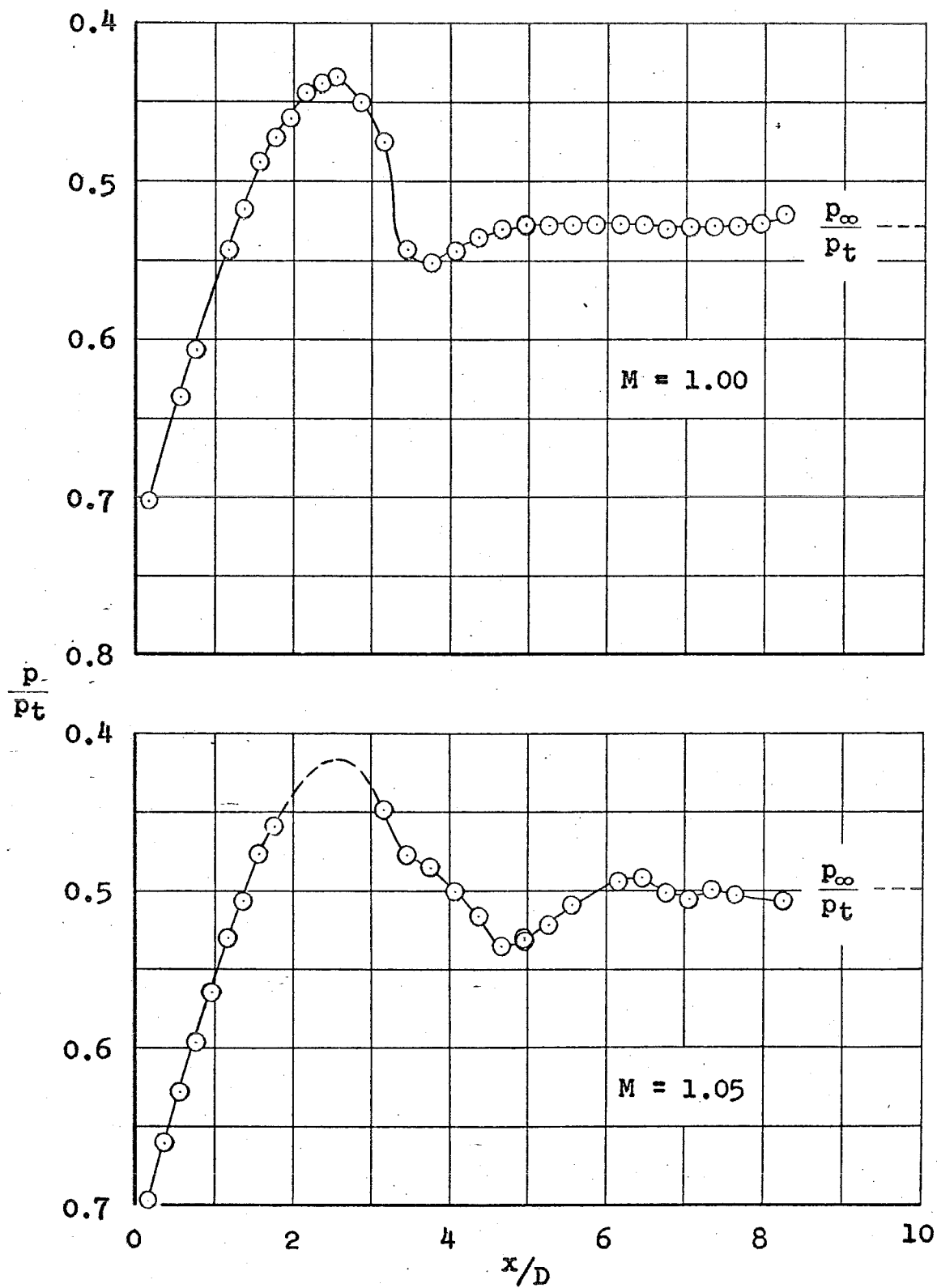
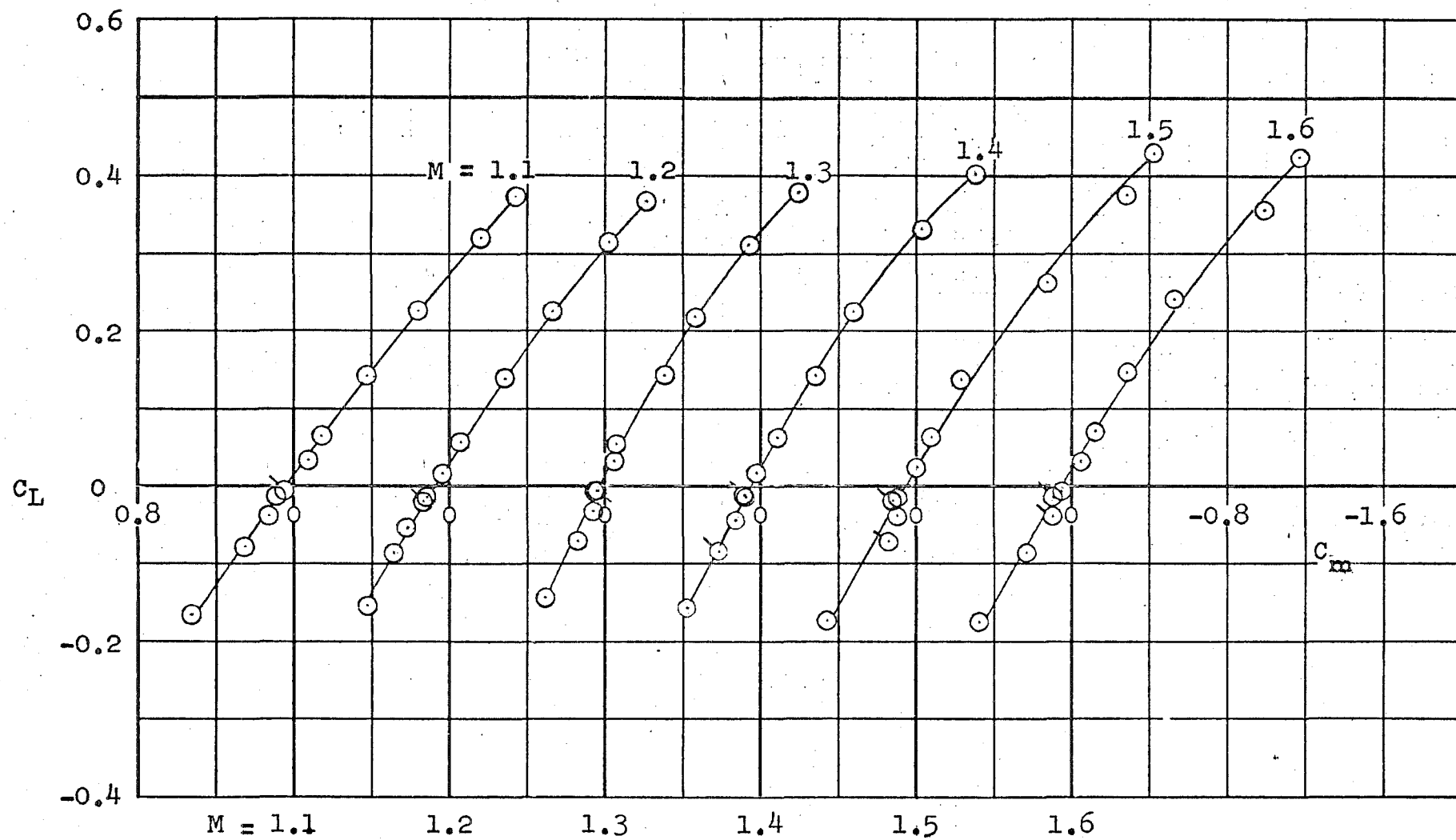Fig. 21 Continued
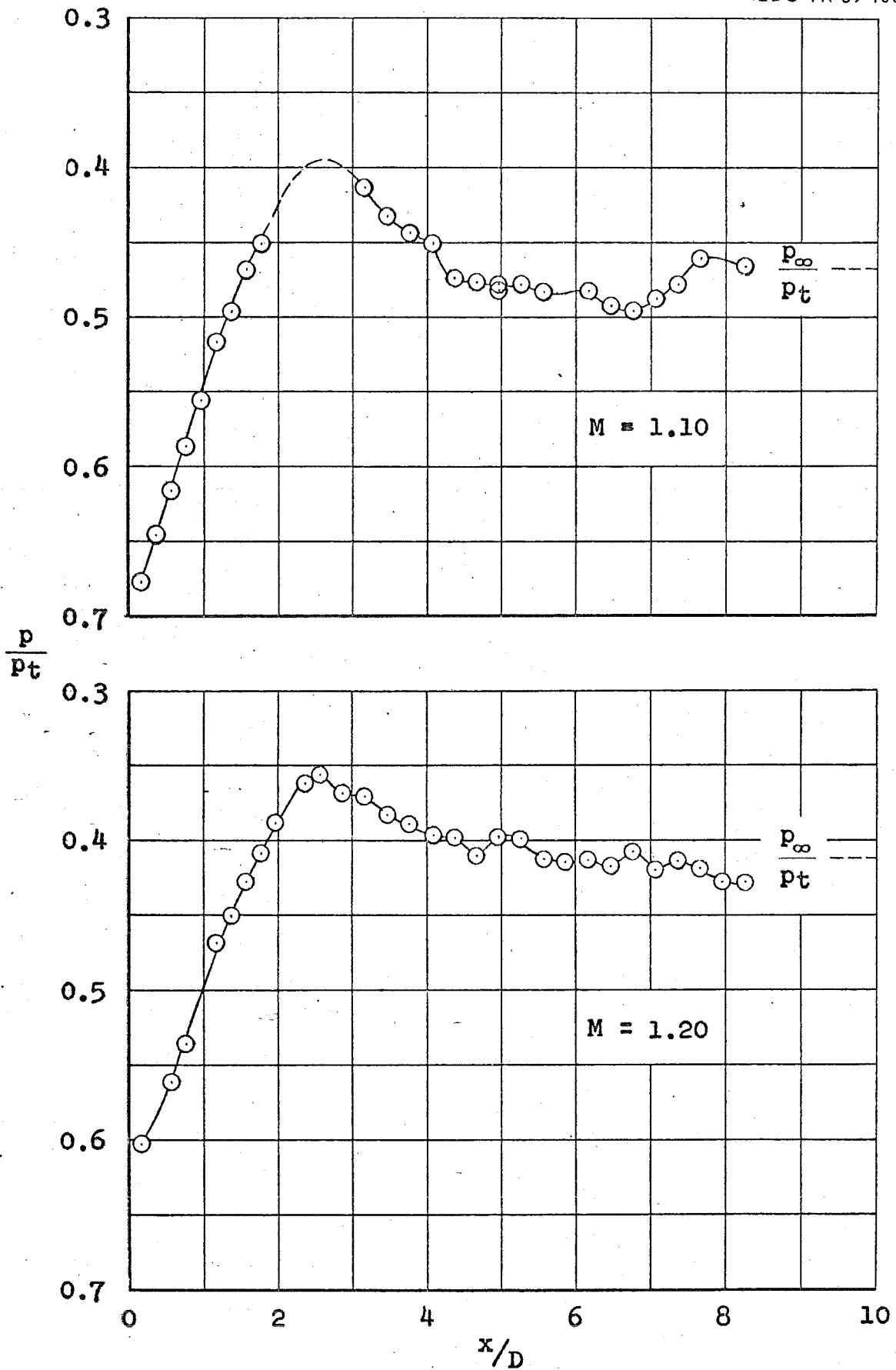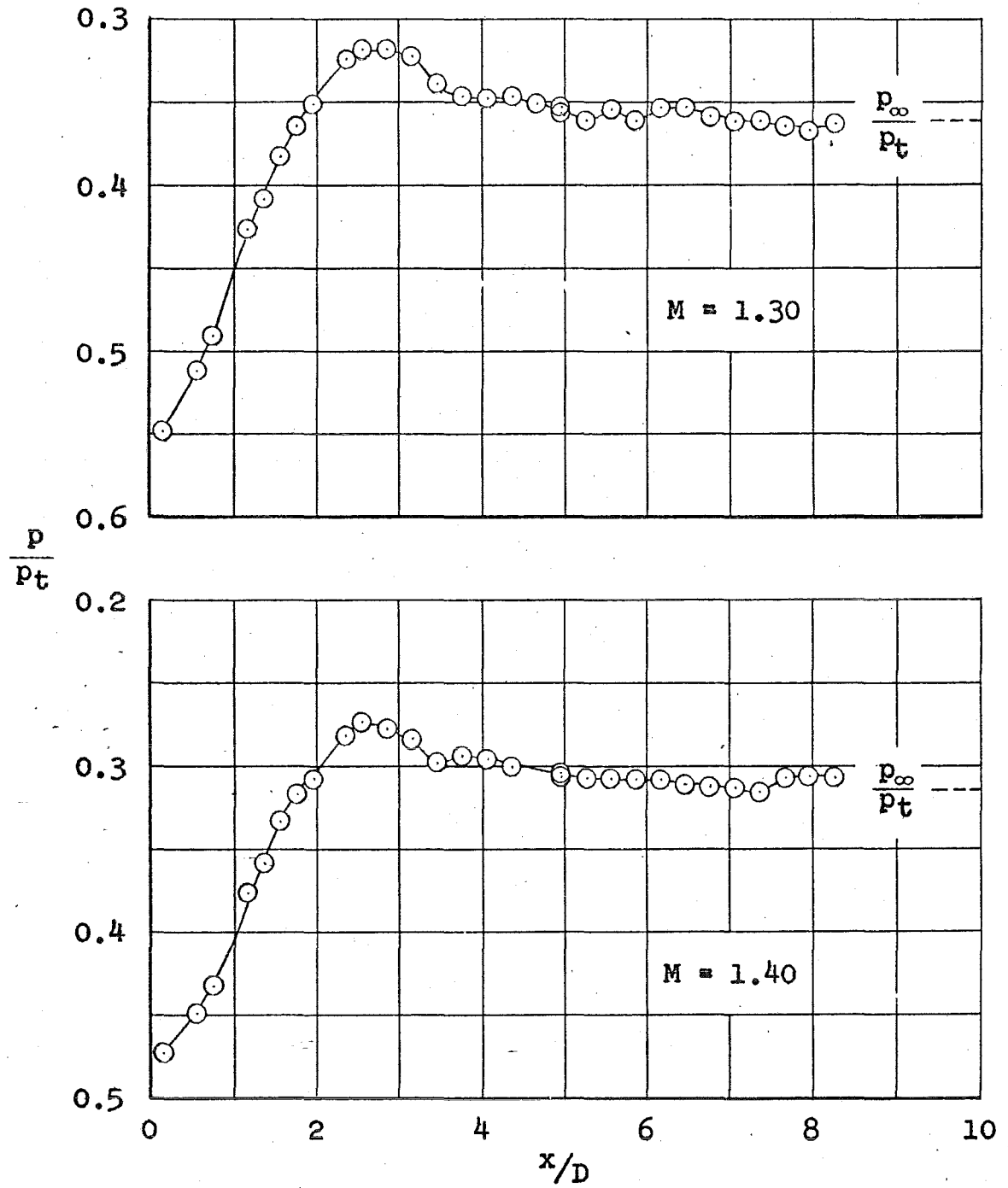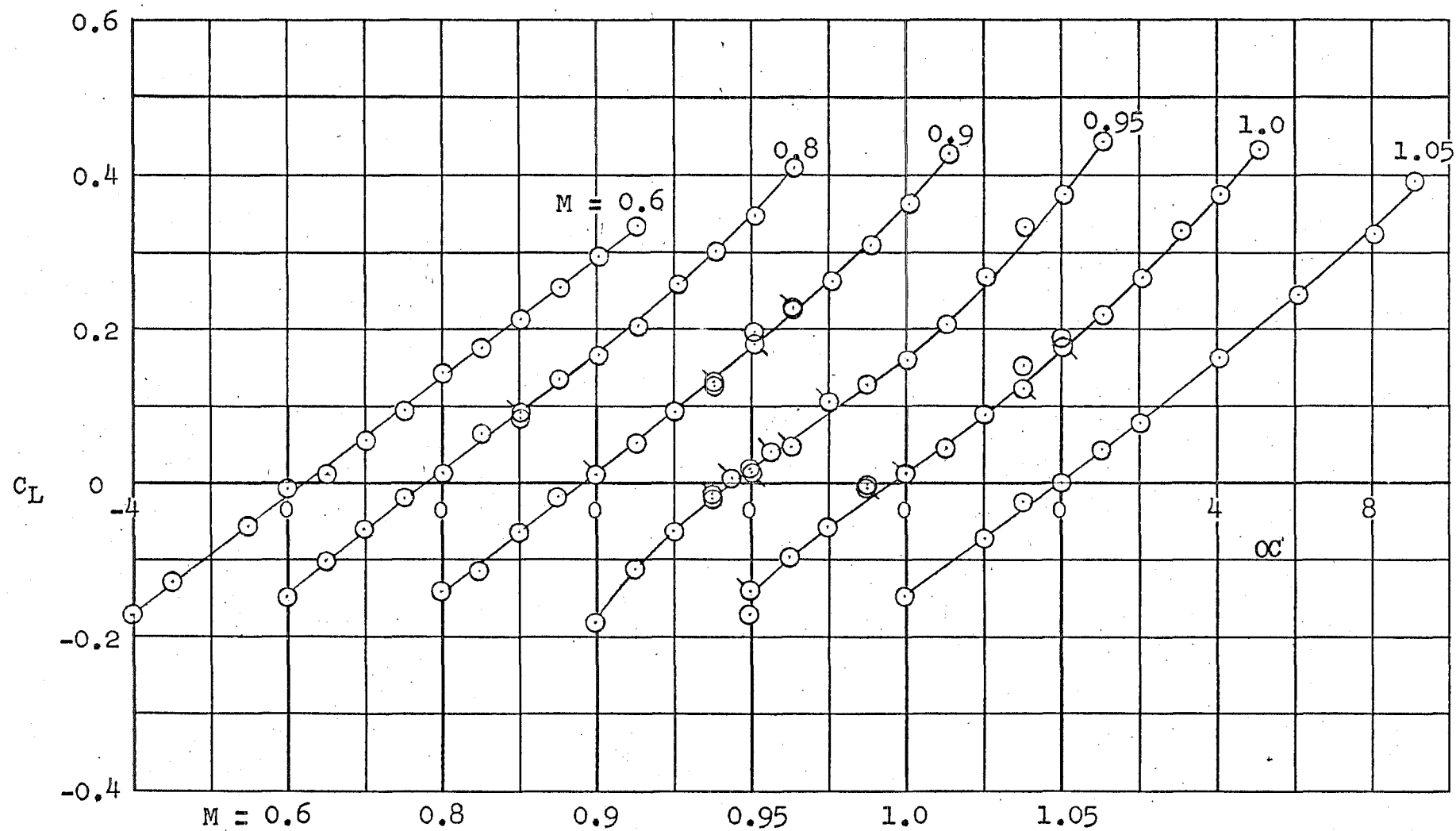
Fig. 21 Continued

Fig. 21 Continued
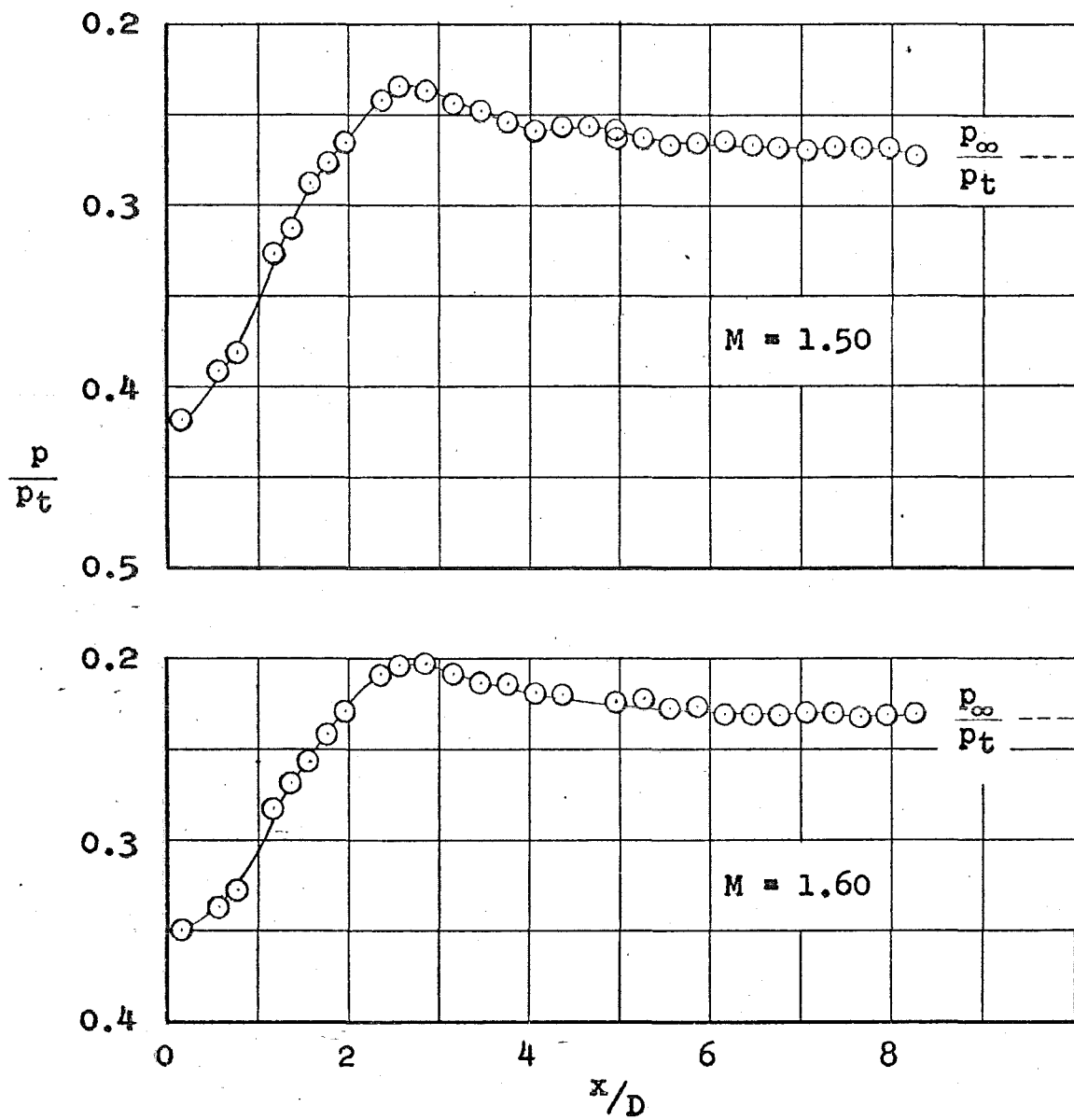
Fig. 21 Concluded
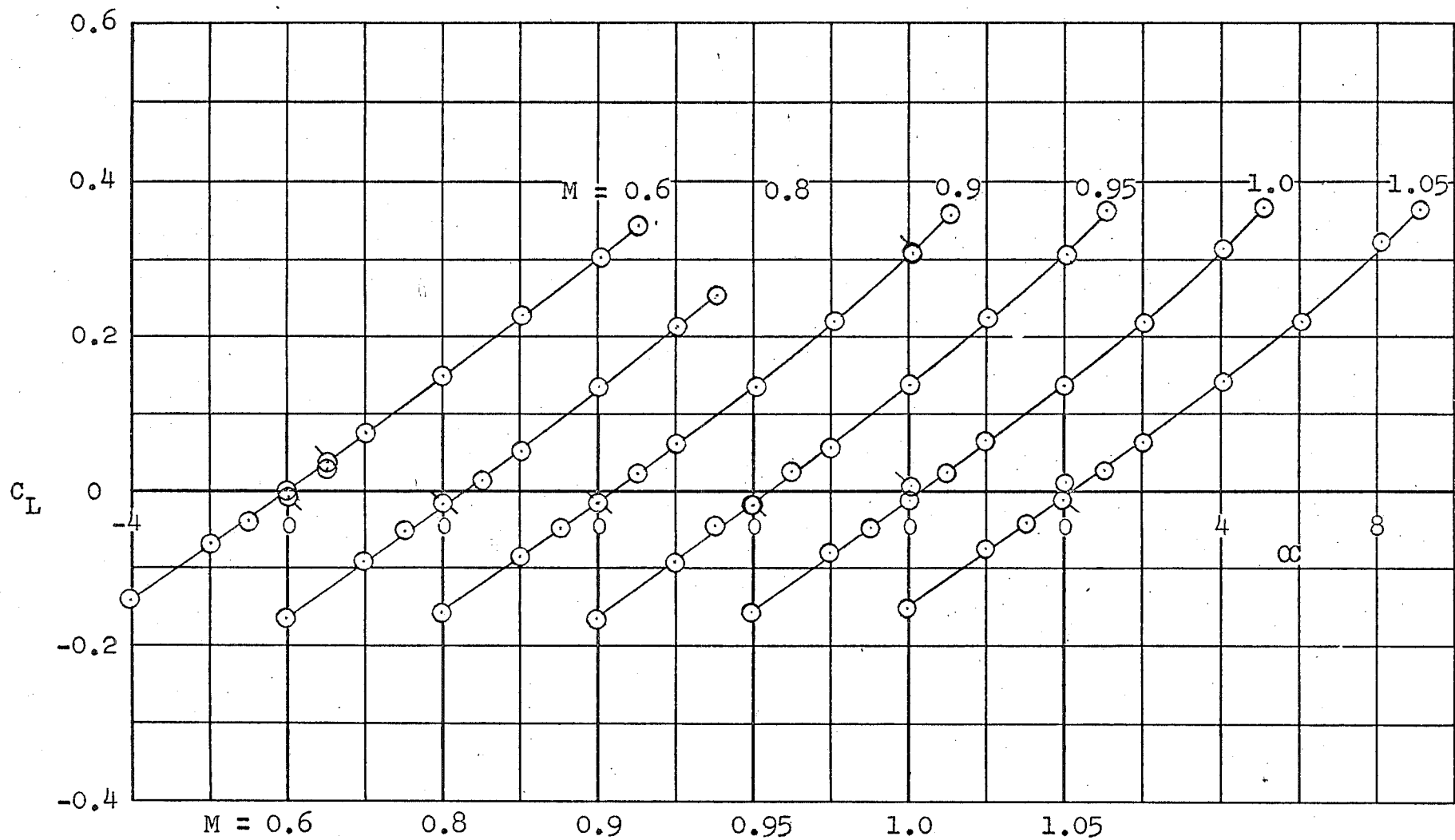
Fig. 22 Variation of Lift Coefficient with Angle of Attack for 8.5-diam
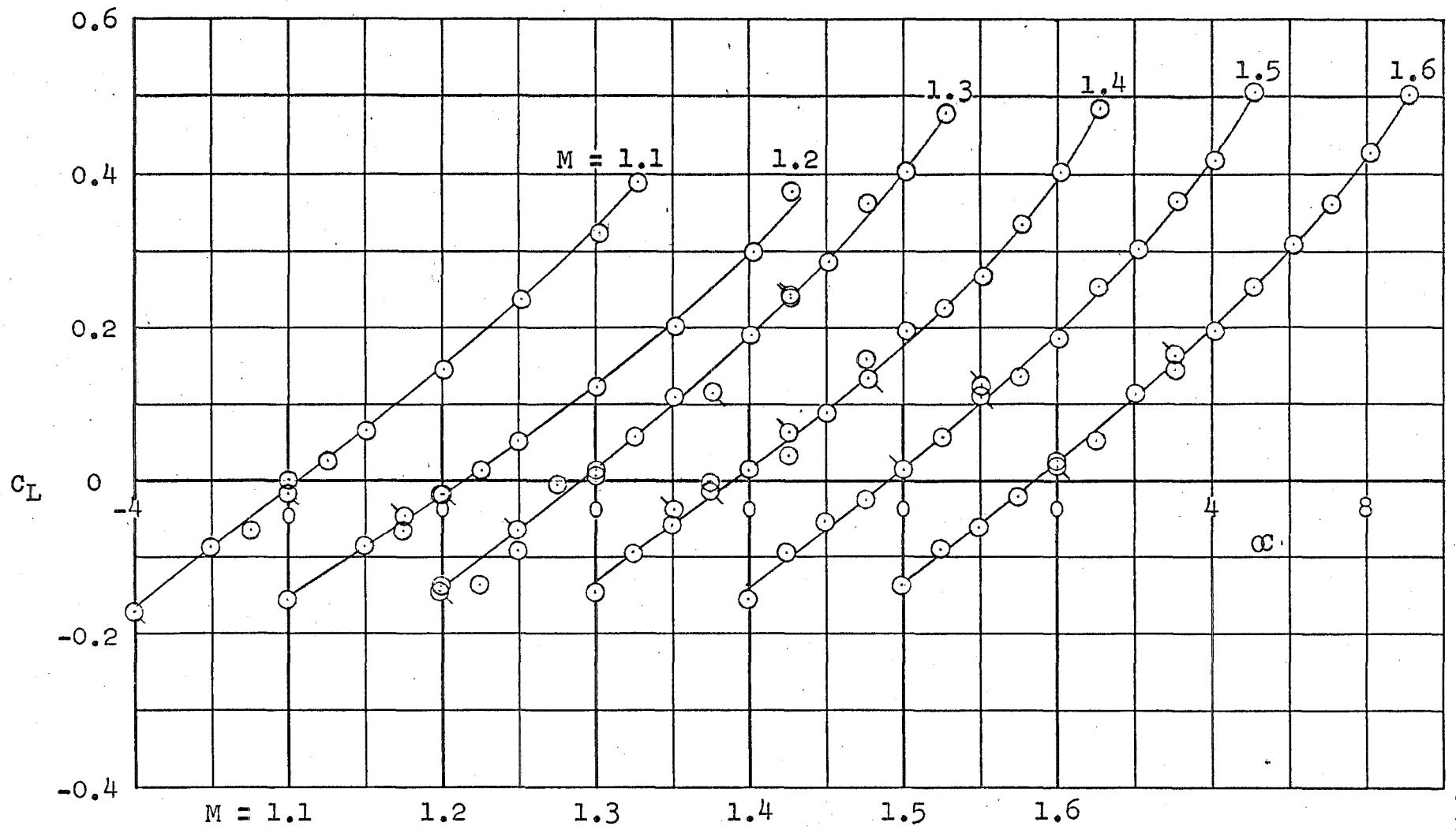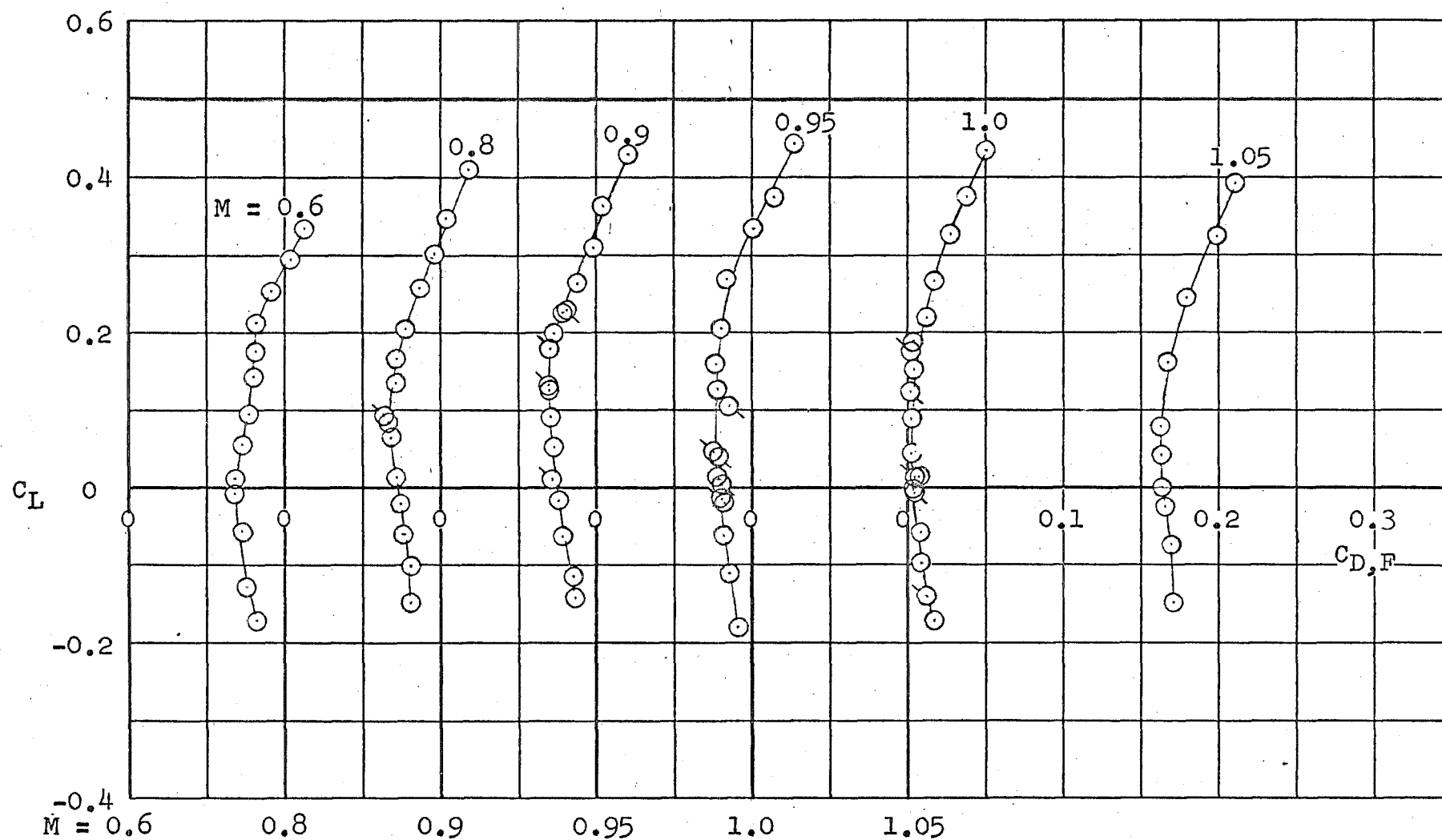Cone-Cylinder Model for a Series of Mach Numbers
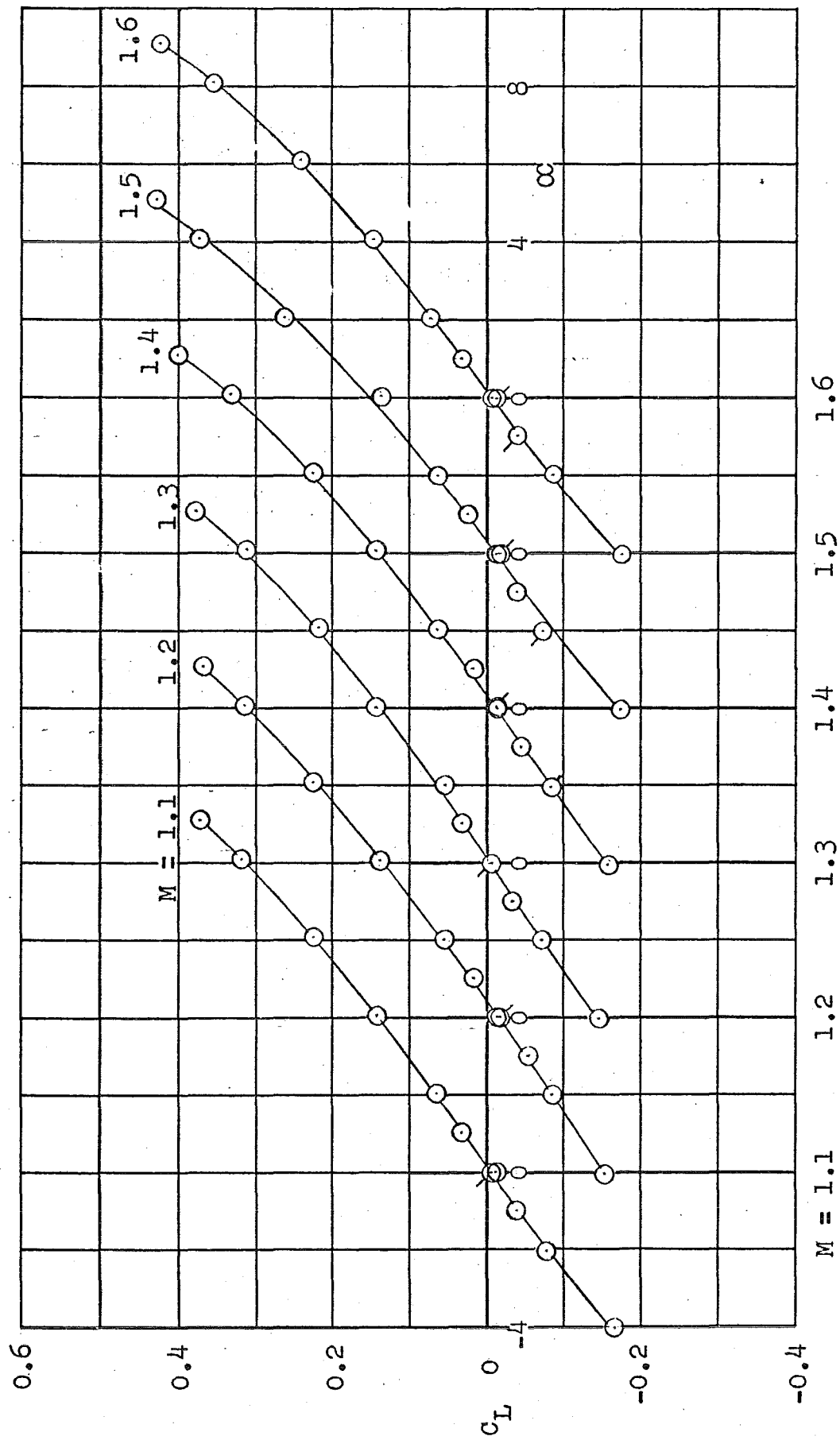
Fig. 22 Concluded
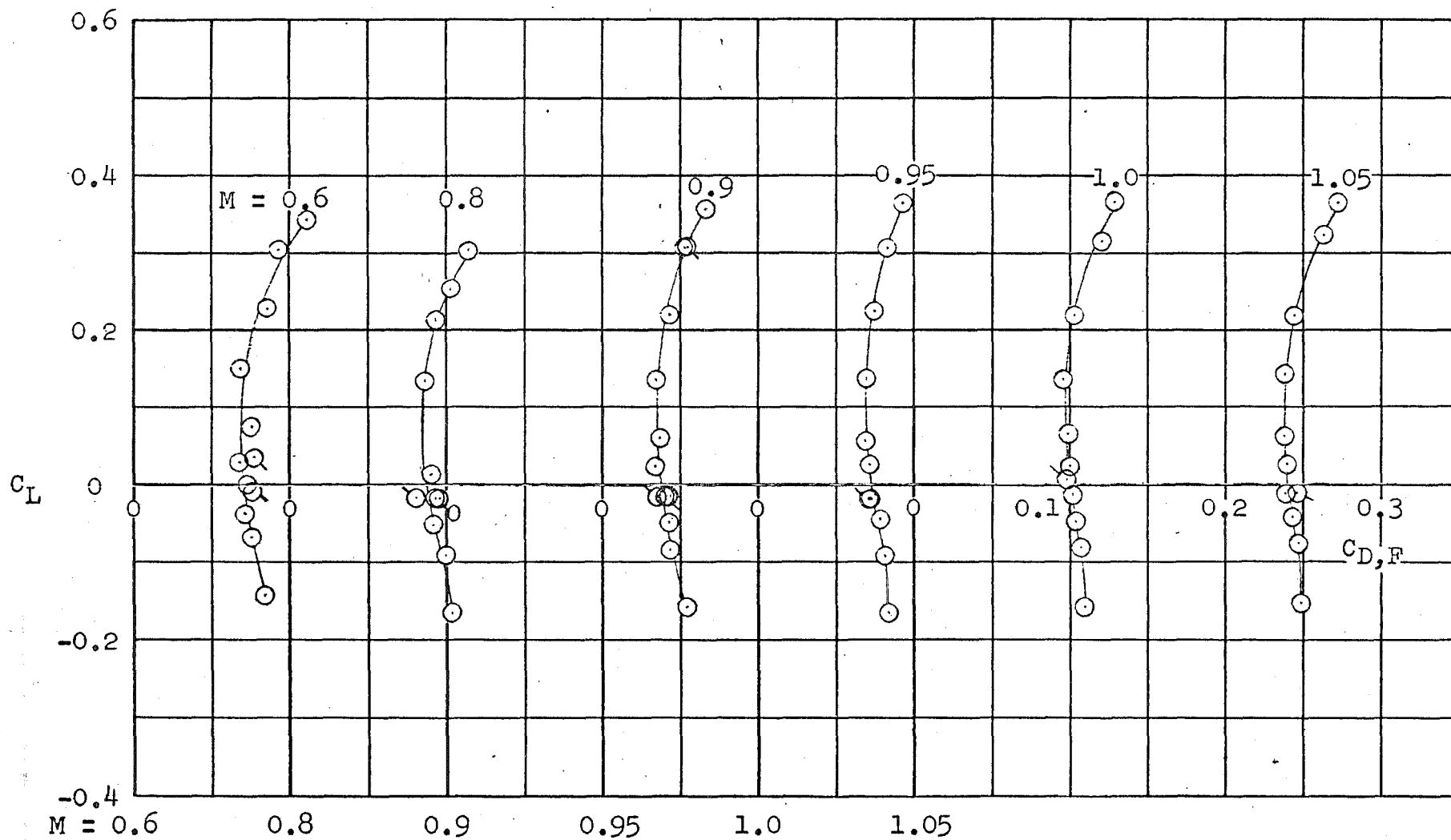
Fig. 23   Variation of Forebody-Drag Coefficient with Lift Coefficient
for 8.5-diam Cone-Cylinder Model for a Series of Mach Numbers
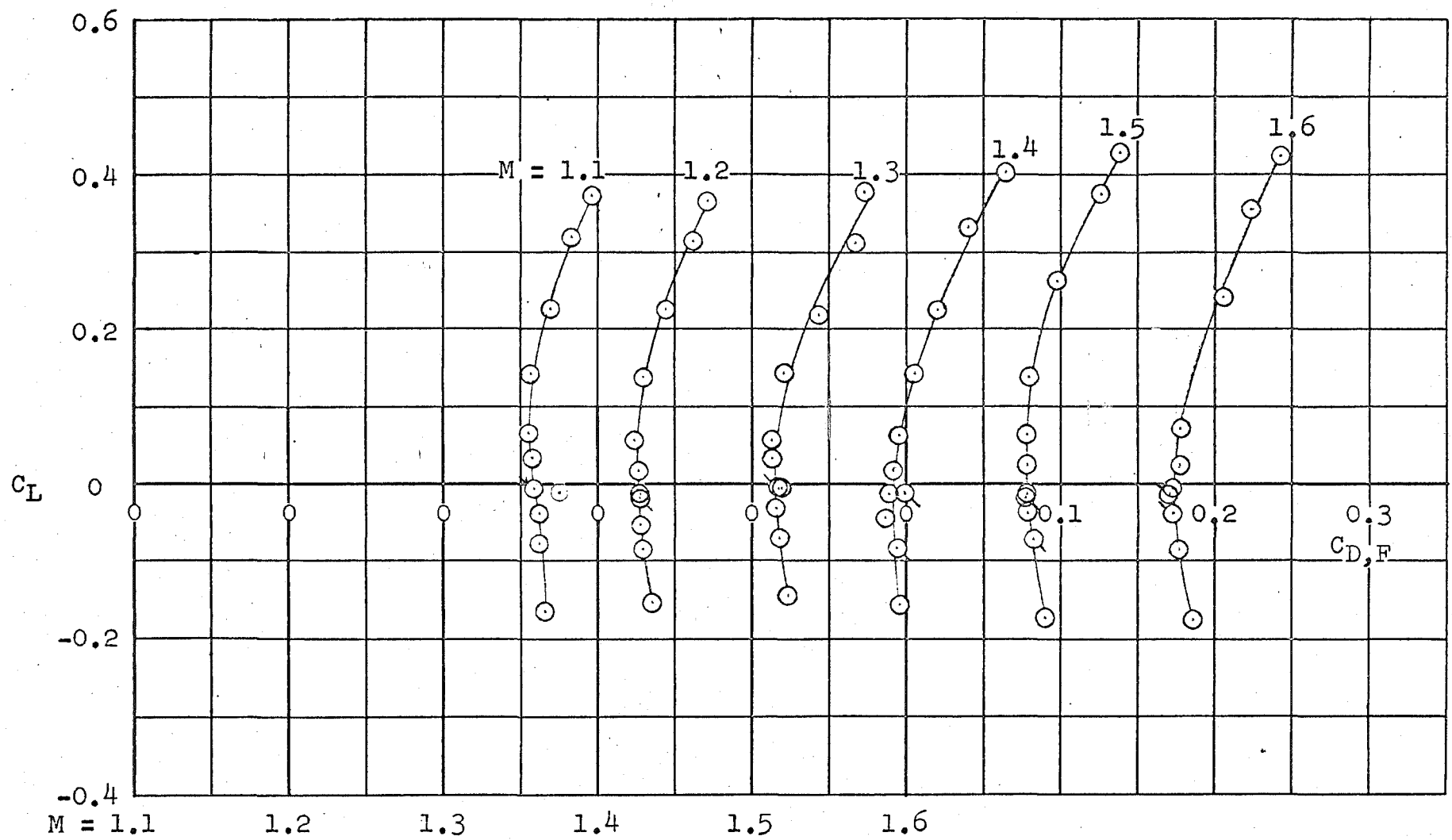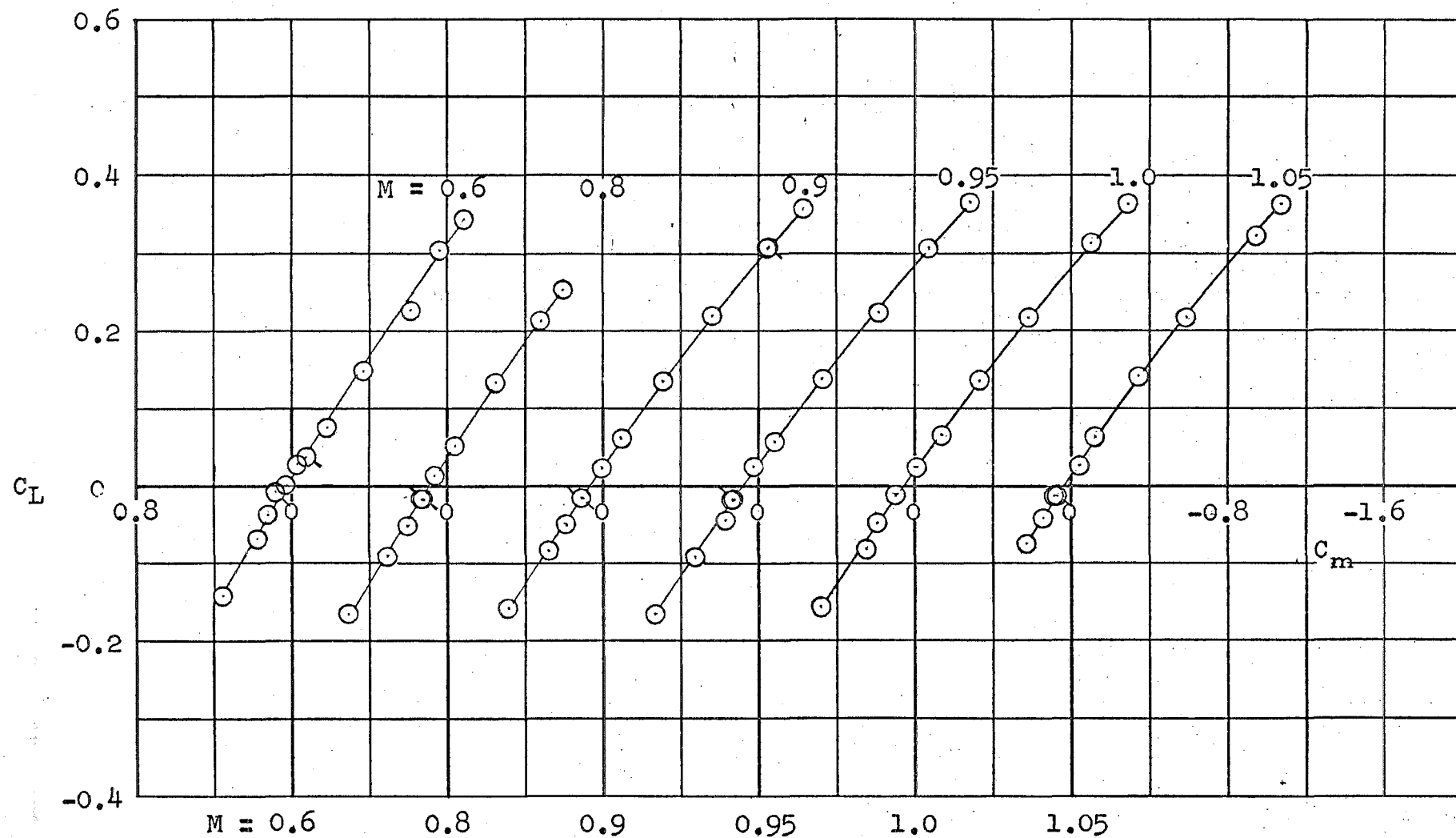
Fig. 23 Concluded

Fig. 24 Variation of Pitching-Moment Coefficient with Lift Coefficient for 8.5-diam Cone-Cylinder Model for a Series of Mach Numbers

Fig. 24 Concluded

Fig. 25 Variation of Lift Coefficient with Angle of Attack for 8.5-diam
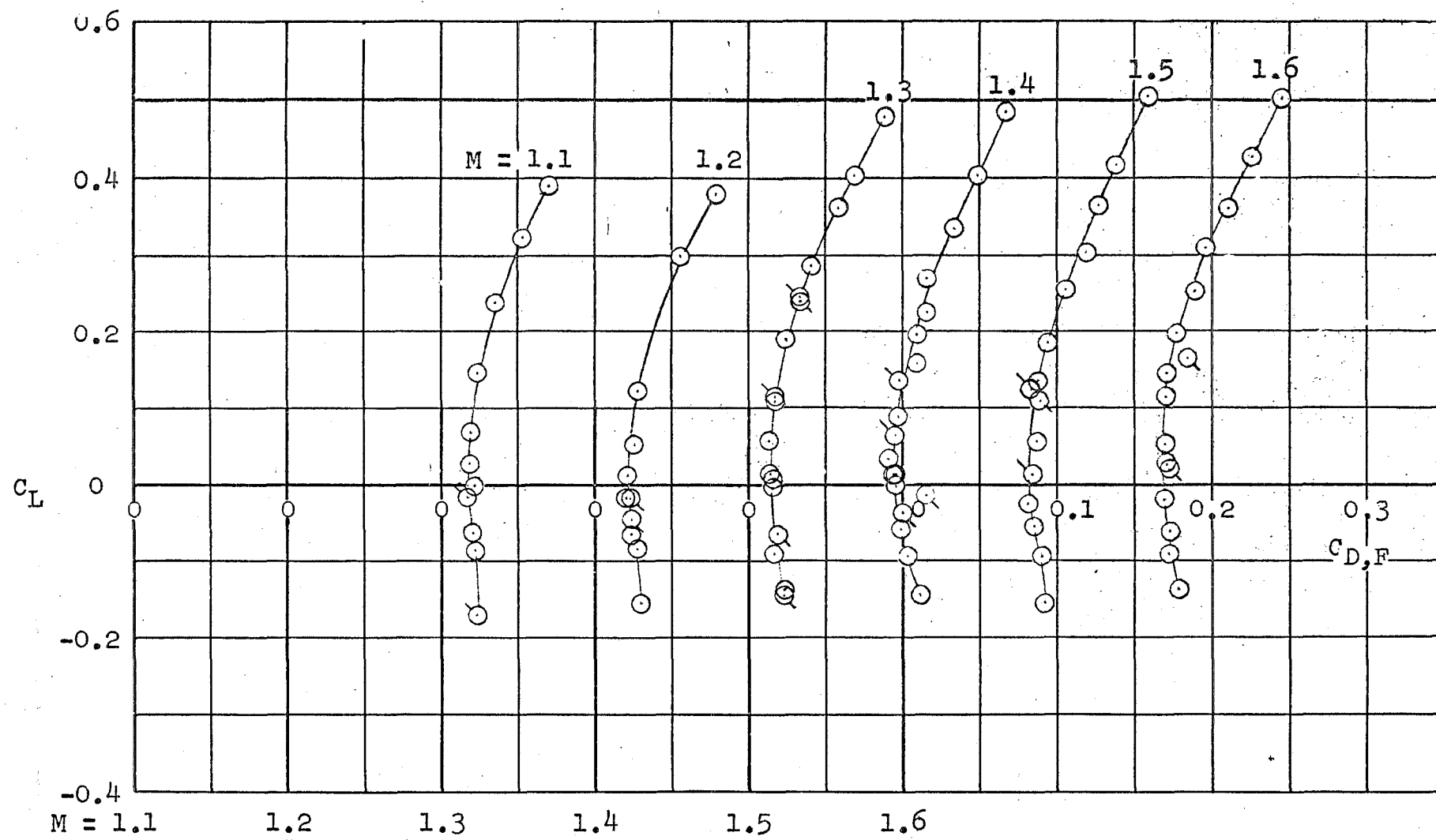Ogive-Cylinder Model for a Series of Mach Numbers

Fig. 25 Concluded

Fig. 26 Variation of Forebody-Drag Coefficient with Lift Coefficient
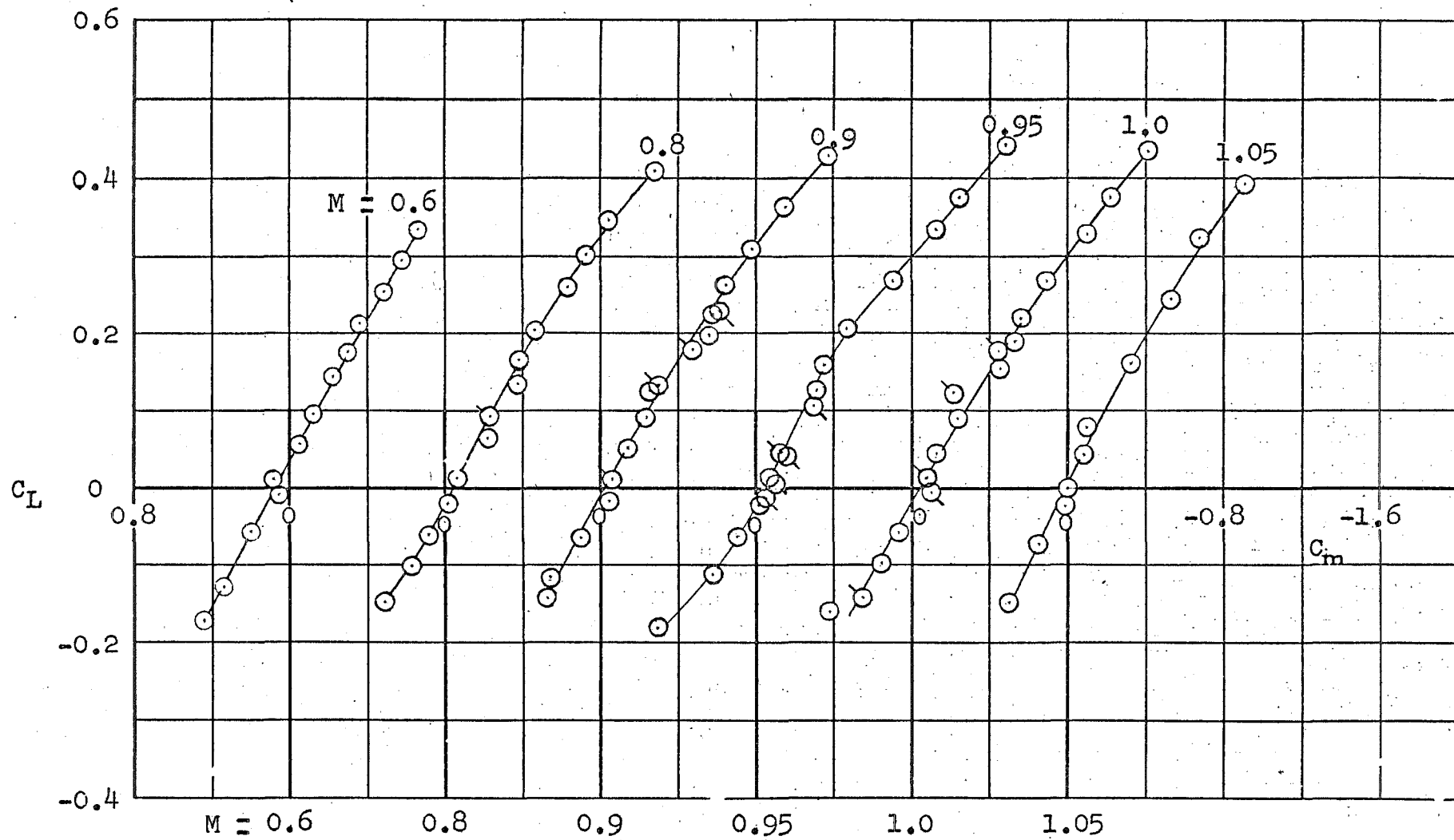for 8.5-diam Ogive-Cylinder Model for a Series of Mach Numbers

Fig. 26 Concluded

Fig. 27 Variation of Pitching-Moment Coefficient with Lift Coefficient
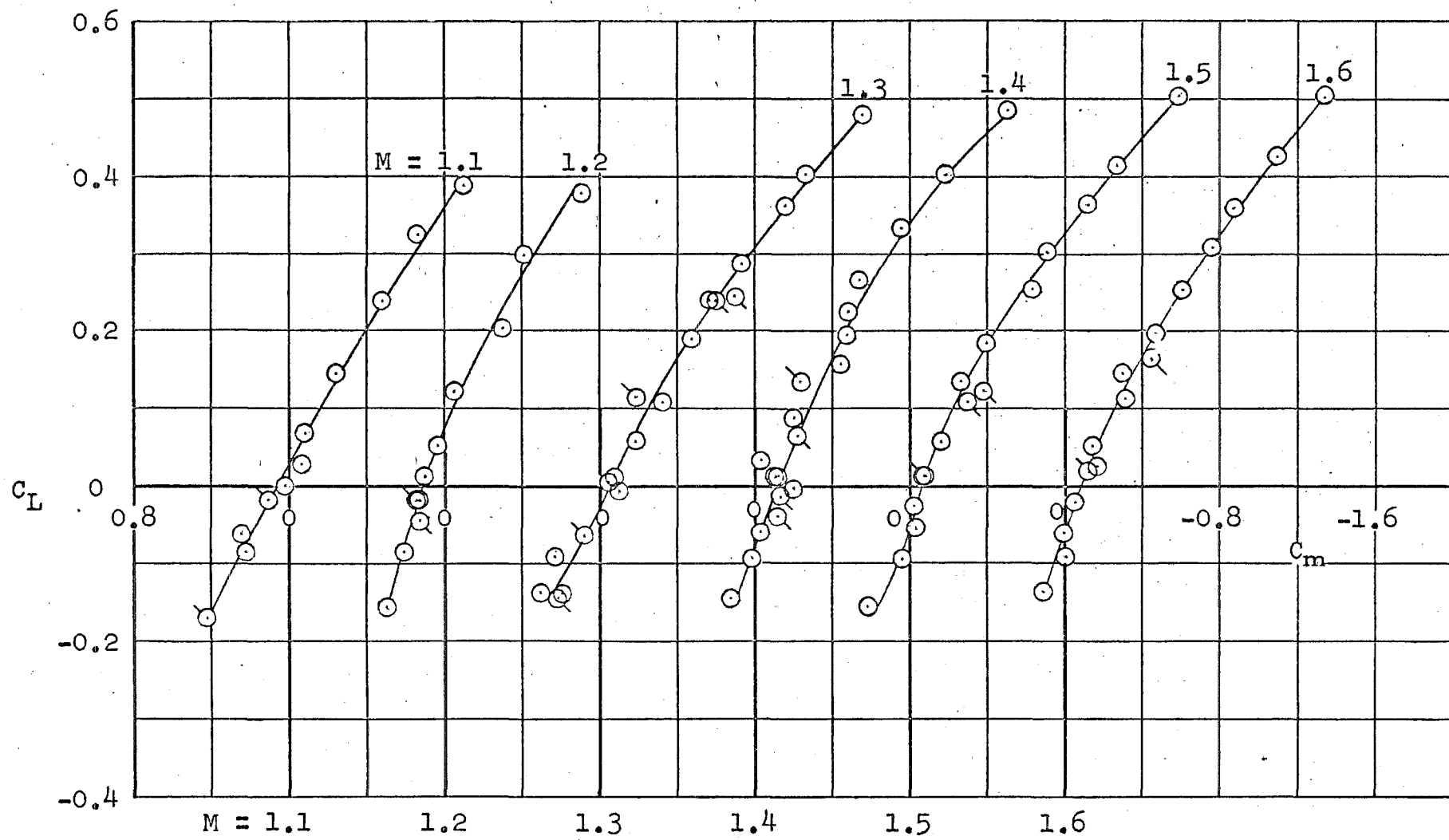for 8.5-diam Ogive-Cylinder Model for a Series of Mach Numbers
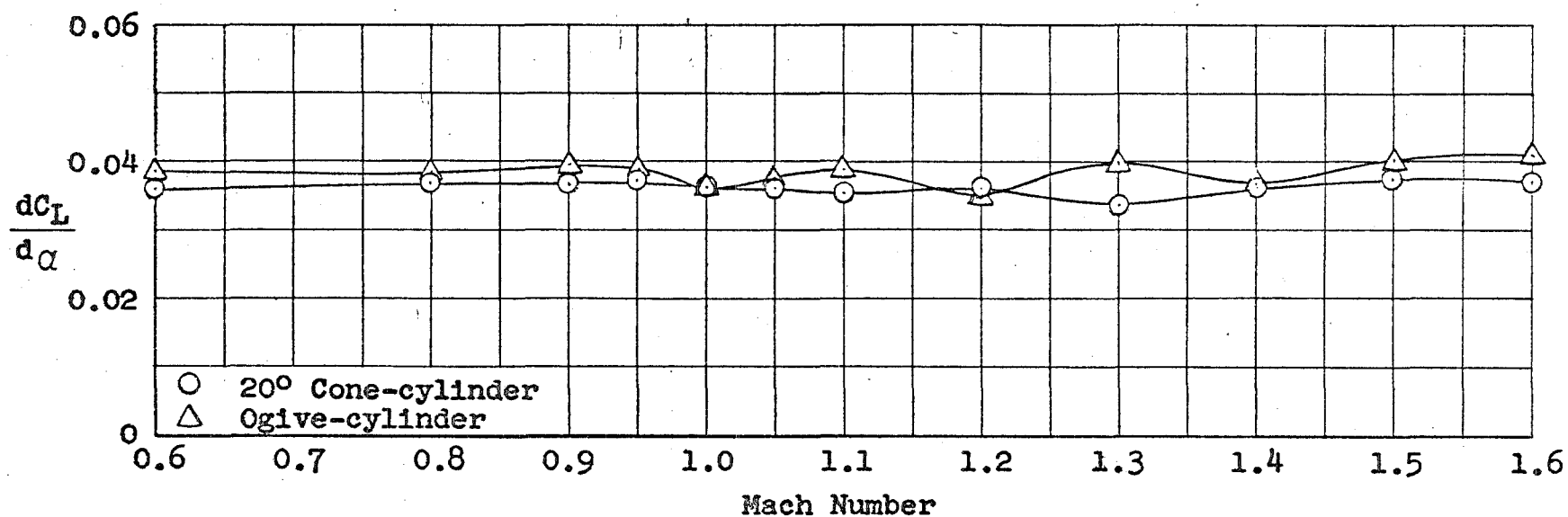
Fig. 27 Concluded

Fig. 28 Variation of Lift Curve Slope at Zero Angle of Attack with
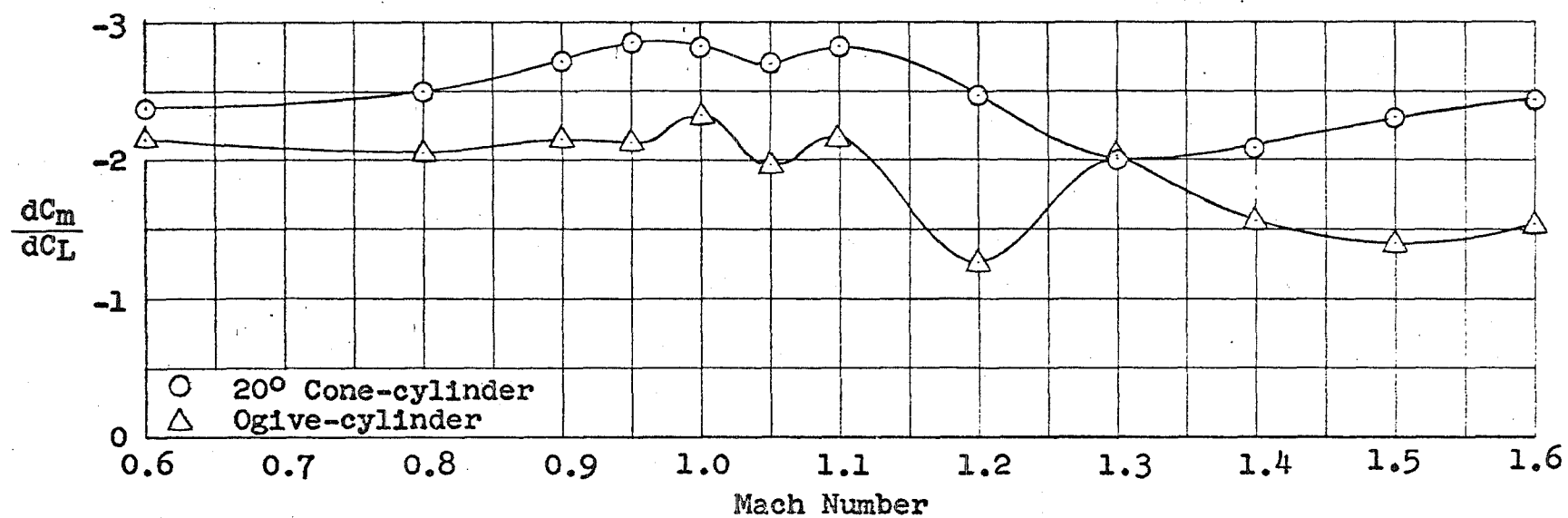Mach Number for 1-Percent Cone-Cylinder and Ogive-Cylinder
Models

Fig. 29 Variation of Pitching-Moment Curve Slope at Zero Angle of Attack
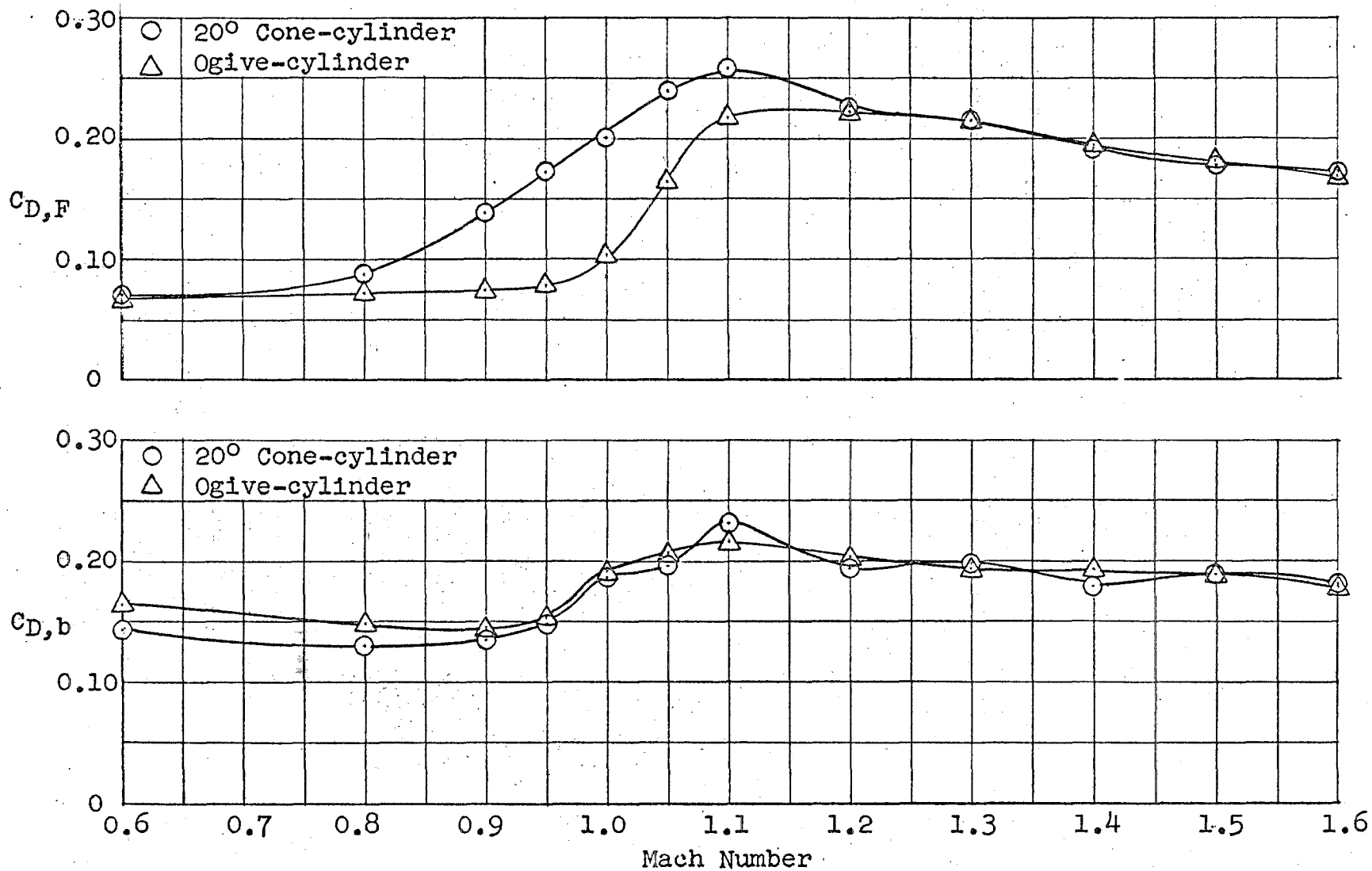with Mach Numbers for 1-Percent Cone-Cylinder and Ogive-
Cylinder Models

Fig. 30 Variation of Forebody- and Base-Drag Coefficients at Zerɔ
Angle of Attack with Mach Number for 1-Percent Cone-
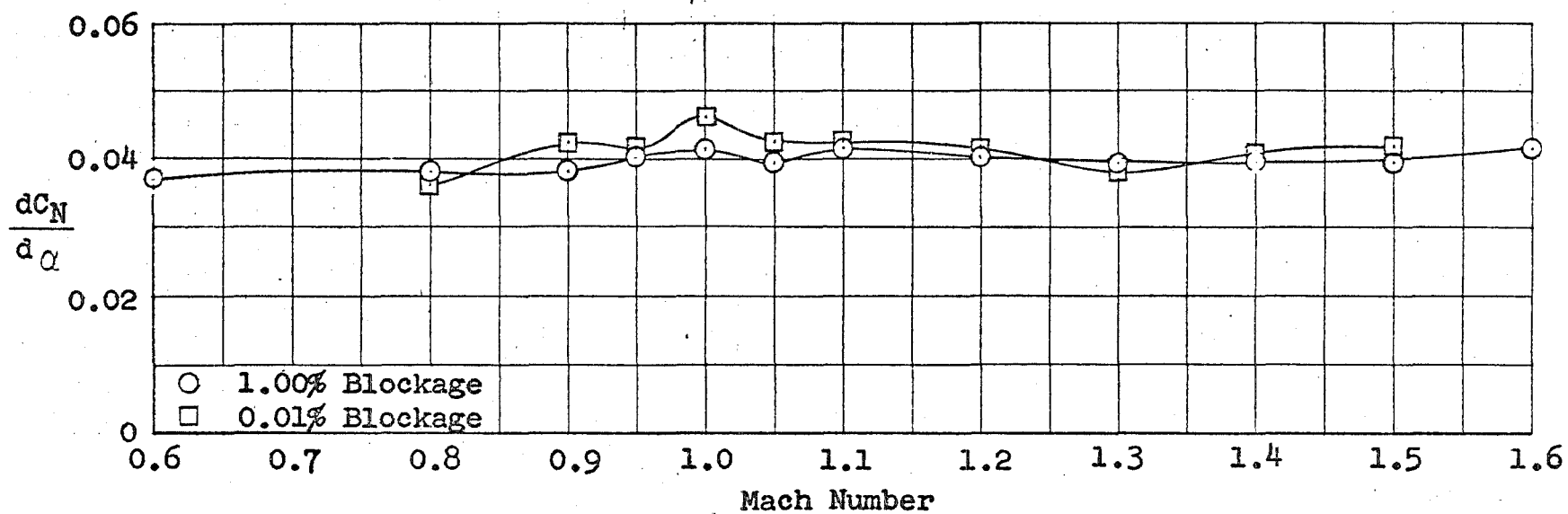Cylinder and Ogive-Cylinder Models

Fig. 31 A Comparison of Normal-Force Curve Slopes at Zero Angle of
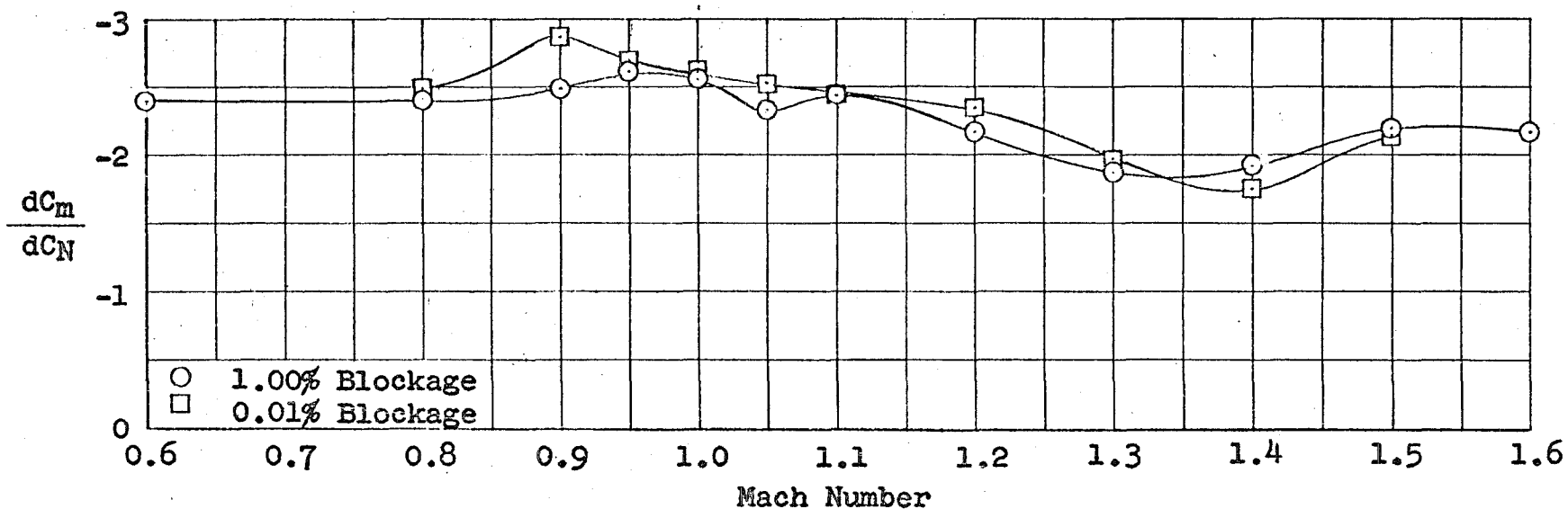Attack for 1-Percent and 0.01-Percent Cone-Cylinder Models

Fig. 32 A Comparison of Pitching-Moment Curve Slopes at Zero
Angle of Attack for 1-Percent and 0.01-Percent Cone-
Cylinder Models